Ancient TL

www.ancienttl.org · ISSN: 2693-0935

Issue 38(1) - June 2020
https://doi.org/10.26034/la.atl.v38.i1

This issue is published under a Creative Commons Attribution 4.0 International (CC BY):
https://creativecommons.org/licenses/by/4.0

© Ancient TL, 2020

ISSN 0735-1348

Ancient TL

A periodical devoted to Luminescence and ESR dating

Department of Physics, East Carolina University, 1000 East 5th Street, Greenville, NC 27858, USA
http://ancienttl.org

June 2020, Volume 38 No.1

Dose-Rate Estimation using α-Al_2O_3:C Chips: Aftermath 1
Sebastian Kreutzer, Chantal Tribolo, Loïc Martin and Norbert Mercier

Radiofluorescence of quartz from rocks and sediments and its correlation with thermoluminescence and optically stimulated luminescence sensitivities 11
Pontien Niyonzima, André O.Sawakuchi, Mayank Jain, Raju Kumar, Thays D. Mineli, Ian del Río and Fabiano Pupim

***eM-Age* (excel Macro for Age calculation), a new application for luminescence age calculation based on Dose Rate and Age Calculator (*DRAC*) and Analyst** 21
Carlos Pérez-Garrido

Thesis abstracts 25

Bibliography 31

Announcements 44

Ancient TL

Started by the late David Zimmerman in 1977

EDITOR

Regina DeWitt, Department of Physics, East Carolina University, Howell Science Complex, 1000 E. 5th Street Greenville, NC 27858, USA; Tel: +252-328-4980; Fax: +252-328-0753 (dewittr@ecu.edu)

EDITORIAL BOARD

Ian K. Bailiff, Luminescence Dating Laboratory, Univ. of Durham, Durham, UK (ian.bailiff@durham.ac.uk)
Geoff A.T. Duller, Institute of Geography and Earth Sciences, Aberystwyth University, Ceredigion, Wales, UK (ggd@aber.ac.uk)
Sheng-Hua Li, Department of Earth Sciences, The University of Hong Kong, Hong Kong, China (shli@hku.hk)
Shannon Mahan, U.S. Geological Survey, Denver Federal Center, Denver, CO, USA (smahan@usgs.gov)
Richard G. Roberts, School of Earth and Environmental Sciences, University of Wollongong, Australia (rgrob@uow.edu.au)

REVIEWERS PANEL

Richard M. Bailey
Oxford, UK
richard.bailey@ouce.ox.ac.uk

James Feathers
Seattle, WA, USA
jimf@uw.edu

Rainer Grün
Canberra, Australia
rainer.grun@anu.edu.au

David J. Huntley
Burnaby B.C., Canada
huntley@sfu.ca

Sebastian Kreutzer
Bordeaux, France
sebastian.kreutzer@u-bordeaux-montaigne.fr

Michel Lamothe
Montréal, Québec, Canada
lamothe.michel@uqam.ca

Norbert Mercier
Bordeaux, France
norbert.mercier@u-bordeaux-montaigne.fr

Didier Miallier
Aubière, France
miallier@clermont.in2p3.fr

Andrew S. Murray
Roskilde, Denmark
anmu@dtu.dk

Vasilis Pagonis
Westminster, MD, USA
vpagonis@mcdaniel.edu

Naomi Porat
Jerusalem, Israel
naomi.porat@gsi.gov.il

Daniel Richter
Leipzig, Germany
drichter@eva.mpg.de

David C.W. Sanderson
East Kilbride, UK
David.Sanderson@glasgow.ac.uk

Andre Sawakuchi
São Paulo, SP, Brazil
andreos@usp.br

Ashok K. Singhvi
Ahmedabad, India
singhvi@prl.res.in

Kristina J. Thomsen
Roskilde, Denmark
krth@dtu.dk

Web coordinators: Joel DeWitt, Regina DeWitt
Article layout and typesetting: Regina DeWitt, Sebastian Kreutzer
Bibliography: Sebastien Huot

licensed under CC BY 4.0

Ancient TL

Dose-Rate Estimation using α-Al_2O_3:C Chips: Aftermath

Sebastian Kreutzer[1,2], Chantal Tribolo[1], Loïc Martin[3,1], Norbert Mercier[1]

[1]Geography & Earth Sciences, Aberystwyth University, Aberystwyth, Wales, United Kingdom
[2]IRAMAT-CRP2A, UMR 5060, CNRS-Université Bordeaux Montaigne, Pessac, France
[3]Scottish Universities Environmental Research Centre, East Kilbride, United Kingdom

Corresponding Author:sebastian.kreutzer@aber.ac.uk

Received: April 23, 2020; in final form: May 25, 2020

Abstract

We present additional experiments for α-Al_2O_3:C chips used to estimate *in situ* γ-dose rates. Our contribution supplements the article by Kreutzer et al. (2018) and presents results from previously announced follow-up experiments. (1) We investigate the divergent γ-dose rate results we obtained from cross-check experiments for one reference site. (2) We discuss the origin of encountered large inter-aliquot scatter using results from low-level background and calibration measurements. (3) We show that the chip geometries vary considerably, which may partly contribute to additional inter-aliquot scatter, regardless of an overall good reproducibility of results. (4) We report new source-calibration results after replacing the β-source housing of our measurement system, which resulted in an increase of the source dose rate at the sample position by ca 37 %. *GEANT4* simulations show that the increased dose rate is likely caused by an unfortunate fabrication tolerance of the shutter in front of the β-source, which, in combination with the chip geometry, significantly contributes to the observed inter-aliquot scatter. (5) Finally, we introduce a newly developed shiny application we use at the IRAMAT-CRP2A to analyse α-Al_2O_3:C measurements. The application is open-source and freely available.

Keywords: Dosimetry, Al_2O_3:C, Luminescence

1. Introduction

Two years ago, Kreutzer et al. (2018) published an article outlining techniques and workflow to determine the environmental γ-dose rate with passive α-Al_2O_3:C chips (Akselrod et al., 1990a,b, 1993). The contribution included performance tests of the used *lexsyg SMART* (Richter et al., 2015) reader, newly developed software functions for the **R** (R Core Team, 2019) package 'Luminescence' (Kreutzer et al., 2012), an application example at the archaeological site Sierra de Atapuerca (e.g., Aguirre & Carbonell, 2001), and a cross-check of the so estimated γ-dose rates against four different references sites around Clermont-Ferrand (France) (Miallier et al., 2009). While the performance of the presented system proved satisfactory, we identified two issues as potential subjects to further tests:

1. The cross-check against the reference site 'PEP' (a granite block, cf. Miallier et al., 2009) yielded a γ-dose rate ca 13 % lower than expected. Kreutzer et al. (2018) argued that field evidence revealed a tube movement partly out of the granite block after storage, which may have caused the recorded lower γ-dose rate ($\dot{D}_\gamma$).

2. The observed relative standard deviation (three chips in each of the 21 dosimeter tubes) ranged from 1.1 % to 15.1 % for the application site Sierra de Atapuerca. The resulting average value of 5.1 % was much higher than the 0.2 % scatter observed in reproducibility tests in the laboratory.

In the best tradition of Ancient TL, our contribution compiles a lab report with results addressing these two previously encountered issues. Additionally, we present observations made in the course of our β-source calibrations after exchanging the source-module housing. The remainder briefly

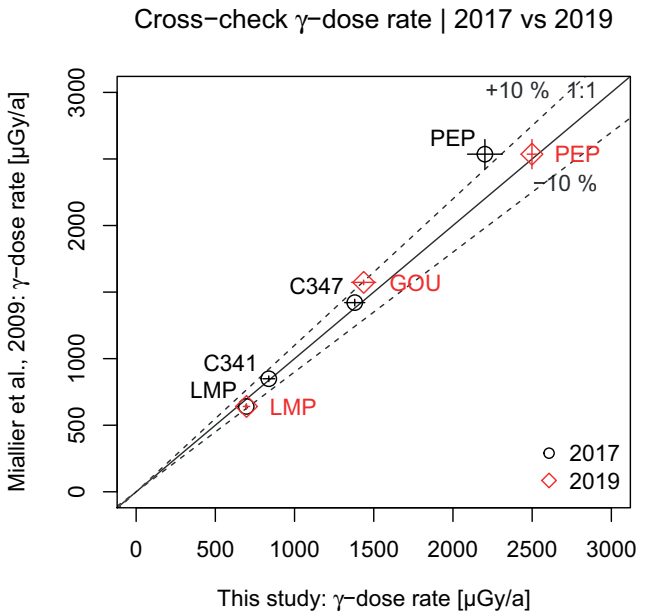

Figure 1. Natural γ-dose rates measured according to Kreutzer et al. (2018) against values tabulated in Miallier et al. (2009) in 2017 (black circles) (Kreutzer et al., 2018, their Fig. 8) and newly measured in 2019 (red diamonds). The solid black line indicates the 1:1 line, dashed lines the 10 % divergence from unity. For the measured chips we quoted the mean ± standard deviation of the mean. For the reference site values, uncertainties were taken from Miallier et al. (2009). Please note that in Kreutzer et al. (2018) we mixed up the labels for the sites LMP and C341. Here the labels are plotted correctly.

introduces an open-source shiny (Chang et al., 2019) application developed to analyse α-Al_2O_3:C measurements at the IRAMAT-CRP2A.

We will keep details on instrumentation, measurement protocol and analysis procedure to a minimum. For full details, we refer to Kreutzer et al. (2018), which is available as an open-access article. For all presented measurements, we employed the same *lexsyg SMART* (Richter et al., 2015) luminescence reader we already used for the article by Kreutzer et al. (2018). For the data analysis we employed the **R** scripts from Kreutzer et al. (2018) in conjunction with the most recent version of the **R** package 'Luminescence' (Kreutzer et al., 2019). Data analysis and visualisation benefited from the **R** packages 'ggplot' (Wickham, 2009), 'gridExtra' (Auguie, 2017), 'readxl' (Wickham & Bryan, 2019), and 'khroma' (Frerebeau, 2019).

2. $\dot{D}_\gamma$ cross-check

Our first experiment concerned the divergent γ-dose rate ($\dot{D}_\gamma$) results we obtained from our cross-check experiments for the granite block 'PEP'. The $\dot{D}_\gamma$ measured with the α-Al_2O_3:C chips was ca 13 % lower than expected in comparison to the values quoted in Miallier et al. (2009). In summer 2018, new tubes with three chips each were stored at three reference sites: (1) 'PEP' (granite), (2) 'LMP' (basalt), and (3) the before not considered site 'GOU' (trachyandesite). The three sites cover a wide range of annual $\dot{D}_\gamma$ values allowing to re-evaluate the performance of the procedure by Kreutzer et al. (2018) from, LMP: (641 ± 18) μGy a^{-1}, over GOU: (1573 ± 17) μGy a^{-1}, up to PEP: (2536 ± 110) μGy a^{-1} (Miallier et al., 2009). The dosimeters were measured in February 2019, five days after their retrieval from the sites. In total, the environmental $\dot{D}_\gamma$s were recorded over 313 days (LMP, GOU), and 315 days (PEP).

The combined results of our measurements from 2017 and 2019 are displayed in Fig. 1. Our measurements from 2019 (red diamonds) exhibit $\dot{D}_\gamma$-values within 10 % of the expected $\dot{D}_\gamma$. These findings seem to confirm the hypothesis that the unexpected dose-rate offset measured for PEP was not random but likely related to a displacement of the sample tube after initial storage in the rock. However, below, we will discuss another possibility that will let appear this result coincidentally. We will show that the geometry of the chips in combination with the irradiation geometry, may have led to the discrepancy observed in 2017.

Besides, the data exhibit that the expected natural $\dot{D}_\gamma$-values can be sufficiently recovered. Sample LMP gave nearly identical results, with an overall recovery of 0.98 ± 0.09 (2017) vs. 1.00 ± 0.09 (2019) (quoted are arithmetic mean ± standard deviation). In summary (data 2017 and 2019, excluding the outlier for PEP from 2017), a natural $\dot{D}_\gamma$ can be recovered within ca 7 % from unity.

3. Cosmic-dose rate impact?

The second experiment targeted the inter-aliquot dispersion when chips are stored in a natural environment over a long period (> 1 day). Kreutzer et al. (2018) speculated that cosmic-rays might explain the dispersion of the dose values due to the storage orientation of the chips in the site. Horizontal stacking of the chips in the tube usually exposes a smaller surface towards the cardinal point than vertically stacked chips. Although cosmic-rays do not hit targets on the ground only in a 90° angle, the chip orientation may indeed play a role in the observed scatter. To test whether the chip orientation has a measurable impact on the $\dot{D}_\gamma$ scatter, we designed the following experiment.

Twenty-six chips, reset at 910 °C for 10 min in an external furnace, were placed in a home-made cuboid made out of radio-nuclide free polymethyl methacrylate (PMMA, acrylic glass) (Fig. 2). The cuboid has a footage of 100 × 80 mm and a total height of 60 mm and consists of two parts, a cover and a body. The cover is detachable, either to stack chips in a vertical or horizontal orientation in slots in the cuboid body. The slots size facilitate chips with a diameter up to 5.2 mm. The box design and the location of the slots within the cuboid ensured that the chips were not affected by external α and β-particles. Their contribution to the dose accumulated by the chips is negligible. All slots used were filled up to their maximum capacity with chips. The number of chips per slot varied due to different chip thickness (see Sec. 4). Scotch tape ensured that the chips did not move. The box cover and box body were glued and sealed with Scotch tape

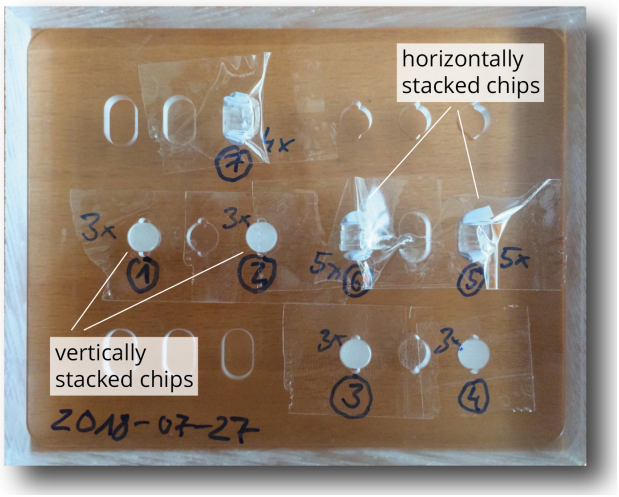

Figure 2. Top view photo of the bottom of the dosimeter storage cuboid made of radionuclide free acrylic glass. The cuboid has 18 positions, nine for horizontally and nine for vertically chip stacking. For our experiments, we used only seven positions (26 chips in total). The number of chips per position varied with chip thickness (four chips in position 7 vs five chips each in positions 5 and 6). Scotch tape on the top prevented the chips from moving. During the experiment, bottom and cover of the cuboid were glued together. The brownish background in the photo reflects the office table where the cuboid was placed on for the photo.

and enveloped in opaque bags to prevent light exposure. The cuboid was then placed in the low-background radiation lead castle in the cellar of the IRAMAT-CRP2A. This lead castle is the same that we use to store, temporarily, dosimeter tubes from the field, if they cannot be measured upon arrival.

The chips were stored for 361 days and then measured and analysed following the procedure outlined in Kreutzer et al. (2018). Figure 3 shows the results of this experiment for dose values derived from the green stimulated luminescence (GSL) signal and the subsequent thermal luminescence (TL) signal used to deplete the remaining luminescence. Black circles display results of the accumulated dose for chips orientated vertically, and red triangles illustrate horizontally stacked chips. It appears that the individual standard error[1] for vertically stacked chips are slightly higher than for chips stored horizontally. However, the main question is: *Does the distribution indicate two distinct dose groups correlated with the orientation of the chips in the cuboid?*

A two-sided Welch t-test returned a p-value of 0.04 (t = 2.17, df = 24). This result suggests a random difference between the two groups for a significance level of 1 %. However, a Q-Q plot (not shown) revealed that the distributions followed only vaguely normal distributions, which makes the application of a t-test debatable. An additionally performed two-sided Kolmogorov-Smirnov test returned a p-value of 0.14 (D = 0.43), also implying that the observed difference between the two orientation groups is random.

[1]The term "standard error" was used following the nomenclature used by Galbraith (1990).

As a side effect, with the described experiment, we were able to estimate the background-dose rate in our lead castle. The average accumulated dose over 26 chips amounted to $(155 \pm 23)\,\mu$Gy, which corresponds to an annual background-dose rate ($\dot{D}_\gamma + \dot{D}_{cosmic}$) of ca 157 μGy a^{-1}. In light of the minimum determination limit of ca 10 μGy estimated by Kreutzer et al. (2018) for the dosimetry system (OSL/TL reader and measurement protocol) used at the IRAMAT-CRP2A, it implies that dosimeter tube storage times of less than one month will not add a dose distinguishable from background noise.

Nevertheless, Fig. 3 indicates an additional grouping of aliquots, which does not appear to be related to the slot group positioning and the orientation of the chips in the cuboid. Moreover, the plot reveals a large scatter between chips in general (c_v of the full dataset: 14.5 %).

Over the years, we purchased batches of α-Al_2O_3:C chips from the same manufacturer varying slightly in diameter, thickness and colour (transparent, milky). For all measurements shown here and by Kreutzer et al. (2018), chips were not preselected but picked-up randomly from a box containing hundreds of chips of mixed batches. The reproducibility experiments by Kreutzer et al. (2018) did not reveal any particular problem with the chips or showed a particular correlation with an unknown variable.

While we cannot exclude that different batches have slightly different dose-response characteristics, additional measurements were made in order to double check the effect of varying chip geometry on the measured dose.

4. Chip geometry impact

We analysed 33 Al_2O_3:C chips placed in 11 tubes such as those described by Kreutzer et al. (2018) and inserted them for one year in the stratigraphic section of Border Cave, a Palaeolithic site in South Africa (e.g., Grün & Beaumont, 2001; Backwell et al., 2018). Each tube contained three chips; one additional tube was used as travel dosimeter. After the measurements, the thickness and diameter of each chip were measured (accuracy $\pm$ 0.01 mm). Figure 4 displays the variability of the chip geometry. We identified two major groups: (1) chips displaying thickness values between 0.78 mm and 0.80 mm and diameters between 5.01 mm and 5.16 mm, and (2) chips with higher thickness between 0.87 mm to 1.02 mm but narrower diameter (4.61 mm to 4.99 mm). A third group with a thickness similar to group (1) but with diameters in the same range as group (2) might be identifiable. Overall, diameter and thickness can vary from chip-to-chip by up to 12 % and 20 %, respectively.

The tubes were located in different places at Border Cave, and we did not expect similar D_γ-values for different tubes. However, the three chips within each tube should display statistically undistinguishable doses. In Fig. 5 we show the measured standardised dose as dependent variable of the chip volume (as aggregated variable of thickness and diameter); colours code different tubes. Figure 5A renders a picture similar to Fig. 4, the chips show two separate groups.

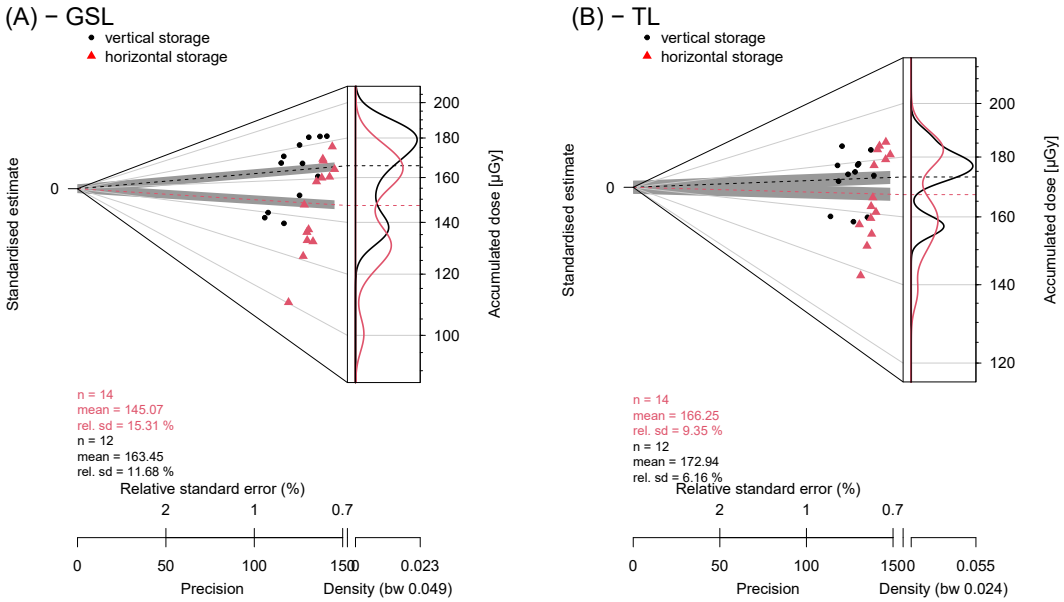

Figure 3. Abanico plots (Dietze et al., 2016) showing accumulated background doses after 361 days. Black circles indicate vertically, red triangles horizontally stacked chips. (A) D_e derived using the GSL signal, (B) D_e determined from the subsequent TL curve. In the latter case the obtained dose is not overall correct, but the scatter between the two groups can still be compared. For the interpretation of the term "relative standard error" as used in the plot we refer to Galbraith (1990).

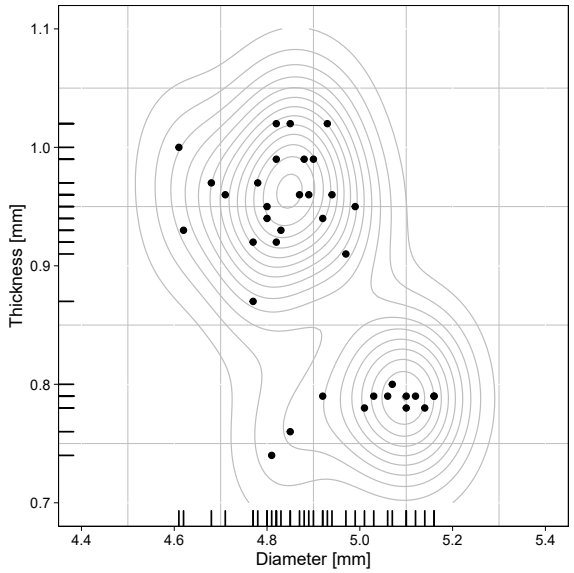

Figure 4. Diameter and thickness variation of the chips (n=33). Measurement uncertainties are too small to be displayed.

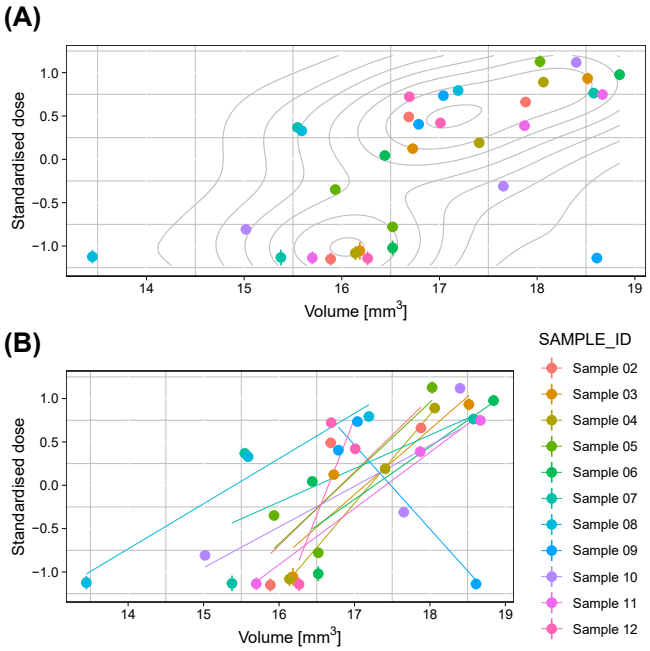

Figure 5. Standardised dose vs chip volume. (A) and (B) show the same values, with a different graphical representation. The solid lines in (B) are linear regression lines for each tube. Standardised dose values were calculated as follows: $d_{std} = (d_i - \bar{d})/\sigma$, with $\bar{d}$ being the average dose rate and σ the standard deviation.

Whether this difference in volume relates to real differences in doses can be seen in Fig. 5B. Here we have drawn regression lines separately for each tube. We observed, (1) a significant variability for the measured dose in each tube (10 % to 20 %), and (2) that this variation appears to correlate positively with the chip volume. Higher volumes seem to lead to higher doses. One tube (Sample 09, Fig. 5B), shows a negative correlation of volume with dose, which might be, however, related to the luminescence characteristics of this particular chip.

We checked similar plots for the diameter and the thickness instead of the aggregated variable volume (not shown). Using a regression analysis to understand the impact of thickness and diameter on the standardised dose, we found that, combined, both parameters explain 59.5 % (adjusted R^2) of the variance in the dataset. However, only the thickness has a significant impact on the explained variance. In other

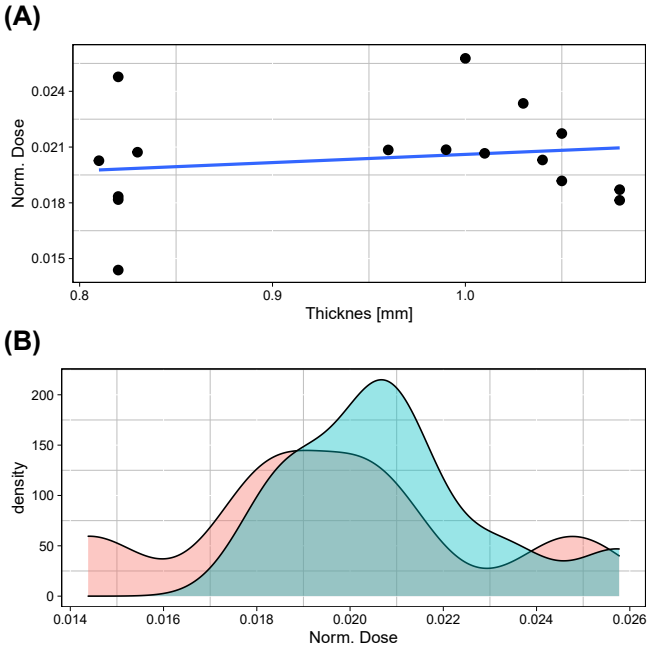

Figure 6. Apparent dose normalised to the storage duration vs chip thickness. (A) Displays a weak positive correlation between thickness and normalised dose. (B) shows the normalised dose groups (threshold: chip thickness 0.9 mm) as kernel density plots, both distributions overlap and are statistically indistinguishable (see *t*-test results).

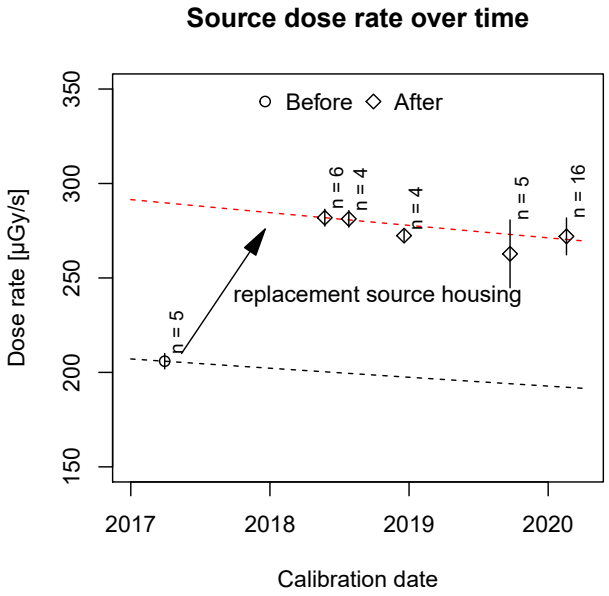

Figure 7. Source-calibration results over time. The dashed lines indicate the predicted dose-rate evolution of the ^{90}Sr/^{90}Y-source based in the first calibration point. The circle indicates the dose rate before, the diamonds the dose rates after the source housing was replaced. Dose-rate values refer to calibration measurements under the source with its shutter closed. Shown are mean ± standard deviation of the mean.

words, while differences in diameter may still have a small impact on the dose variance, the major driver appears to be the chip thickness. Hence, 40.5 % of the variance remain unexplained. The true dose (D_γ + D_{cosmic}) recorded in each tube should be independent of the chip thickness, given the travel range of natural γ-photons and cosmic-rays. The variability observed in the apparent dose for each set of the three chips may thus be linked to the irradiation in the luminescence reader. This consists of bremsstrahlung and high-energy electrons (Kreutzer et al., 2018), which are attenuated at the scale of a few millimetres (see Sec. 5). If this is the case, the source dose rate obtained through calibration measurements should be a function of the chip thickness.

Hence, we set up a new calibration experiment taking into account the chip thickness. The experimental design was similar to what was done by Kreutzer et al. (2018). We stored six tubes (three chips each), in the middle of a brick block with a well known γ-dose rate (Richter et al., 2010) available in the basement of the IRAMAT-CRP2A for periods of 140 days to 634 days.

Figure 6 displays the results of this experiment as thickness vs dose normalised to the storage duration. We removed two (out of 18 values) from the plot. One chip exhibited a dose ca two times higher than the highest dose value from the distribution and one chip could not be retrieved from the tube.

The chip thicknesses range similar to those values observed previously, i.e. between 0.81 mm and 0.83 mm for one group and between 0.96 mm and 1.08 mm for the second one.

While Fig. 6A indicates a weak positive correlation between chip thickness and normalised dose (r = 0.17), the two dose distributions (Fig. 6B) are statistically indistinguishable for a significance level of 5 % (two-sided Welch *t*-test, *p*-value: 0.367, *t* = -0.96, df = 7.7).

It must be noted here that, contrary to what was recommended in Kreutzer et al. (2018), the cups used for the measurements were not heated to 450 °C before the measurements. This may have induced some additional scatter. However, the mean dose rate is consistent with dose rates expected from previous experiments, where heating of the discs before the measurement was performed (see below).

5. Source-calibration and an unexpected dose-rate evolution

In summer 2018, a shutter failure of the β-source module in the *lexsyg SMART* required a source-housing exchange service. This requires that the ^{90}Sr/^{90}Y source (cf. Fig. 2 in Richter et al., 2012) is detached from the housing module (enveloped in a lead shield), which facilitates shutter and sensor electronics, before getting re-attached to the new housing. In theory, since the modules are certified and identical in design, such intervention should not alter the source dose rate.

To our surprise, a source calibration carried out immediately after the source-housing replacement showed a remarkable leap of the source-dose rate by 36.9 % (Fig. 7). At the same time, our routine source-calibrations using optically stimulated luminescence (OSL, Huntley et al., 1985) in

conjunction with the single-aliquot regenerated (SAR) dose protocol (Murray & Wintle, 2000) on quartz separates, also carried out after the replacement of the source housing, remained unsuspicious. We, therefore, repeated the calibration shortly after and again in 2019 applying the procedure outlined in Kreutzer et al. (2018) (including the irradiation time correction and cross-talk measurements) with fresh chips stored in the cubic brick block in the cellar of our laboratory (cf. Kreutzer et al., 2018; Richter et al., 2010). The last calibration (see results Sec. 4) was run in February 2020. Figure 4 displays all five source-calibration values rendering consistent within uncertainty after the exchange of the source housing. Moreover, Fig. 1 proves that our calibrations are overall correct since the results in 2019 and 2020 are consistent with the values from 2017 (after the replacement). Finally, the last calibration, for which the chip thickness was checked, suggests that the change in the dose rate is not related to the chip thickness (Sec. 4).

5.1. Additional *GEANT4* simulations

To determine the cause of the dose-rate change and estimate how dose is deposited as a function of the chip thickness, we ran additional *GEANT4* (Agostinelli et al., 2003) simulations on a dedicated multi-core server at the IRAMAT-CRP2A. We simulated an irradiation geometry similar to the one in the *lexsyg SMART* based on technical information provided to every customer by Freiberg Instruments. According to the manufacturer, both source housings (new and replaced one) were identical. However, the stainless steel shutter, which was produced by an external manufacturer, has a fabrication tolerance of ± 0.1 mm (pers. comm. Andreas Richter, Freiberg Instruments GmbH). In other words, the shutter can have a thickness between 0.9 mm and 1.1 mm. Based on this information and combined with our observations regarding the thickness of the chips presented above, we developed six scenarios to model the dose rate for shutter geometries of 0.9 mm, 1 mm, and 1.1 mm repeated for chips with a thickness of 0.8 mm and 1 mm.

The simulated irradiation spectrum (Fig. 8A) show that while the X-ray spectrum is not significantly affected by the thickness of the source shutter, the amount of incident β-particles range over approximately an order of magnitude. Lowest values are observed for a shutter of 1.1 mm thickness. Please note that Fig. 8A represents the six simulation scenarios, i.e. combinations of shutter thickness and chip thickness. However, the incident spectra cannot be affected by the chip thickness, and variations in the curves are random. Figure 8B shows the local dose-rate profile for the three shutter configurations. The curve shapes differ for the shutter geometries but are mostly similar for the different chip thicknesses. The corresponding chip dose rate is the respective average of these curves (Fig. 8C). For a shutter with a thickness of 0.9 mm the simulated dose rate between chips with a thickness of 1 mm and 0.8 mm deviates by 15.3 % and only 5.8 % for a shutter with a thickness of 1.1 mm.

We ran additional tests for the varying chip diameters (we list $\dot{D}_{Sr-90}$ for extreme chip geometries in the appendix). We found only a weak impact of the shutter thickness on the induces dose rates. This finding confirms our results from Sec. 4 where we showed that differences in chip thickness explain more dose variance than differences in chip diameters. While a thicker shutter shows a dose rate less dependable on the chip geometry, it also reduces the dose rate by a factor of ca 2 per 1 mm. Vice versa, the results leave little doubt that our new source housing module has a thinner shutter installed, hence we observed the jump of the dose rate after the replacement service.

The simulated dose rates are at least 50 % lower than the measured values in Fig. 7. To some extent, this discrepancy is likely a result of the simplified geometry used for the simulation (e.g., instead of a cup, we used a disc-like geometry for the sample carrier). Nonetheless, we consider our simulations as qualitatively correct regarding the impact of the shutter thickness on the dose rate induced in chips of different thickness.

In conjunction with the observations presented in Sec. 4 these findings render a comprehensive picture, and demand a critical reflection on our procedure to measure Al_2O_3:C chips.

1. The simulated irradiation spectra questions our, so far applied, approach to consider geometry effects in the irradiation field negligible.
2. Depending on the shutter thickness, the passing high-energy β-particles induce considerable chip geometry related dose rates.
3. Although the source calibration results itself seem to show only a weak correlation with chip thickness (Fig. 7), the presented results strongly indicate that the dose scatter observed between chips is mainly an effect caused by the irradiation geometry in the measurement system.

Despite the overall acceptable reproducibility of natural $\dot{D}_\gamma$s (Sec. 2), in light of our findings we suggest the following additional measures when using Al_2O_3:C chips for *in situ* dose-rate measurements:

1. Different batches of chips must not be mixed and kept well separated.
2. Users should double-check their chip geometries and recalibrate their systems for their respective geometries.
3. It appears to be advisable, to double the number of tubes stored per sampling position (e.g., two tubes instead of one), so that the mean dose-rate can be obtained with higher confidence.
4. Since it appears that a thicker shutter can markedly reduce the geometry effects, it might be desirable to liaise with the manufacturer when ordering a new system or exchange the source housing. This might be also advisable from the radiation protection point of view.

Overall, the findings show that the origin of the scatter is not easy to fathom, and our results still may not tell the entire story. Compared to data measured in 2017, perhaps the chips

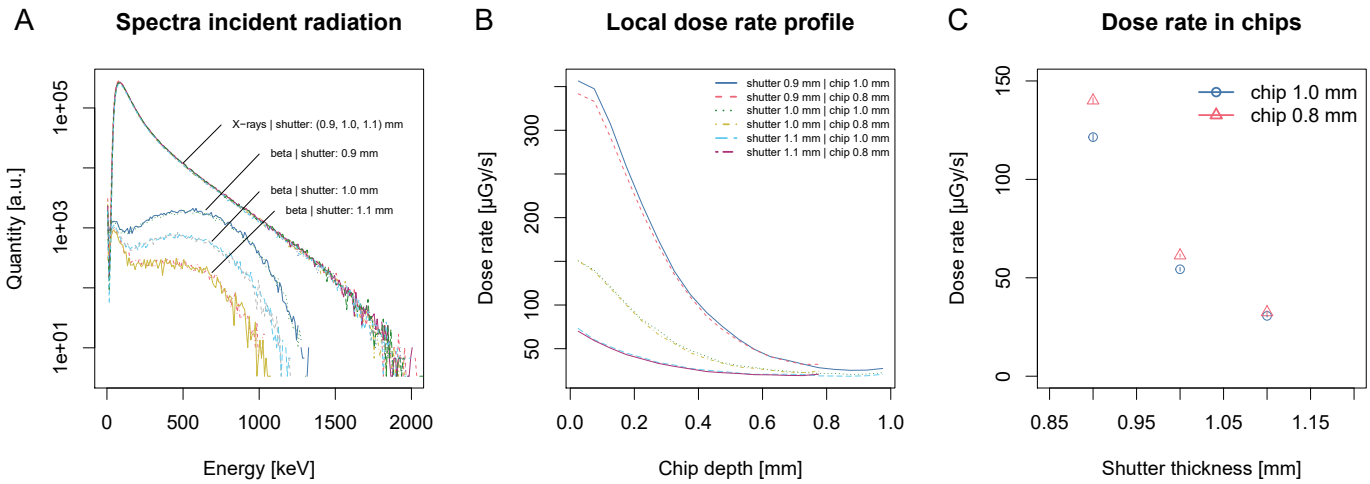

Figure 8. Results of the *GEANT4* simulations. The figures show the effect of different irradiation scenarios in the *lexsyg SMART* reader used for the measurements. (A) displays the spectra of the incident particles (here β-particles and X-ray photons) at the sample position for different shutter thicknesses. Colours code shutter geometries and chip geometries (1.0 mm and 0.8 mm). (B) Local dose rate profile for different irradiation geometries. (C) Induced chip dose rate as a dependent of the shutter thickness for two different chip geometries.

also suffer from some kind of degeneration contributing to the observed higher dose dispersion. Such a degeneration might be caused by the regular heating of the chips to 910 °C before being shipped to the field. However, such treatment is applied to empty the deep electron traps (Akselrod et al., 1990a), and even though this is considered a routine procedure, not being reported hazardous to the chips (Erfurt et al., 2000; Kalchgruber & Wagner, 2006; Yukihara & McKeever, 2011), one may wonder whether it causes an unexpected ageing of the chips. We are going to investigate this issue in the future.

In summary, the presented results emphasize another time that users should always remain suspicious regarding their measurement equipment (see also Kreutzer et al., 2017), in particular when dealing with new or modified systems. Moreover, the results underline another time the importance of regular source calibrations (for a recent discussion see Tribolo et al., 2019).

6. The Al_2O_3:C Analysis App

Along with their article, Kreutzer et al. (2018) deployed three new **R** functions for the package 'Luminescence' tailored to analyse calibration and routine dosimeter measurements. However, setting knowledge on **R** and the **R** package 'Luminescence' in particular as a prerequisite for analysing dosimeter measurements put up a barrier to a quick adoption in a laboratory that regularly hosts international guest researchers, students, and interns. Consequently, we decided to develop a so-called, shiny (Chang et al., 2019) application called 'Al_2O_3:C Analysis App' which is a graphical user interface to the **R** function `analyse_Al2O3C_Measurement()` in the 'Luminescence' package. In our laboratory, the application runs on a local *RStudio*® (`https://www.rstudio.com`) server. Users access the application platform-independent using a state-of-the-art browser of their choice. The 'Al_2O_3:C Analysis App' has three main panels for data import, data analysis, and post-processing including an export option of the results (cf. Fig. 9).

The user has various possibilities to interact with the software, such as copy & paste tabulated values or swipe through the graphical output. Furthermore, the software automatically provides access to all available system calibration datasets (cf. Kreutzer et al., 2018), such as irradiation time correction, cross-talk correction, and source calibration, so far they are stored on the same server. The software sets no limits regarding the number of datasets to access, and multiple reader data are accessible within the same environment. If no calibration datasets are available, data can still be analysed, but are of limited scientific value. Own calibration datasets, produced using the procedure detailed in Kreutzer et al. (2018) can be uploaded and used at any time during one session.

The application is available free of charge via `https://github.com/crp2a/Al2O3_AnalysisApp`. As usual, we published the software under the General Public Licence (GPL-3), which means it can be even modified and adapted following the licence conditions.

7. Conclusions

We presented new findings from follow-up experiments testing the reliability of our workflow employed to measure the environmental γ-dose rate using passive dosimeters detailed by Kreutzer et al. (2018). If tested against natural reference sites, a known γ-dose rate is reproducible within ca 7 %. Our cosmic-ray experiment, however, indicated a much larger scatter between aliquots, which can amount up to 15 % in low-level background environments. We did not find a statistical significant correlation between the chip orientation and the recorded dose. *GEANT4* simulations gave

Figure 9. Screenshots of the shiny application 'Al_2O_3:C Analysis App' freely available at https://github.com/crp2a/Al2O3_AnalysisApp.

evidence that the majority of the scatter can be explained by different chip geometries in conjunction with an unfortunate fabrication tolerance of the shutter in front of the radioactive source. The replacement of the source housing led to an increased dose-rate induced in the chips. The thinner shutter, (1) increased the number of high-energy β -particles passing the shutter, and (2) caused a higher dependency of the induced dose rate on the chip thickness. This explained why we observed (1) an increased dose-rate induced in the chips by ca 37 % after the replacement of the source housing and (2) a difference in the induced dose rate of at least 15 % for chips of 0.8 mm and 1 mm while irradiated in the reader. We suggested a couple of measures to reduce the inter-aliquot scatter, and with this systematic effects likely not related to the real dose-rate variations in the field. However, this aspect will receive further attention in the future.

Nevertheless, the employed experiments, along with the good reproducibility of calibration results, show the still overall justified applicability of our approach. The presented shiny application may serve those who do not want to learn **R** first before analysing their data.

Finally, our contribution falls in line with uncounted articles, many of them in Ancient TL, addressing potential sources of systematic uncertainties when determining luminescence ages. These days, more and more sophisticated numerical methods, such as Bayesian modelling (e.g., Combès et al., 2015; Combès & Philippe, 2017; Philippe et al., 2019), are adopted by the luminescence community. For those methods, a profound understanding and quantification of sources of systematic uncertainties are not just a 'nice to have', but an essential prerequisite to deploy their full potential and deliver correct overall calculations.

Author contributions

SK prepared the initial manuscript and developed the shiny application, CT organised the re-check at the reference sites and ran part of the measurements, calibrations as well as the first data analysis. LM designed, ran and analysed the *GEANT4* simulations. NM initiated and supervised the work. All authors discussed the results and equally contributed to the final manuscript.

Acknowledgements

We thank Dr Yukihara for valuable comments on our manuscript. Didier Miallier is thanked another time for his valuable support with the dosimeters at the reference sites around Clermont-Ferrand. This work received financial support by the LaScArBx LabEx, a programme supported by the ANR - n° ANR-10-LABX-52, and by the project DAPRES_LA_FEM, funded by the Region Nouvelle Aquitaine. While the manuscript was completed, SK has received funding from the European Union's Horizon 2020 research and innovation programme under the Marie Skłodowska-Curie grant agreement No 844457.

Appendix

Table 1. Values for $\dot{D}_{Sr-90}$ for extreme chip configurations.

	Shutter thickness [mm]		
Parameter	**0.9**	**1.0**	**1.1**
$\dot{D}_{C_{max}}$ [μGy s^{-1}]	154.9	65.3	34.0
(uncert. - 95 % CL)	(3.0)	(0.4)	(0.3)
$\dot{D}_{C_{min}}$ [μGy s^{-1}]	106.7	49.6	29.6
(uncert. - 95 % CL)	(1.1)	(0.5)	(0.5)
Diff. (C_{max}, C_{min})	**31 %**	**24 %**	**13 %**
(uncert. - 95 % CL)	(2 %)	(1 %)	(2 %)

C_{min}: tck. = 1.14 mm | ρ = 5.03 g cm^{-3} | dim. = 5.11 mm
C_{min}: tck. = 0.80 mm | ρ = 4.17 g cm^{-3} | dim. = 4.73 mm
CL: confidence level | tck.: thickness | dim.: diameter

References

Agostinelli, S., Allison, J., Amako, K., Apostolakis, J., Araujo, H., Arce, P., Asai, M., Axen, D., Banerjee, S., Barrand, G., Behner, F., Bellagamba, L., Boudreau, J., Broglia, L., Brunengo, A., Burkhardt, H., Chauvie, S., Chuma, J., Chytracek, R., Cooperman, G., Cosmo, G., Degtyarenko, P., Dell'Acqua, A., Depaola, G., Dietrich, D., Enami, R., Feliciello, A., Ferguson, C., Fesefeldt, H., Folger, G., Foppiano, F., Forti, A., Garelli, S., Giani, S., Giannitrapani, R., Gibin, D., Gómez Cadenas, J. J., González, I., Gracia Abril, G., Greeniaus, G., Greiner, W., Grichine, V., Grossheim, A., Guatelli, S., Gumplinger, P., Hamatsu, R., Hashimoto, K., Hasui, H., Heikkinen, A., Howard, A., Ivanchenko, V., Johnson, A., Jones, F. W., Kallenbach, J., Kanaya, N., Kawabata, M., Kawabata, Y., Kawaguti, M., Kelner, S., Kent, P., Kimura, A., Kodama, T., Kokoulin, R., Kossov, M., Kurashige, H., Lamanna, E., Lampén, T., Lara, V., Lefebure, V., Lei, F., Liendl, M., Lockman, W., Longo, F., Magni, S., Maire, M., Medernach, E., Minamimoto, K., Mora de Freitas, P., Morita, Y., Murakami, K., Nagamatu, M., Nartallo, R., Nieminen, P., Nishimura, T., Ohtsubo, K., Okamura, M., O'Neale, S., Oohata, Y., Paech, K., Perl, J., Pfeiffer, A., Pia, M. G., Ranjard, F., Rybin, A., Sadilov, S., Di Salvo, E., Santin, G., Sasaki, T., Savvas, N., Sawada, Y., Scherer, S., Sei, S., Sirotenko, V., Smith, D., Starkov, N., Stoecker, H., Sulkimo, J., Takahata, M., Tanaka, S., Tcherniaev, E., Safai Tehrani, E., Tropeano, M., Truscott, P., Uno, H., Urban, L., Urban, P., Verderi, M., Walkden, A., Wander, W., Weber, H., Wellisch, J. P., Wenaus, T., Williams, D. C., Wright, D., Yamada, T., Yoshida, H., and Zschiesche, D. *Geant4—a simulation toolkit*. Nuclear Instruments and Methods in Physics Research Section A: Accelerators, Spectrometers, Detectors and Associated Equipment, 506(3): 250–303, 2003. doi: 10.1016/S0168-9002(03)01368-8.

Aguirre, E. and Carbonell, E. *Early human expansions into Eurasia: The Atapuerca evidence*. Quaternary International, 75(1): 11–18, 2001. doi: 10.1016/S1040-6182(00)00073-2.

Akselrod, M. S., Kortov, V. S., Kravetsky, D. J., and Gotlib, V. I. *Highly Sensitive Thermoluminescent Anion-Defective Alpha-Al_2O_3:C Single Crystal Detectors*. Radiation Protection Dosimetry, 32(1): 15–20, 1990a. doi: 10.1093/oxfordjournals.rpd.a080715.

Akselrod, M. S., Kortov, V. S., Kravetsky, D. J., and Gotlib, V. I. *Highly Sensitive Thermoluminescent Anion-Defect Alpha-Al_2O_3:C Single Crystal Detectors*. Radiation Protection Dosimetry, 33(1-4): 119–122, 1990b. doi: 10.1093/oxfordjournals.rpd.a080771.

Akselrod, M. S., Kortov, V., and Gorelova, E. *Preparation and Properties of $\alpha - Al_2O_3 : C$*. Radiation Protection Dosimetry, 47(1-4): 159–164, 1993. doi: 10.1093/oxfordjournals.rpd.a081723.

Auguie, B. *gridExtra: Miscellaneous Functions for "Grid" Graphics*, 2017. URL https://CRAN.R-project.org/package=gridExtra. R package version 2.3.

Backwell, L. R., d'Errico, F., Banks, W. E., de la Peña, P., Sievers, C., Stratford, D., Lennox, S. J., Wojcieszak, M., Bordy, E. M., Bradfield, J., and Wadley, L. *New Excavations at Border Cave, KwaZulu-Natal, South Africa*. Journal of Field Archaeology, 0 (0): 1–20, 2018. doi: 10.1080/00934690.2018.1504544.

Chang, W., Cheng, J., Allaire, J., Xie, Y., and McPherson, J. *shiny: Web Application Framework for R*, 2019. URL https://CRAN.R-project.org/package=shiny. R package version 1.3.2.

Combès, B. and Philippe, A. *Bayesian analysis of individual and systematic multiplicative errors for estimating ages with stratigraphic constraints in optically stimulated luminescence dating*. Quaternary Geochronology, 39: 24–34, 2017. doi: 10.1016/j.quageo.2017.02.003.

Combès, B., Philippe, A., Lanos, P., Mercier, N., Tribolo, C., Guérin, G., Guibert, P., and Lahaye, C. *A Bayesian central equivalent dose model for optically stimulated luminescence dating*. 28: 62–70, 2015. doi: 10.1016/j.quageo.2015.04.001.

Dietze, M., Kreutzer, S., Burow, C., Fuchs, M. C., Fischer, M., and Schmidt, C. *The abanico plot: visualising chronometric data with individual standard errors*. Quaternary Geochronology, 31: 12–18, 2016. doi: 10.1016/j.quageo.2015.09.003.

Erfurt, G., Krbetschek, M. R., Trautmann, T., and Stolz, W. *Radioluminescence (RL) behaviour of Al_2O_3:C-potential for dosimetric applications*. Radiation Measurements, 32(5–6): 735–739, 2000. doi: 10.1016/S1350-4487(00)00052-4.

Frerebeau, N. *khroma: Colour Schemes for Scientific Data Visualization*. Université Bordeaux Montaigne, Pessac, France, 2019. URL https://CRAN.R-project.org/package=khroma. R package version 1.3.0.

Galbraith, R. F. *The radial plot: Graphical assessment of spread in ages*. International Journal of Radiation Applications and Instrumentation. Part D. Nuclear Tracks and Radiation Measurements, 17(3): 207–214, 1990. doi: 10.1016/1359-0189(90)90036-W.

Grün, R. and Beaumont, P. *Border Cave revisited: a revised ESR chronology*. Journal of Human Evolution, 40(6): 467–482, 2001. doi: 10.1006/jhev.2001.0471.

Huntley, D. J., Godfrey-Smith, D. I., and Thewalt, M. L. W. *Optical dating of sediments*. Nature, 313: 105–107, 1985. doi: 10.1038/313105a0.

Kalchgruber, R. and Wagner, G. A. *Separate assessment of natural beta and gamma dose-rates with TL from single-crystal chips*. Radiation Measurements, 41(2): 154–162, 2006. doi: 10.1016/j.radmeas.2005.04.002.

Kreutzer, S., Schmidt, C., Fuchs, M. C., Dietze, M., Fischer, M., and Fuchs, M. *Introducing an R package for luminescence dating analysis*. Ancient TL, 30(1): 1–8, 2012. URL http://ancienttl.org/ATL_30-1_2012/ATL_30-1_Kreutzer_p1-8.pdf.

Kreutzer, S., Murari, M. K., Frouin, M., Fuchs, M., and Mercier, N. *Always remain suspicious: a case study on tracking down a technical artefact while measuring IR-RF*. Ancient TL, 35(1): 20–30, 2017. URL http://www.ecu.edu/cs-cas/physics/ancient-timeline/upload/ATL_35-1_Kreutzer_p20-30.pdf.

Kreutzer, S., Martin, L., Guérin, G., Tribolo, C., Selva, P., and Mercier, N. *Environmental Dose Rate Determination Using a Passive Dosimeter: Techniques and Workflow for alpha-Al_2O_3:C Chips*. Geochronometria, 45: 56–67, 2018. doi: 10.1515/geochr-2015-0086.

Kreutzer, S., Burow, C., Dietze, M., Fuchs, M. C., Schmidt, C., Fischer, M., and Friedrich, J. *Luminescence: Comprehensive Luminescence Dating Data Analysis*, 2019. URL https://CRAN.R-project.org/package=Luminescence. R package version 0.9.3.

Miallier, D., Guérin, G., Mercier, N., Pilleyre, T., and Sanzelle, S. *The Clermont radiometric reference rocks: a convenient tool for dosimetric purposes*. Ancient TL, 27: 37–44, 2009. URL http://ancienttl.org/ATL_27-2_2009/ATL_27-2_Miallier_p37-44.pdf.

Murray, A. S. and Wintle, A. G. *Luminescence dating of quartz using an improved single-aliquot regenerative-dose protocol*. Radiation Measurements, 32(1): 57–73, 2000. doi: 10.1016/S1350-4487(99)00253-X.

Philippe, A., Guérin, G., and Kreutzer, S. *BayLum - An R package for Bayesian analysis of OSL ages: An introduction*. Quaternary Geochronology, 49: 16–24, 2019. doi: 10.1016/j.quageo.2018.05.009.

R Core Team. *R: A Language and Environment for Statistical Computing*. Vienna, Austria, 2019. URL https://r-project.org.

Richter, D., Dombrowski, H., Neumaier, S., Guibert, P., and Zink, A. C. *Environmental gamma dosimetry with OSL of -Al2O3:C for in situ sediment measurements*. Radiation Protection Dosimetry, 141(1): 27–35, 2010. doi: 10.1093/rpd/ncq146.

Richter, D., Pintaske, R., Dornich, K., and Krbetschek, M. R. *A novel beta source design for uniform irradiation in dosimetric applications*. Ancient TL, 30(2): 57–63, 2012. URL http://ancienttl.org/ATL_30-2_2012/ATL_30-2_Richter_p57-64.pdf.

Richter, D., Richter, A., and Dornich, K. *Lexsyg smart — a luminescence detection system for dosimetry, material research and dating application*. Geochronometria, 42(1): 202–209, 2015. doi: 10.1515/geochr-2015-0022.

Tribolo, C., Kreutzer, S., and Mercier, N. *How reliable are our beta-source calibrations?* Ancient TL, 37(1): 1–10, 2019. URL http://ancienttl.org/ATL_37-1_2019/ATL_37-1_Tribolo_p1-10.pdf.

Wickham, H. *ggplot2: Elegant Graphics for Data Analysis*. Springer New York, New York, NY, 2009.

Wickham, H. and Bryan, J. *readxl: Read Excel Files*, 2019. URL https://CRAN.R-project.org/package=readxl. R package version 1.3.1.

Yukihara, E. G. and McKeever, S. W. S. *Optically Stimulated Luminescence*. Optically Stimulated Luminescence. Wiley, 2011.

Reviewer

Eduardo Gardenali Yukihara

Reviewer comment

At this temperature [meant are 910°C] one does not expect much senstivitiy change, but with time it has been observed that a dead layer develops due to diffusion of oxygen. This can be tested by comparing the sensitvitiy of the chips with the sensitivity of polished chips exposed to α-particles.

licensed under CC BY 4.0

Ancient TL

Radiofluorescence of quartz from rocks and sediments and its correlation with thermoluminescence and optically stimulated luminescence sensitivities

Pontien Niyonzima[1*], André O. Sawakuchi[1], Mayank Jain[2], Raju Kumar[2], Thays D. Mineli[1], Ian del Río[1] and Fabiano N. Pupim [1,3]

[1] Luminescence and Gamma Spectrometry Laboratory (LEGaL), Instituto de Geociências, Universidade de São Paulo, São Paulo,Rua do Lago 562, São Paulo, SP 05508-080, Brazil

[2] Department of Physics, Technical University of Denmark, DTU Risø Campus, DK-4000 Roskilde, Denmark

[3] Departamento de Ciências Ambientais, Universidade Federal de São Paulo, Diadema, Rua São Nicolau, 210, São Paulo 09913-030, Brazil

*Corresponding Author: pontienn@usp.br

Received: May 22, 2020; in final form: June 18, 2020

Abstract

The present study examines radiofluorescence (RF) emissions in quartz from parent rocks (igneous plutonic and volcanic) and sediments of different provenances, which represent a range of optically stimulated luminescence (OSL) and thermoluminescence (TL) sensitivities observed in nature. OSL and TL (110 °C peak) sensitivities of quartz have been successfully used for sediment provenance analysis, but the considerable sensitivity variations are still poorly understood in terms of charge traps and recombination centers. In the studied samples, the RF spectra obtained at room temperature and using X-ray irradiation consist of two broad emission bands: the first emission band is centered at ∼1.9 eV (blue) and has a higher intensity compared to the second emission band centered at ∼3.5 eV (ultraviolet, UV). The deconvolution analysis confirms that the quartz RF spectrum is at least the sum of four emission bands located between 1.5 eV (827 nm) and 4.0 eV (310 nm). The general observation is that the RF intensity differs between quartz from rocks and sediments, and among quartz from sediments with different provenances. Generally, quartz from sediments showed higher RF intensity compared to quartz from rocks, rendering the same pattern observed for OSL and TL sensitivities. For quartz from sediments, we observed strong correlations between the UV-RF band intensity and the OSL or 110 °C TL sensitivities. We argue that these correlations may be attributed to the fact that both 110 °C TL peak and OSL of quartz use the same recombination centers rather than the same electron trap. The UV-RF intensity measured using X-ray sources can also be used for provenance analysis of sediments in the same way as the OSL and TL sensitivities.

Keywords: Quartz in sediments, Sediment provenance, Luminescence of quartz, Radiofluorescence spectra, X-ray irradiation

1. Introduction

Since the first proposals for the use of thermoluminescence (TL) (e.g., Grögler et al. 1958; Fleming 1970; Mejhdahl 1979; Wintle & Huntley 1979) and optically stimulated luminescence (OSL) in quartz (Huntley et al., 1985) as dating techniques, it appears that both TL and OSL signals are not merely due to charge eviction from traps after stimulation with consequent luminescence recombination. However, more complex mechanisms are involved (Martini et al., 2009). Aitken & Smith (1988) reported parallel changes in the OSL sensitivity and the sensitivity of the 110 °C TL peak and suggested that this might be related to a common mechanism. Most researchers agree on the involvement of the same recombination centers of these two processes (e.g.,

Table 1. Description of studied samples, indicating types of rocks and sediments, approximate age of crystallization (rocks) or deposition (sediments), location of the sampling sites, and average TL and OSL sensitivities and standard deviation as presented in unpublished work by Mineli et al. Aliquots used to measure TL, and OSL sensitivities contained approximately 150 to 200 grains, as observed under an optical microscope, with an average mass of 8.1 ± 0.9 mg. TL and OSL sensitivities data were not obtained for sample L0680, which was collected in the same geological setting of sample L0674. Both samples are examples of sediments with low sensitivity quartz. For both TL and OSL measurements, 2 to 6 aliquots were measured for each sample and results presented in the table are average with standard.

	Code	Name	Age	Location	TL 110 °C (cts Gy^{-1})	OSL (cts Gy^{-1})
Rocks	VR12	Granite	Neoproterozoic	Ribeira Fold Belt, Guaraú Massif, (Cajati, São Paulo, Brazil)	1865 ± 1851	67 ± 70
	ITA1	Granite	Neoproterozoic	Ribeira Fold Belt, Itacoatiara Massif, (Niterói, Rio de Janeiro, Brazil)	2019 ± 261	4.4
	LA1	Rhyolite	Pleistocene	Los Alamos (New Mexico, USA)	1795 ± 319	63 ± 25
	IP22	Hydro-thermal quartz	Permian	Teresina Formation, Paraná Basin (Anhembi, São Paulo, Brazil)	108	2.2
Sediments	L0001	Coastal sand	Pleistocene	South Atlantic Coast (Southern Brazil)	128760 ± 42674	23152 ± 9361
	L0017	Fluvial sand	Pleistocene	Central Amazon (Northern Brazil)	22426 ± 5354	1390 ± 502
	L0698	Fluvial sand	Holocene	Western Amazon (Northern Brazil)	12396 ± 4036	2432 ± 1309
	L0229	Fluvial sand	Pleistocene	Pantanal Wetland (Western Brazil)	308683 ± 51341	53520 ± 9522
	L0688	Fluvial sand	Holocene	Paraná River Basin (Southern Brazil)	433092 ± 53278	89544 ± 53278
	L0572	Fluvial sand	Pleistocene	Central Amazon (Northern Brazil)		
	L0674	Alluvial sand	Pleistocene	Mejillones Peninsula, Andes (Chile)	266 ± 44	17 ± 9
	L0680	Colluvial sand	Pleistocene	Salar Del Carmen, Andes (Chile)	*	*

Chen et al. 2000). Radiofluorescence (RF), the light emission during irradiation, has been investigated in quartz samples from rocks and sediments as well as in artificially growing SiO_2 crystals (Marazuev et al., 1995; Krbetschek & Trautmann, 2000; Martini et al., 2012b) for dosimetry and dating purposes. RF has also been investigated for a better understanding of the luminescence dynamics in quartz (Martini et al., 2012a,b; Chithambo & Niyonzima, 2017) by comparing the 3.44 eV RF peak intensity measured after series of irradiation and thermal treatments in order to understand the specific role of various defect centers. Different from TL and OSL, the RF emission seems to correspond predominantly to the direct recombination of electrons from the conduction band with the holes at the recombination centers during irradiation (e.g., Schmidt et al. 2015; Friedrich et al. 2017).

Deconvolution of the RF spectra showed the presence

of the same emission bands from both natural and "artificial" (laboratory crystal growth) quartz crystals, indicating that the same luminescence processes are involved (Martini et al., 2012a,b; Chithambo & Niyonzima, 2017). The similarity among RF, TL and OSL emission spectra (Huntley et al., 1991; Krbetschek et al., 1997; Schilles et al., 2001) provided evidence that these luminescence signals share the same recombination centers (Friedrich et al., 2017). This similarity suggests that changes in OSL and TL sensitivities in nature, as observed in quartz from sediments (e.g., Pietsch et al. 2008; Zular et al. 2015) are probably related to the recombination process rather than trapping process. In this way, investigation of the relationship between RF and OSL and TL sensitivities can shed light on the role of recombination centers for the natural sensitization processes. In addition to its widespread application for dating of Quaternary sediments (Aitken, 1998), luminescence signals from quartz are used for tracing the provenance of sediments (e.g., Lü & Sun 2011, Gray et al. 2019). In the previous works, TL spectra (Rink et al., 1993), the proportion of OSL components (Tsukamoto et al., 2011), the OSL and TL sensitivities (Sawakuchi et al., 2012; Zular et al., 2015; Mendes et al., 2019) and OSL signal components (Nian et al., 2019) of quartz have been used in discriminating sediment sources and provenance analysis. Thus, several luminescence properties (*e.g.*, sensitivity, thermal activation, spectral variation, and signal components) can be used to discriminate quartz from different provenances. A general pattern is that quartz extracted from different types of igneous and metamorphic rocks has a relatively low luminescence sensitivity (Chithambo et al., 2007; Guralnik et al., 2015) compared to quartz from sediments, which shows a wide range of OSL sensitivity variation (Sawakuchi et al., 2011). Thus, recent studies have successfully applied OSL sensitivity in sediment provenance analysis through discrimination of sediments with different transport histories since their parent rocks (e.g., Sawakuchi et al. 2018; Mendes et al. 2019).

In this study, we investigate the variation of RF emission spectra in quartz extracted from different igneous rocks, which are primary sources of terrigenous sediments, and sediments of different geological settings, ranging from tectonic active mountain ranges to stable craton areas in South America. This suite of samples has a broad range in natural TL and OSL sensitivities, as presented in Sawakuchi et al. (2020) and unpublished work by Mineli et al. and summarized in Table 1. Correlation between UV-RF and sensitivity of both TL and OSL is also investigated in this study. We hypothesis that, this correlation would support the use of RF of quartz for sediment provenance analysis.

2. Experimental details

2.1. Sample description and preparation

Samples used in this investigation were quartz from igneous rocks (granite, rhyolite, and hydrothermal vein) representing different conditions of quartz crystallization and sediments (alluvial, fluvial and coastal sands) of different depositional environments from South American sites (Table 1). OSL and TL sensitivities of these samples were previously studied by Mineli et al. (pers. comm.) and they are summarized in Table 1.

Step	OSL and TL sensitivities [a]
1	Bleach with blue LEDs at 125 °C for 100 s
2	Dose: 10 Gy
3	TL up to 190 °C (5 °C/s) (110 °C TL sensitivity)
4	Blue stimulation at 125 °C for 100 s (OSL sensitivity)
5	Blue stimulation at 125 °C for 100 s (background)

Table 2. Measurement protocol used by Mineli et al. (pers. comm.) for determination of TL (step 3) and OSL (step 4) sensitivities. The 110 °C TL sensitivity was determined through the integration of the 75 – 125 °C interval of the TL glow curve and the OSL sensitivity through the first second of light emission of the OSL decay curve

Rock samples were crushed to release quartz crystals, which were manually picked for careful grinding using a pestle and ceramic mortar. Quartz crystals from igneous rocks and quartz grains from sediments in the range of 180 – 250 μm were extracted by wet sieving. The target fraction was treated with hydrogen peroxide (H_2O_2, 27%) and hydrochloric acid (HCl, 10%) to remove organic matter and carbonate minerals, respectively. Heavy minerals and feldspar grains were removed by heavy liquid separation with lithium metatungstate solutions with densities of 2.75 g/cm^3 and 2.62 g/cm^3, respectively. To purify and concentrate the quartz fraction, samples were etched in 38% hydrofluoric acid (HF) for 40 min. Infrared stimulation (IR) was performed to confirm the absence of feldspar contamination in the HF treated quartz fraction. Samples with remaining feldspar were subjected to steps of HF 5% etching for 24 hours followed by wet sieving (180 μm sieve), and in some cases, samples were repeatedly HF-etched until a negligible infrared signal was achieved, compared with blue stimulation signal.

2.2. Instrumentation

Radiofluorescence measurements were carried out using the Risø station for CryOgenic Luminescence Research COLUR at Center for Nuclear Technologies, Technical University of Denmark (DTU), Risø campus. It consists of a Horiba Fluorolog-3 spectrometer expanded to include multi-excitation and detection ports, an X-ray irradiator (40 kV anode voltage, 100 μA anode current, and ca 0.06 Gy/s dose rate to quartz), and a temperature-controlled closed-loop He cryostat (7 – 300 K) (Prasad et al., 2016).

All the radiofluorescence measurements reported in this paper were obtained using X-ray irradiation at room temperature and a CCD detector. Quartz grains were mounted on a steel cup using double-sided tape. Measurements were performed with a constant dose rate (ca 0.06 Gy/s), integration

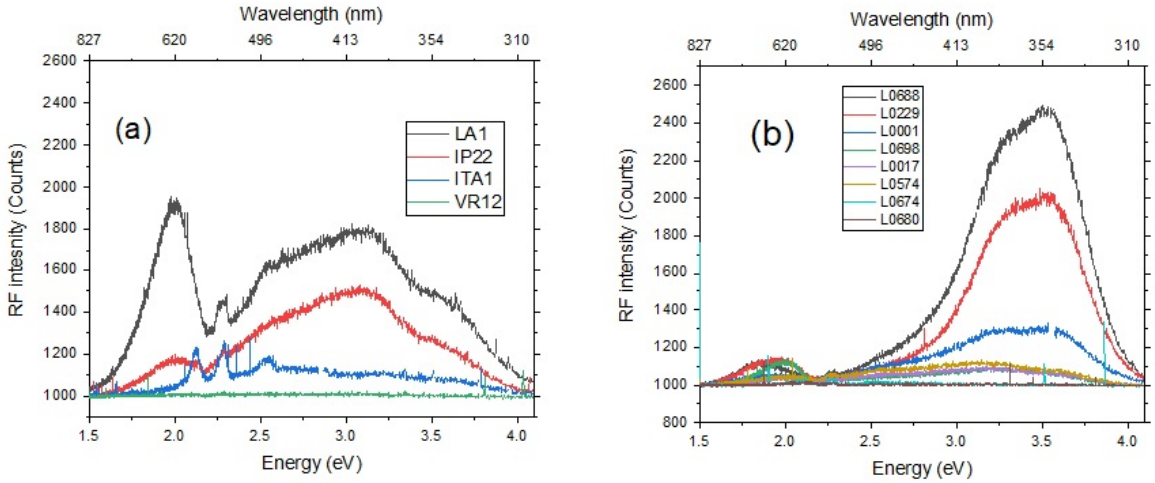

Figure 1. Comparison of the RF emission spectra measured in quartz from rocks (a) and sediments (b).

times of 30 s ($\sim$ 1.8 Gy) for quartz sediment grains (samples L0001, L0017, L0229, L0572, L0674, L0680, L0688, and L0698) and 300 s ($\sim$ 18 Gy) for quartz rock crystals (samples VR12, ITA1, LA1, and IP22) and full-range detection (300-1,000 nm). Integration times were higher for quartz from rocks to acquire significant RF spectra. Background emission was acquired by measuring empty cups with tape. Samples were exposed to daylight, but they were not submitted to any thermal or irradiation treatment before the acquisition of RF spectra. RF spectra were deconvoluted into Gaussian components using the least square method with the Levenberg-Marquardt algorithm (Origin software 2018).

The same quartz samples used for RF measurements were previously submitted to OSL and TL sensitivity measurements performed in the two Risø TL/OSL DA-20 readers at the Luminescence and Gamma Spectrometry Laboratory (LEGaL) of the Institute of Geosciences, University of São Paulo, Brazil. The OSL and TL sensitivity data are summarized in Table 1. The measurement protocol is described in Table 1. Aliquots of similar masses were used in order to minimize the effect of aliquot size on luminescence signal sensitivity. The readers are equipped with a beta-radiation source (^{90}Sr/^{90}Y) with dose rates of ca 0.132 Gy/s and ca 0.077 Gy/s, blue (470 nm, max. 80 mW cm^{-2}) and infrared (870 nm, max. 145 mW cm^{-2}) LEDs for stimulation and Hoya U-340 filters (200 – 400 nm) for light detection in the ultraviolet band. Regarding the instrument response spectra correction, RF and OSL/TL measurements were done on different equipment, and the absolute counts of RF and OSL sensitivities are not directly comparable. However, the main goal of this study is the relative comparison between RF and OSL/TL. In the TL and OSL measurements carried out by Mineli et al. (pers. comm.), quartz aliquots were mounted on 9.7 mm diameter stainless steel discs using silicone oil. Each aliquot contained approximately 150 to 200 grains, as observed under an optical microscope, with an average mass of 8.1 $\pm$ 0.9 mg (see procedures for aliquot preparation in Mendes et al. (2019).

3. Results

The comparison between RF spectra of quartz from rocks and sediments is shown in Figure 1. Both types of quartz show similar RF in higher energy part of the spectrum (2.5 – 4.0 eV), despite the difference in their intensities and number of overlapping peaks, while in the lower part of the spectrum

Bands	Sediment sample L0688		Rock sample LA1	
	Energy (eV)	FWHM (eV)	Energy (eV)	FWHM (eV)
Peak 1	1.87	0.32	1.97	0.34
Peak 2	2.55	0.99	2.53	0.48
Peak 3	3.36	0.37	3.07	0.71
Peak 4	3.62	0.42	3.70	0.49

Table 3. Energy values of the detected emission bands for quartz from rock (LA1) and sediment (L0688) samples.

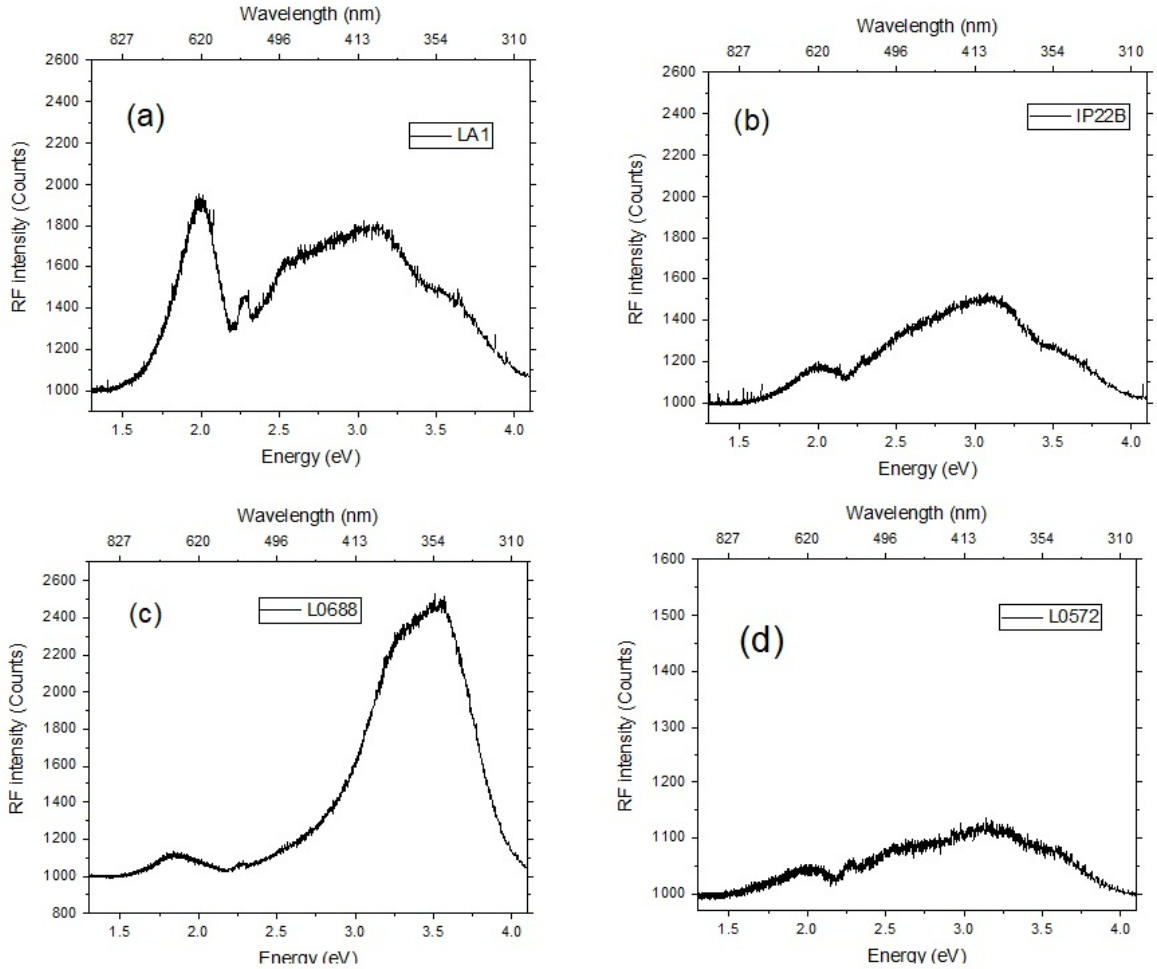

Figure 2. Spectra to illustrate the differences in RF intensities for quartz from rocks and sediments. RF spectra of quartz from rhyolite (a) and hydrothermal vein (b) have relatively low RF intensity compared to quartz from sediments of stable tectonic areas in southern Brazil (c). However, quartz from sediments of the Chilean Andes (d) has low RF intensity, comparable to quartz from rocks. The sample description can be found in Table 1.

(1.5 – 2.5 eV), non-similarity in the RF spectra was observed.

The luminescence spectra of quartz samples used in this study showed a broad unstructured emission ranging from 1.5 eV (827 nm) to 4.1 eV (310 nm), with maximum RF intensity close to 2.0 eV (620 nm) for quartz from rocks (Figure 1a) and 3.6 eV (354 nm) for quartz from sediments (Figure 1b). For the emission spectra of quartz from rocks (Figure 1a), we identified five different emission bands represented by a broader band in the range of 1.6 – 2.1 eV (red), a narrow emission band centered at 2.3 eV and bands at 2.4 – 2.8 eV (blue), 3.0-3.4 eV (UV-violet) and 3.4 – 3.8 eV (UV). The visual analysis of the emission spectra of quartz from sediments resulted in the identification of four different emissions at 1.6 – 2.2 eV (red), around 2.3 – 2.7 eV (blue), 3.0 – 3.3 eV (UV-violet) and 3.5 – 3.8 eV (UV) (Figure 1b). The RF intensity in some samples was not strong enough to perform a curve fitting analysis (Figure 1).

Generally, quartz from sediments of central and southern Brazil, represented by samples from the Paraná River (L0688), Southern Atlantic coast (L0001) and Pantanal Wetland (L0229), showed high UV-RF emission intensity compared to sediments from Chilean Andes, i.e., Mejillones Peninsula (L0674) and Salar Del Carmen (L0680). For quartz from Brazilian sediments, the exceptions are the samples from northern Brazil, i.e., central Amazon (L0572) and western Amazon (L0017 and L0698), that showed low RF intensity compared to that of quartz from central and southern Brazil used in this study. For the samples from rocks, quartz from granite (VR12 and ITA1) shows low RF intensity compared to quartz from rhyolite (LA1) and hydrothermal vein (IP22). Figure 2 shows the main characteristics of RF spectra recorded for quartz from rocks (LA1 and IP22) and sediments with higher (L0688) and lower (L0572) RF intensities.

All the RF emission spectra from quartz extracted from both rocks and sediments have been deconvoluted into their main components (Figure 3). The fitting of the RF emission spectra was performed assuming four bands, and the Gaus-

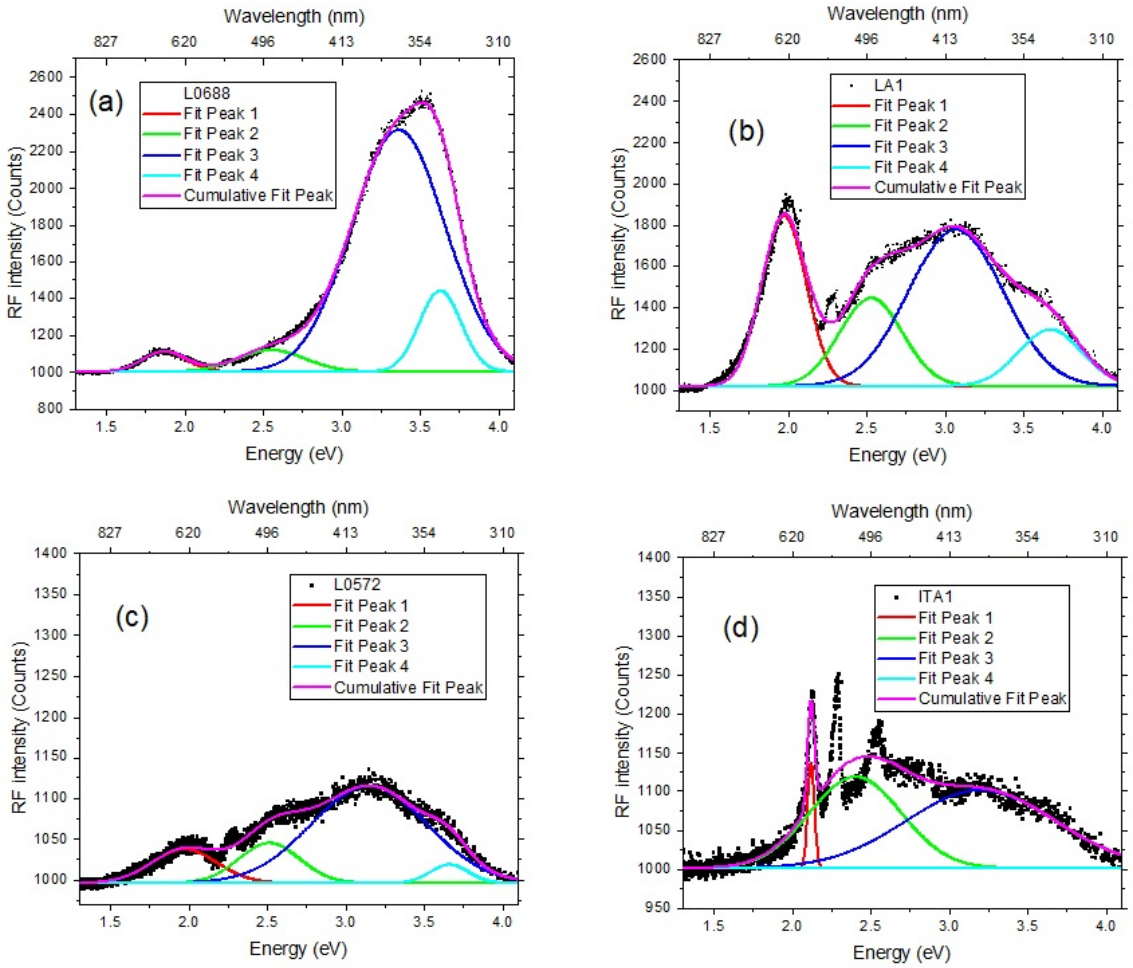

Figure 3. Gaussian components of high-intensity RF emission spectra of quartz from sediments of the Paraná River Basin (a) and rhyolite of Los Alamos (b). Gaussian components of low-intensity RF emission spectra of quartz from sediments of Central Amazon (c) and granite of the Ribeira Fold Belt (d).

sian fitting agrees with experimental curves for samples with high RF intensity (Figure 3a).

The energy and full width at half-maximum for the four emission bands used in the deconvolution of the RF spectra are presented in Table 1, i.e., 1.87 eV (0.32 eV), 2.55 eV (0.99 eV), 3.36 eV (0.37 eV), 3.62 eV (0.42 eV) for quartz from sediments (L0688) and 1.97 eV (0.34 eV), 2,53 eV (0.48 eV), 3.07 eV(0.71 eV) and 3.7 eV (0.49 eV) for quartz from rocks (LA1). Martini et al. (2012b) reported five emission bands in natural quartz, i.e., 1.95 eV (0.48 eV), 2.53 eV (0.46 eV), 2.80 eV (0.45 eV), 3.44 eV (0.58 eV) and 3.94 eV (0.49 eV). Values within brackets are full width at half-maximum of the emission bands. More studies are needed to investigate the reasons behind the difference in the number of RF emission bands and values of their full width at half-maximum for quartz from Brazil and quartz from other regions.

For the quartz from rocks and quartz from sediment samples (e.g., L0572, Figure 3c) with low RF intensity, Gaussian fittings are not entirely satisfactory in the energy region ranging from 2.1 eV to 2.4 eV (Figure 3b, c, and d), where small and sharp peaks might be sample related or instrumental artifacts. Other candidates to explain the presence of these sharp peaks are the presence of other mineral phases as inclusions in quartz, such as zircon or apatite. However, additional mineral inclusion analysis is required to confirm or reject this statement.

Bands with peaks at 3.36 eV and 3.6 eV are the most intense in the sediment samples, and a band with a peak at 1.9 eV is the most intense for rock samples. Bands with peaks at 2.5 eV, 3.07 eV, and 3.7 eV are overlapping, as observed in quartz from rhyolite (Figure 3b). The RF intensities of bands with peaks at 3.07 eV and 3.70 eV for quartz from rocks and at 3.36 eV and 3.62 eV for quartz from sediments were used to investigate the relationship between UV-RF and the sensitivities of the 110 °C TL peak and OSL (initial 1 s of light emission) assessed by Mineli et al. (pers. comm.) (Figure 4).

A linear correlation, with a correlation coefficient (r) ranging from 0.95 to 0.99, between UV-RF and the sensitivities of the 110 °C TL peak, and the OSL (first 1s) is observed

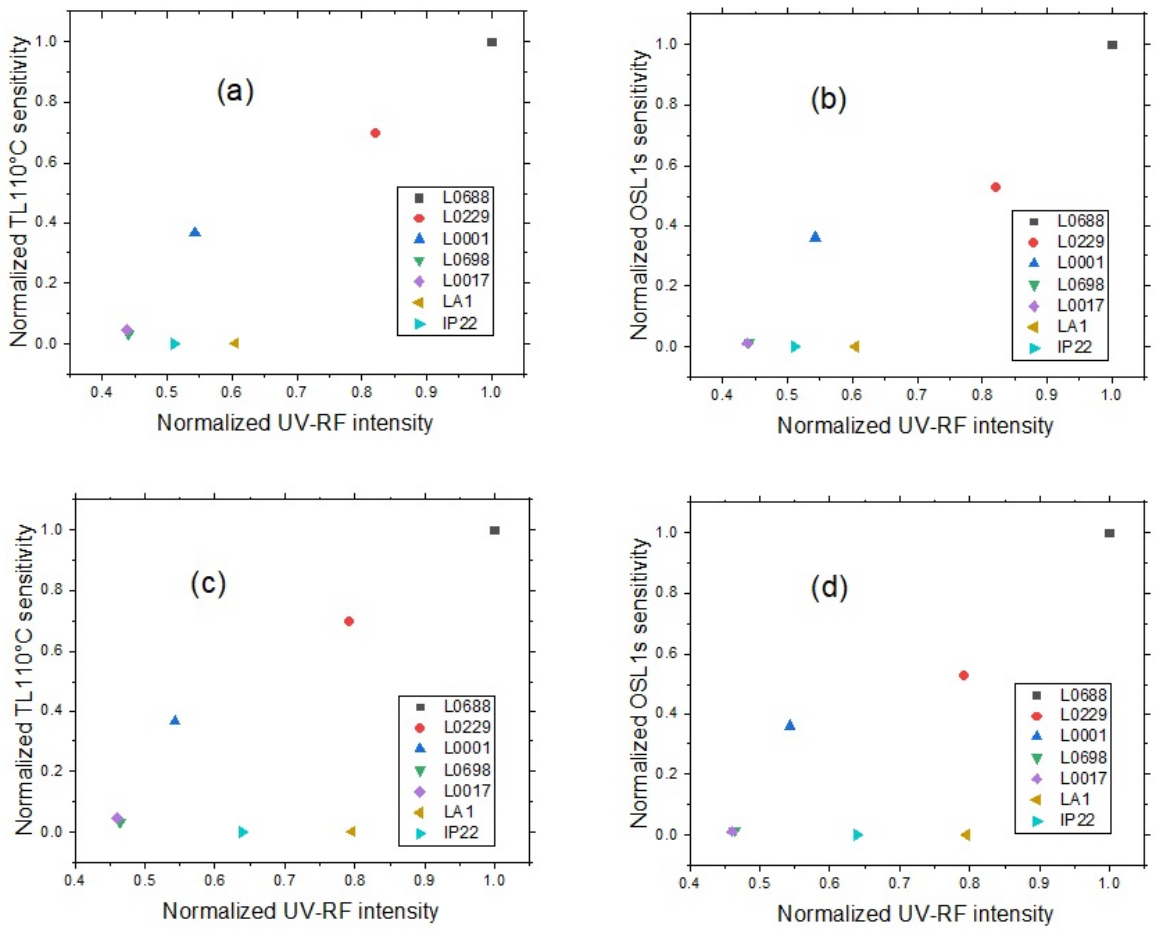

Figure 4. Relationship between 3.6 eV RF emission band intensity and sensitivities of 110 °C TL peak (a) and OSL (b); and between 3.36 eV RF emission band intensity and sensitivities of 110 °C TL peak (c) and OSL (d). The sensitivity of the OSL signal was taken from the integral of the initial second of the OSL decay curve divided by the given radiation dose. The sensitivity of the 110 °C TL peak (heating rate of 5°C/s) was determined from the integration of the 75 – 125 °C interval divided by the given dose. The TL and OSL sensitivities and UV-RF intensity were normalized to their corresponding highest signal for easy comparison.

for quartz extracted from sediments (Figure 5). However, no correlation was observed for quartz from rocks (LA1 and IP22) (Figure 4). The results from Figure 5 indicate that samples with high UV-RF intensity are more sensitive in the case of both 110 °C TL and OSL (first 1s).

4. Discussion and conclusions

In quartz, the correlation between the sensitivities of the 110 °C TL peak and the first 1s of the OSL decay curve has been widely acknowledged, indicating that the fast OSL component and 110 °C TL peak sensitize in a similar manner (Jain et al., 2003). In this study, we present the correlation between both OSL and TL sensitivities with RF intensity of quartz from sediments, which support the use of RF as provenance proxy in the same way as OSL and TL sensitivities.

The RF and TL emissions were found to be similar in the violet, blue, and red regions, suggesting that their recombination centers must be closely related to each other (Shimizu et al., 2006). According to Huntley et al. (1991), the OSL spectra of quartz have been observed in the ultraviolet region, so that the UV-RF (3.6 eV and 3.36 eV) emissions might also be related to the UV-OSL emission. In this study, we observed a linear correlation between the OSL sensitivity, presumably dominated by the fast component, and UV-RF (3.6 eV and 3.36 eV) intensity for quartz from sediments. We also observed a linear correlation between UV-RF and sensitivity of 110 °C TL, which strongly supports the suggestion that sensitization processes in nature might be due to changes in recombination process (density of recombination centers for example) rather than changes in the charge trapping probability like proposed by Moska & Murray (2006).

In the present work, we also observe low RF intensity of quartz from rocks compared to quartz from sediments, which is a pattern also observed for the OSL sensitivity of quartz (Sawakuchi et al., 2011). The RF sensitization, when quartz is released from parent rocks to sedimentary systems, occurs

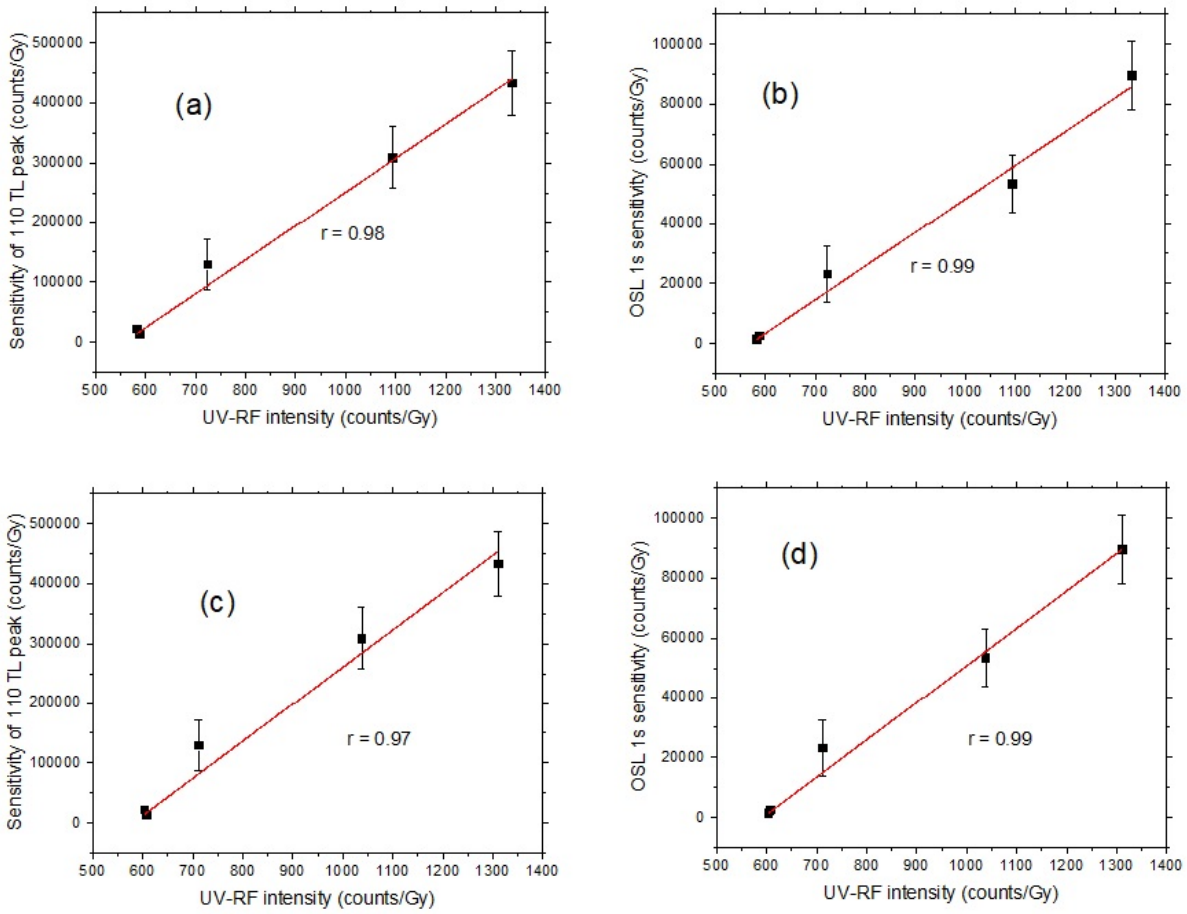

Figure 5. Correlation between 3.6 eV RF emission intensity and the 110 °C TL peak (a) and OSL (b) sensitivities of quartz from sediments. The intensity of the 3.36 eV emission band was also plotted for comparison with the 110 °C TL peak (c) and of OSL (d) sensitivities. The data for all graphs were fitted with a linear equation. For the UV-RF measurement, we only measured one aliquot for each sample.

mainly in the UV and blue emission bands (320 – 400 nm). However, quartz from sediments recently released from their parent rocks in active tectonic settings (L0017 and L0698) have RF intensity in the same range of quartz from rocks. Additional studies are needed to confirm that a single natural process is promoting the sensitization of quartz TL, OSL, and RF.

In conclusion, the results of this study indicate that quartz RF intensity mirrors sensitivity patterns observed for OSL and TL signals in nature and the UV-RF intensity measured using X-ray sources can also be used for provenance analysis of sediments in the same way as the OSL and TL sensitivities.

Acknowledgments

We appreciate the thoughtful and detailed comments and suggestions by Dr. Sebastian Kreutzer, who greatly contributed to improving the quality of our work. PN is grateful to the National Council for Science and Technology Development (CNPq), The World Academy of Sciences (TWAS) (CNPq/TWAS grant 154507/2017-2), and The São Paulo Research Foundation (FAPESP grant 2019/04059-6) for funding the Ph.D. fellowship at the University of São Paulo. AOS is supported by the National Council for Science and Technology Development (CNPq grant 304727/2017-2).

References

Aitken, M. J. *An introduction to optical dating: the dating of quaternary sediments by the use of photon-stimulated luminescence*. Oxford University Press, 1998.

Aitken, M. J. and Smith, B. M. *Optical dating: Recuperation after bleaching*. Quaternary Science Reviews, 7: 387–393, 1988.

Chen, G., Li, S. H., and Murray, A. S. *Study of the 110°C TL peak sensitivity in optical dating of quartz*. Radiation Measurements, 32: 641–645, 2000.

Chithambo, M. and Niyonzima, P. *Radioluminescence of annealed synthetic quartz*. Radiation Measurements, 106: 35–39, 2017.

Chithambo, M. L., Preusser, F., Ramseyer, K., and Ogundare, F. O. *Time-resolved luminescence of low sensitivity quartz from crystalline rocks*. Radiation Measurements, 42: 205–212, 2007.

Fleming, S. J. *Thermoluminescence dating: refinement of the quartz inclusion method*. Archaeometry, 12: 133–145, 1970.

Friedrich, J., Fasoli, M., Kreutzer, S., and Schmidt, C. *The basic principles of quartz radiofluorescence dynamics in the UV - analytical, numerical and experimental results*. Journal of Luminescence, 192: 940–948, 2017.

Gray, H. J., Jain, M., Sawakuchi, A. O., Mahan, S. A., and Tucker, G. E. *Luminescence as a sediment tracer and provenance tool*. Reviews of Geophysics, 57: 987–1017, 2019.

Grögler, N., Houtermans, F. G., and Stauffer, H. *Radiation damage as a research tool for geology and prehistory*. In *Convengo sulle dotazioni con metodi nuclear. th Internazation Elettr Nucl Sezione Nuclear Roma*, pp. 5–15, 1958.

Guralnik, B., Ankjærgaard, C., Jain, M., Murray, A. S., Müller, A., Wälle, M., and Herman, F. *OSL-thermochronometry using bedrock quartz: A note of caution*. Quaternary Geochronology, 25: 37–48, 2015.

Huntley, D. J., Godfrey, S. D. I., and Thewalt, M. L. W. *Optical dating of sediments*. Nature, 313: 105–107, 1985.

Huntley, D. J., Godfrey-Smith, D. I., and Haskell, E. H. *Light-induced emission spectra from some quartz and feldspars*. Nuclear Tracks Radiation Measurements, 18: 127–131, 1991.

Jain, M., Murray, A. S., and Bøtter-Jensen, L. *Characterization of blue-light stimulated luminescence component in different quartz samples: Implications for dose measurement*. Radiation Measurements, 37: 441–449, 2003.

Krbetschek, M. R. and Trautmann, T. *A spectral radioluminescence study for dating and dosimetry*. Radiation Measurements, 32: 853–857, 2000.

Krbetschek, M. R., Götze, J., Dietrich, A., and Trautmann, T. *Spectral information from minerals relevant for luminescence dating*. Radiation Measurements, 27: 695–748, 1997.

Lü, T. and Sun, J. *Luminescence sensitivities of quartz grains from eolian deposits in northern China and their implications for provenance.* Quaternary Research, 76: 181–189, 2011.

Marazuev, Y. A., Brik, A. B., and Degota, V. Y. *Radioluminescent dosimetry of Alpha - quartz*. Radiation Measurements, 24: 565–569, 1995.

Martini, M., Fasoli, M., and Galli, A. *Quartz OSL emission spectra and the role of $[AlO4]^0$ recombination centres*. Radiation Measurements, 44: 458–461, 2009.

Martini, M., Fasoli, M., Galli, A., Villa, I., and Guibert, P. *Radioluminescence of synthetic quartz related to alkali ions*. Journal of Luminescence, 132: 1030–1036, 2012a.

Martini, M., Fasoli, M., Villa, I., and Guibert, P. *Radioluminescence of synthetic and natural quartz*. Radiation Measurements, 47: 846–850, 2012b.

Mejhdahl, V. *Thermoluminescence dating: Beta-dose attenuation in quartz grains*. Archaeometry, 21: 61–72, 1979.

Mendes, V. R., Sawakuchi, A. O., Chiessi, C. M., Giannini, P. C. F., Rehfeld, K., and Mulitza, S. *Thermoluminescence and optically stimulated luminescence measured in marine sediments indicate precipitation changes over northeastern Brazil*. Paleoceanography and Paleoclimatology, 34, 2019.

Moska, P. and Murray, A. S. *Stability of the quartz fast-component in insensitive samples*. Radiation Measurements, 41: 878–885, 2006.

Nian, X., Zhang, W., Qiu, F., Qin, J., Wang, Z., Sun, Q., Chen, J., Chen, Z., and Liu, N. *Luminescence characteristics of quartz from Holocene delta deposits of the Yangtze River and their provenance implications.* Quaternary Geochronology, 49: 131–137, 2019.

Pietsch, T. J., Olley, J. M., and Nanson, G. C. *Fluvial transport as a natural luminescence sensitizer of quartz.* Quaternary Geochronology, 3: 365–391, 2008.

Prasad, A. K., Lapp, T., Kook, M., and Jain, M. *Probing luminescence centers in Na rich feldspar.* Radiation Measurements, 90: 292–297, 2016.

Rink, W. J., Rendell, H., Marseglia, E. A., Luff, B. J., and Townsend, P. D. *Thermoluminescence Spectra of Igneous Quartz and Hydrothermal Vein Quartz*. Physics and Chemistry of Minerals, 20: 353–361, 1993.

Sawakuchi, A. O., Blair, M. W., DeWitt, R., Faleiros, F. M., Hyppolito, T., and Guedes, C. C. F. *Thermal history versus sedimentary history: OSL sensitivity of quartz grains extracted from rocks and sediments*. Quaternary Geochronology, 6: 261–272, 2011.

Sawakuchi, A. O., Guedes, C. C. F., Dewitt, R., Giannini, P. C. F., Blair, M. W., , and Faleiros, F. M. *Quartz OSL sensitivity as a proxy for storm activity on the southern Brazilian coast during the Late Holocene*. Quaternary. Geochronology, 13: 92–102, 2012.

Sawakuchi, A. O., Jain, M., Mineli, T. D., Nogueira, L., Jr, B., J., D., Häggi, C., Sawakuchi, H. O., Pupim, F. N., Grohmann, C. H., Chiessi, C. M., c, M. Z., Mulitza, S., Mazoca, C. E. M., and Cunha, D. F. *Luminescence of quartz and feldspar fingerprints provenance and correlates with the source area denudation in the Amazon River basin*. Earth and Planetary Science Letters, 492: 152–162, 2018.

Sawakuchi, A. O., Rodrigues, F. C. G., Mineli, T. D., Mendes, V. R., Melo, D. B., Chiessi, C. M., and Giannini, P. *Optically stimulated luminescence sensitivity of quartz for provenance analysis.* Methods and Protocols, 3: 6, 2020. doi: https://doi.org/10.3390/mps3010006.

Schilles, T., Poolton, N. R. J., Bulur, E., Bøtter-Jensen, L., Murray, A. S., Smith, G. M., Riedi, P. C., and Wagner, G. A. *A multi-spectroscopic study of luminescence sensitivity changes in natural quartz induced by high-temperature annealing*. Journal of Physics D: Applied Physics, 34: 722–731, 2001.

Schmidt, C., Kreutzer, S., DeWitt, R., and Fuchs, M. *Radiofluorescence of quartz: A review*. Quaternary Geochronology, 27: 66–77, 2015.

Shimizu, N., Mitamura, N., Takeuchi, A., and Hashimoto, T. *Dependence of radioluminescence on TL-properties in natural quartz*. Radiation Measurements, 41: 831–835, 2006.

Tsukamoto, S., Nagashima, K., Murray, A. S., and Tada, R. *Variations in OSL components of quartz from Japan sea sediments and the possibility of reconstructing provenance*. Quaternary International, 234: 182–189, 2011.

Wintle, A. G. and Huntley, D. J. *Thermoluminescence dating of deep sea sediments*. Nature, 279: 710–712, 1979.

Zular, A., Sawakuchi, A. O., Guedes, C. C. F., and Giannini, P. C. F. *Attaining provenance proxies from OSL and TL sensitivities: coupling with grain size and heavy minerals data from southern Brazilian coastal sediments*. Radiation Measurements, 81: 39–45, 2015.

Reviewer

Sebastian Kreutzer

licensed under CC BY 4.0

Ancient TL

eM-Age (excel Macro for Age calculation), a new application for luminescence age calculation based on Dose Rate and Age Calculator (*DRAC*) and *Analyst*

Carlos Pérez-Garrido[1*]

[1] Instituto Geológico y Minero de España, IGME, C\La Calera, 1, 28760 Tres Cantos (Madrid), Spain

*Corresponding Author: carlos.perez@igme.es

Received: January 24, 2020; in final form: June 18, 2020

Abstract

***eM-Age* is a new program for calculating luminescence ages quickly and more easily. It allows the user to instantly check the impact of choosing different attenuation factors (dose rate parameters, grain size, water content, etc) on the final dose rate, and therefore also on the final age, calculation. Based on data collected by Durcan et al. (2015) in the *DRAC* program, *eM-Age* offers a graphical interface and also allows the calculation and selection of equivalent dose data from summaries generated by *Analyst*, as well as offering options for different age models for the loaded data.**

Keywords: Quaternary, data treatment, data analysis, geochronology, luminescence dating, software

1. Introduction

Age calculation using dating techniques such as thermoluminescence (TL) or Optically Stimulated Luminescence (OSL) can be a challenge due to the large number of individual factors which need to be taken into account, such as grain size attenuation, etch depth attenuation, burial depth, water content, dose rates of the different radionuclides present in the sediment etc. In recent years, new applications and add-ons have emerged to help researchers in these processes, reducing the potential for miscalculations and providing useful tools for inter-laboratory comparisons and data sharing. Within this aim, specific programs have been developed for the different dating techniques, as well as add-ons such as *AGE* program (Grün, 2009), *ADELE* (Kulig, 2005), Dose Rate and Age Calculator, *DRAC* (Durcan et al., 2015), `'Luminescence'` and `'RLumShiny'` packages for **R** (Kreutzer et al., 2012, 2019), *CRONUS* (Balco et al., 2008), *LDAC* (Liang & Forman, 2019), and the implementation of **R** features within *Analyst* (v4.57) (Duller, 2018).

Here I present a new program for luminescence age calculation based on *DRAC* datasets (Durcan et al., 2015), but with a simpler Graphical User Interface (GUI), for users with and without a high degree of knowledge of luminescence calculation programs like *Analyst* or **R** `'Luminescence'` package, and are more familiar with commercial packages such as *Microsoft Office*®.

2. Key features

eM-Age has been designed to be run on *Microsoft Excel*® (2007 and later) as a macro. For proper operation, users must have enabled macros in Excel. *eM-Age* is an easy and friendly way to perform most of the calculus and parameter evaluation involved in age calculation for luminescence dating techniques (especially OSL), both equivalent dose (D_e) and dose rate calculation. Users can input their data directly, and in addition, D_e data can be uploaded from *Analyst .binx* files.

One of the main features of *eM-Age* is to allow the user to check continuously (during the whole data input process) the effect of data changes on both the total dose rate and the final age calculation. This is an improvement with respect to other programs where the user needs to input all the data prior to obtaining a final result (e.g., *DRAC*, **R** `'Luminescence'`, *LDAC*), and provides a rapid way of sensitivity testing the impact of various different datasets on the final calculated dose rate.

Moreover, *eM-Age* offers the possibility of uploading data sets from *Analyst* (equivalent doses, recycling, test dose errors, palaeodose errors, recuperation %, reader dose rate if available, disc and grain position). Radionuclei (U,

Th, K and Rb) values can be input as either concentrations (ppm/%) or activities (Bq/kg) for dose rate calculation, offering more flexibility than other programs where the data input is restricted to a fixed format (e.g. radionuclide concentrations in ppm or weight percentage only). *eM-Age* avoids the use of complex syntaxes for equivalent dose calculation (e.g. from `'Luminescence'`, package for **R**: `calc_AverageDose[data, sigma_m = NULL, Nb_BE = 500, na.rm = TRUE, plot = TRUE, verbose = TRUE, ...]`), which requires a certain degree of knowledge of programming codes. In addition, the original data set often needs pre-treatment prior to use within **R**. The most recent enhancement of *Analyst* (Duller, 2018) includes the possibility of using the **R** `'Luminescence'` package (Kreutzer et al., 2012, 2019), making it a powerful tool for researchers, and clearly enhances the use of advanced functions included in the `'Luminescence'` package of **R**. Nonetheless, certain knowledge of **R** is required to obtain the desired results.

The aim of this program is to offer a straightforward, intuitive software, in which equivalent doses and dose rates can be calculated for luminescence dating. It is aimed at a broad range of researchers, without the requirement for coding skills. It is intended that this program will be developed in the future, with future versions having more capabilities. A repository in GitHub (`https://github.com/yomismovk/eM-Age-program`) has been created with this aim to house the original files and future updates.

3. Quick guide and program structure

To run the program it is necessary to click on the button "Run eM-Age program" located in the main tab called "eM-Age program info". In the first run, the program automatically uploads a default stored dataset (example data from SAR-2.binx file, *Analyst* (v4.57) - Duller 2018). The program window (Figure 1) is divided into two main sections; (1) an upper part with permanent (always visible) data (showing in green sample name, final age (in ka), equivalent dose (Gy) and total dose rate values (Gy/ka), and (2) a section with different tabs for data input (Data, Dosimetry, Results & Graphs and Summary). Listed below is a brief description of the different tabs and the required data.

3.1. "Data" tab

This tab is designed to introduce basic data information of the sample, such as name, project name, type of analysis (single aliquot, single grain), type of protocol (TL, OSL, VSL, TT-OSL), type of material (quartz, feldspars, others). Data included in this tab will be output in the user summary. Also, this tab allows the user to upload equivalent dose data from external sources (summaries from *Analyst* (v4.57) and later, exported as *.anr* files). The equivalent dose data (D_e in seconds and Gy) is shown, as well as different quality parameters like recycling ratio, test dose error, palaeodose error and recuperation % (for further information see *Analyst* (v4.57) manual).

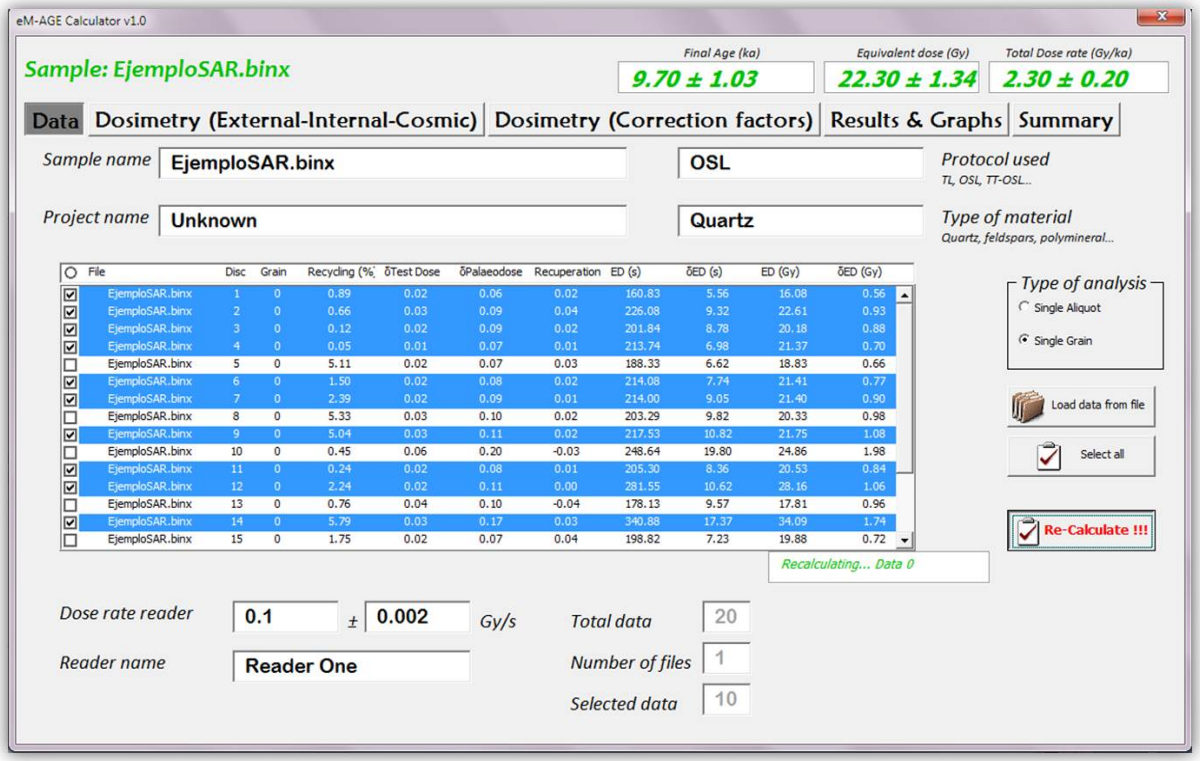

Figure 1. *eM-Age* main screen with an Analyst file uploaded

If the uploaded file contains data referring to the source dose rate from the luminescence reader, it will be shown and used for the calculations. If not, a "N.D." (no data) caption will appear in the dose rate reader field, and a message will inform the user that an estimated dose rate of 0.100(2) Gy/s will be used. The user also has the option of manually inputting their source dose rate. Additionally, if the user does wish to import their equivalent dose data, it is possible to input an equivalent dose value for the sample in the "Results & Graphs" tab (User Equivalent Dose).

3.2. "Dosimetry" tabs

Dosimetry calculation is handled in the tabs "Dosimetry-Correction Factors", for water content and correction factors of the infinite matrix alpha, beta and gamma doses calculated from the data input, and "Dosimetry-External-Internal-Cosmic", that includes both external, internal and cosmic dosimetry parameters.

The "Dosimetry-Correction Factors" tab allows the user to input the information related to sample water content. This last point will define the percentage of water content used for age calculation (Zimmerman, 1971; Aitken & Xie, 1990). In this section, the user can input the "Saturation water content" (maximum percentage of water accepted by the sediment), organics content (estimated % of organic matter in the sample), and % saturation (estimated percentage of water during the burial time, 100% = sediment always saturated in water, 0% = sediment always dry). This tab enables the modification of parameters such as sample grain size, choose between different dose rate conversion factors (Adamiec & Aitken, 1998; Guérin et al., 2011; Liritzis et al., 2013), attenuation factors for grain size and etching (Bell & Zimmerman, 1978; Mejdahl, 1979; Bell, 1979, 1980; Brennan et al., 1991; Readhead, 2002a,b; Brennan, 2003; Guérin et al., 2012), shallow depth correction factor for samples with depth $\leq$ 30 cm (Aitken, 1985; Durcan et al., 2015), and the type of attenuation applied (independently from K, U and Th concentrations or using an average attenuation factor "MIX" calculated assuming the elemental ratios of Mejdahl 1979). Also shown in this tab, is a graphical presentation of the relative contribution (%) to the total dose of the different sources (alpha, beta, gamma, internal and cosmic doses).

The "Dosimetry-External-Internal-Cosmic" tab enables the input of parameters relevant to the cosmic dose rate, as well as the external and internal dosimetry. Several factors are taken into account for cosmic dose rate calculation such as altitude, burial depth, sediment density and sample coordinates (latitude and longitude). Geomagnetic corrections based on the workings of Prescott & Hutton (1988, 1994) are used.

External and internal dosimetry data can be inserted in two different ways: 1) as U, Th, Rb (ppm) and K (%) concentrations, or 2) as U, Th, K and Rb activities (Bq/kg). Also, this last method allows the users to use only ^{238}U, ^{232}Th and ^{40}K activities, if the user does not have data of the complete decay chain of ^{238}U and ^{232}Th.

3.3. "Results & Graphs" tab

This tab shows valuable information about the sample data set (if the data was uploaded from an external source, *.anr* files), including probability distribution and histogram plots for both raw uploaded data and selected equivalent dose data ("Raw data" and "Selected data" tabs).

Also, in the "Selected data" tab, users can compare different ages obtained by using different age models: Mean, Weight mean, Common age model and Central age model (Galbraith et al., 1999) and to choose between them. Moreover, for this last age model the overdispersion is calculated.

3.4. "Summary" tab

eM-Age allows the export of a *.pdf* file with all the information provided by the user and the main parameters used in the age calculation, such as alpha, beta, gamma, cosmic, internal dose rates, equivalent doses selected for the age calculation (if an *Analyst* file is uploaded) as well as a list of the different correction factors applied. This will help the researchers to organize their results and to compare different samples. Also, during the process of calculation the program generates (in the folder where it is located) a number of files with *.gif* format to be used in another programs or reports made by the user.

4. Conclusions

eM-Age offers a new opportunity for easily calculating luminescence ages. The simplicity of its interface together with the multiple data entry options offer researchers, and specifically the geochronologists, a fast and reliable tool for the basic calculation of luminescence ages. It is simple and intuitive enough for under- and postgraduate students to use, as they develop their skills and knowledge in luminescence dating. It can also serve to complement more advanced research in conjunction with existing programs.

The presentation of this calculator as a macro in Excel and the free access of the code used (`https://github.com/yomismovk/eM-Age-program`) offers the possibility of modification and improvement of the program's capabilities by other users and the chance of adaptation to particular requirements.

5. Data Availability

Dose rate conversion factor data were obtained directly from the original works of: Adamiec & Aitken (1998); Guérin et al. (2011); Adamiec & Aitken (1998); Guérin et al. (2011); Liritzis et al. (2013). Grain size attenuation factors, etch depth attenuation factors, cosmic dose rate parameters (F, J and H) and gamma dose scaling factors were obtained and slightly modified (format only) from the supplementary information of Durcan et al. (2015) at `http://dx.doi.org/10.1016/j.quageo.2015.03.012`. All the datasets are visible in the background worksheets of the *eM-Age* calculator v1 Code Visible file.

Acknowledgments

This research did not receive any specific grant from funding agencies in the public, commercial, or not-for-profit sectors. I want to thank the reviewer for the suggestions and comment, that has contributed significantly to improve the quality of the program.

Appendix

The supplementary documents contain the following files: (1) program write-protected for general use (eM-AGE calculator v1.0 Protected) (2) program with visible code, spreadsheets, macro functions for advanced users (eM-AGE calculator v1.0 Visible Code) (3) Equivalent dose data file from Analyst summary (Example SAR-2.ANR) (4) Example of report (SAR-2.binx Report.pdf) (5) User Manual (eM-Age Manual v1.0). The Supplementary Documents are available as zip-file for download. A detailed description of the datasets used in the program can be found in the supplementary information of Durcan et al. (2015).

References

Adamiec, G. and Aitken, M. J. *Dose-rate conversion factors: update*. Ancient TL, 16: 37–46, 1998.

Aitken, M. J. *Thermoluminescence Dating*. Academic Press, New York. 351 p, 1985.

Aitken, M. J. and Xie, J. *Moisture correction for annual gamma dose*. Ancient TL, 8: 6–9, 1990.

Balco, G., Stone, J. O., Lifton, N. A., and Dunai, T. J. *A complete and easily accessible means of calculating surface exposure ages or erosion rates from ^{10}Be and ^{26}Al measurements*. Quaternary Geochronology, 3: 174–195, 2008.

Bell, W. T. *Attenuation factors for the absorbed radiation dose in quartz inclusions for thermoluminescence dating*. Ancient TL, 8: 1–12, 1979.

Bell, W. T. *Alpha attenuation in Quartz grains for Thermoluminescence Dating*. Ancient TL, 12: 4–8, 1980.

Bell, W. T. and Zimmerman, D. W. *The effect of HF acid etching on the morphology of quartz inclusions for thermoluminescence dating*. Archaeometry, 20: 63–65, 1978.

Brennan, B. J. *Beta doses to spherical grains*. Radiation Measurements, 37: 299–303, 2003.

Brennan, B. J., Lyons, R. G., and Phillips, S. W. *Attenuation of alpha particle track dose for spherical grains*. International Journal of Radiation Applications and Instrumentation. Part D. Nuclear Tracks and Radiation Measurements, 18: 249–253, 1991.

Duller, G. A. T. *Enhancing Analyst by integrating the R package 'Luminescence'*. Ancient TL, 36(2): 1–6, 2018.

Durcan, J. A., King, G. E., and Duller, G. A. T. *DRAC: An online Dose Rate and Age Calculator*. Quaternary Geochronology, 28: 54–61, 2015.

Galbraith, R. F., Roberts, R. G., Laslett, G. M., Yoshida, H., and Olley, J. M. *Optical dating of single and multiple grains of quartz from Jinmium rock shelter, northern Australia: Part I, Experimental design and statistical models*. Archaeometry, 41: 339–364, 1999.

Grün, R. *The "AGE" program for the calculation of luminescence age estimates*. Ancient TL, 27, 2009.

Guérin, G., Mercier, N., and Adamiec, G. *Dose-rate conversion factors: update*. Ancient TL, 29: 5–8, 2011.

Guérin, G., Mercier, N., Nathan, R., Adamiec, G., and Lefrais, Y. *On the use of infinite matrix assumption and associeted concepts: A critical review*. Radiation Measurements, 47(9): 778–785, 2012.

Kreutzer, S., Schmidt, C., Fuchs, M. C., Dietze, M., Fischer, M., and Fuchs, M. *Introducing an R package for luminescence dating analysis*. Ancient TL, 30(1): 1–8, 2012.

Kreutzer, S., Burow, C., Dietze, M., Fuchs, M., Schmidt, C., Fischer, M., and Friedrich, J. *Luminescence: Comprehensive Luminescence Dating Data Analysis.* R package version 0.9.6, 2019. URL https://CRAN.R-project.org/package=Luminescence.

Kulig, G. *Erstellung einer Auswertesoftware zur Altersbestimmung mittels Lumineszenzverfahren unter spezieller Berücksichtigung des Einflusses radioaktiver Ungleichgewichte in der ^{238}U-Zerfallsreihe (Creation of a software for luminescence dating with special attention to the influence of radioactive disequilibria in the ^{238}U decay chain)*. Technische Bergakademie Freiberg. Unpublished BSc Thesis, 2005.

Liang, P. and Forman, S. L. *LDAC: An Excel-based program for luminescence equivalent dose and burial age calculations*. Ancient TL, 37(2): 21–40, 2019.

Liritzis, I., Stamoulis, K., Papachristodoulou, C., and Ioannides, K. *A re-evaluation of radiation dose-rate conversion factors*. Mediterranean Archaeology and Archaeometry, 13: 1–15, 2013.

Mejdahl, V. *Thermoluminescence dating: beta-dose attenuation in quartz grains*. Archaeometry, 21: 61–72, 1979.

Prescott, J. R. and Hutton, J. T. *Cosmic ray and gamma ray dosimetry for TL and ESR*. Nuclear Tracks and Radiation Measurements, 14: 223–227, 1988.

Prescott, J. R. and Hutton, J. T. *Cosmic ray contributions to dose rates for luminescence and ESR dating: large depths and long-term time variations*. Radiation Measurements, 23: 497–500, 1994.

Readhead, M. L. *Absorbed dose fraction for 87Rb beta particles*. Ancient TL, 20: 25–29, 2002a.

Readhead, M. L. *Appendum to "Absorbed dose fraction for 87Rb beta particles"*. Ancient TL, 20: 47, 2002b.

Zimmerman, D. W. *Thermoluminescence dating using fine grains from pottery*. Archaeometry, 13: 29–52, 1971.

Reviewer

Julie Durcan

Thesis Abstracts

Index

Ingrid Bejarano Arias	p. 25
Galina Faershtein	p. 25
Nicola Horsburgh	p. 26
Jandessa Silva de Jesus	p. 27
Şule Kaya-Keleş	p. 27
Xue Rui	p. 28
Javier Andrés Sandoval Andrade	p. 28
Aayush Srivastava	p. 29
Roos Marina Johanna van Wees	p. 29

Ingrid Bejarano Arias

Determination of depositional environment and luminescence dating of Pleistocene deposits in the Biely Váh Valley, southern foothills of the Tatra Mountains, Slovakia

June 2020
Lund University, Lund, Sweden

Degree: M.Sc.
Supervisors: Helena Alexanderson, Isa Doverbratt and Juraj Janočko

The Tatra Mountains have had several glaciations during the Quaternary. The deposits located in the southern foothills were classified as glacifluvial, based on geomorphology, but its sediments have not been studied in detail. Therefore, this project focused on establishing the depositional history, processes, and age of the deposits in a gravel pit, located in the Biely Váh Valley in these foothills. The combination of luminescence dating with sedimentological analysis, including clast shape and maximum particle size, were the methods of choice. For the luminescence dating eleven samples were collected from the units composed mainly of sand.

Initially optically stimulated luminescence (OSL) dating was used, but after applying the standard Single Aliquot Regeneration (SAR) protocol quality tests, it was evident that the quartz was poorly behaved with low signal intensity. The dose estimation gave bad results, even after attempting pulsed OSL and differential OSL. Therefore, it was decided to move on to feldspar grains. Given that there is a risk of fading and the fact that feldspar grains take longer to bleach, the corrective measurements were done by calculating the g-value and use of IR_{50} and $pIRIR_{225}$ signals for the bleaching.

The sedimentological description yielded 13 units from the lower and upper outcrops in the study area. The results of the sedimentological analysis indicated that the process of deposition had a high energy component, representative of subaerial flows. Given the features of the sediments it was identified as a hyperconcentrated flow. Moreover, for the age determination the most likely water content of the sediments was chosen, the g-values and the equivalent dose were determined, using both IR_{50} and $pIRIR_{225}$ signals. Subsequently, four ages were obtained per sample, one for each signal, and with and without correction for fading. From these, the uncorrected $pIRIR_{225}$ ages were selected, since this signal has a lower fading rate which is supported by the obtained g-values, which were smaller than 1 – 1.5%.

The results were compared to the known glacial history of the Tatra Mountains. The obtained luminescence ages, which range from ca 200 to 260 ka, would correspond to the Riss glaciation. Both ages and sediment characteristics match those of the other deposits from the northern and southern Tatra foothills that also have been correlated to the Riss glaciation. Taken together, these results suggest a glacial advance to the present-day foothills of the High Tatras during the Riss glaciation and extensive deposition of glacifluvial sediments outside the ice margin.

Galina Faershtein

Extending luminescence dating into the early Pleistocene – method development and application to the eastern Mediterranean coastal plain

January 2020
Hebrew University, Jerusalem, Israel

Degree: Ph.D.
Supervisors: Naomi Porat, Ari Matmon

The aim of the thesis was to explore the extended-range luminescence dating techniques that have the potential of dating sediments throughout the middle to early Pleistocene. Numerical dating of continental clastic sediments of Pleistocene age, particularly early Pleistocene, has always been a challenge. The luminescence dating techniques, and particularly the optically stimulated luminescence (OSL), are strong tools for dating late Pleistocene to late Holocene sediments from different geological settings. However, the common OSL technique is usually limited to 100-200 ka due to signal saturation. Recent developments of new extended-range luminescence methods show great potential for dating older sediments of middle and even early Pleistocene. For quartz, the techniques include the thermally transferred OSL (TT-OSL) and violet stimulated luminescence (VSL). Using these signals, ages of up to 1 Ma have been reported. For alkali-feldspars, the post-infrared-infrared stimulated luminescence at elevated temperatures (pIRIR) protocols have been used

to obtain ages of over 500 ka. There are unsolved issues concerning the optimal use of these techniques such as exact measurement protocols, accuracy, and effective time range. This thesis deals with some of these problems in an attempt to resolve them.

The Israeli Coastal Plain sequence spans the entire Quaternary and comprises mainly aeolian sediments. The mineral grains (such as quartz and alkali-feldspar) are all derived from a single source: the Nile river. This setting is a perfect natural laboratory for investigating of the different luminescence signals. This study focussed on two representative sections: Kerem Shalom (sand) and Ruhama (loess). The extended range signals in quartz and feldspar were systematically investigated; the upper limits of the signals were defined through natural and laboratory saturation and thermal stability of their source traps.

In nature, luminescence signals usually reach saturation at lower doses than in the laboratory. Natural saturation profiles (created by plotting the natural normalized signals of samples against their depth) constructed for OSL and TT-OSL (for Kerem Shalom and Ruhama), as well as VSL and $pIRIR_{250}$ (for Kerem Shalom), were found to be a powerful tool for detecting saturated samples in the studied sections. Semi-natural dose response curves (DRC), constructed by plotting natural normalized signals against their laboratory equivalent doses (for OSL, TT-OSL, $pIRIR_{250,290}$), using samples from these two sections, as well as from other sites in the region, characterize Nilotic quartz and feldspar and define their typical DRC's. The semi-natural OSL DRC is unique to the quartz of Nilotic origin and indicates that the upper limit for reliable OSL dating of this quartz is 140 Gy due to signal saturation, corresponding to 45 – 280 ka (for typical environmental dose rates of 0.5-3 Gy ka^{-1}).

The TT-OSL semi-natural DRC is also uniform for the Nilotic quartz. This signal is limited by the low thermal stability of its source trap as was indicated for the Nilotic quartz by combination of field data and laboratory techniques (varying heating rates, isothermal decay, alongside several models). Isothermal decay data exhibits significant departures from first-order kinetic behavior; however, extrapolations of these models imply first-order behavior over geological timescales. The TT-OSL lifetime is assessed at $\sim$550 ka for the eastern Mediterranean Pleistocene climate. Age underestimation simulations demonstrate that the environmental dose rate of the sediment significantly affects the upper limit of the attainable TT-OSL ages. Nevertheless, for a specific storage temperature, TT-OSL age underestimation exceeds 10% after approximately the same time period for virtually all sedimentary environments and dose rates. Thus, TT-OSL ages over 200 ka should be treated with caution as minimum ages.

The pIRIR signal stimulated at 250 °C ($pIRIR_{250}$) was chosen for dating Nilotic feldspar since it displays a preferable balance between bleaching time and recovery ability. The semi-natural DRC of this signal shows some variability in natural saturation for the Nilotic feldspar. Natural saturation is most likely reached at 500 Gy, when equilibrium between electron trap filling and athermal de-trapping is obtained. Nilotic feldspar $pIRIR_{250}$ ages derived from higher equivalent doses are probably minimum ages.

Application of the extended range methods to the Kerem Shalom sediments produces accurate ages up to 200 ka and minimum ages up to 715 ka. The new ages are significantly older than the known luminescence chronology of the coastal sediments in the central and northern parts of Israel which presently are attributed mostly to the last 70 ka. It suggests the presence of sands in the southern coastal plain already in the Early Pleistocene. Even though the early Pleistocene is still out of reach for accurate luminescence dating, middle Pleistocene sediments can be successfully dated with these methods.

A PDF of this thesis can be downloaded from: by contacting the author: galina.faershtein@weizmann.ac.il.

Nicola Horsburgh

REE induced defects in minerals: A Spectroscopic Study

June 2020

School of Earth & Environmental Sciences, University of St Andrews, Scotland, UK

Degree: Ph.D.
Supervisor: Adrian Finch

This thesis examines the luminescence and mineral physics of Rare Earth Element (REE) bearing minerals as a precursor to developing smart sorting tools for critical metals used in low-carbon technologies. I characterise luminescence responses of complex zirconosilicates; eudialyte ($Na_{15}Ca_6(Fe^{2+},Mn^{2+})_3Zr_3[Si_{25}O_{73}](O,OH,H_2O)_3(OH,Cl)_2$), wöhlerite ($NaCa_2(Zr,Nb)(Si_2O_7)(O,OH,F)_2$) and catapleiite ($Na_2Zr(Si_3O_9) \cdot 2H_2O$). Fluorite was included as it is commonly associated with REE ores and displays strong REE luminescence. Its behaviour provides key insights into REE substitution into ionic minerals.

X-ray Excited Optical Luminescence (XEOL) and Thermoluminescence (TL) measurements were taken from 20 to 673 K. Fluorite responses result from a balance of intrinsic luminescence and REE substituents and evidence for REE and defect coupling. Thermoluminescence indicates the presence of electron traps and the coupling of these traps to lanthanide emissions show that the defect and the lanthanide are clustered in physical space. The absence of changes in TL for different lanthanides shows that energy is passed efficiently between rare earths, indicating that the REE are clustered.

The zirconosilicates all show increased intensity in XEOL response below 150 K. Cryogenic emissions are interpreted as originating from the host mineral. There are 3 shared features: UV ($\sim$280 nm) paramagnetic oxygen or oxygen vacancy; blue (440 nm) Al-O^--O /Ti centres; and REE. Wöhlerite and eudialyte show Fe^{3+} band ($\sim$708 nm) and wöhlerite displays broad emission attributed to Mn^{2+}. Eudialyte shows two additional responses; UV ($\sim$320 nm) ten-

tatively assigned to Na migration and UV/blue ($\sim$400 nm) potentially associated with charge balances associated with the coupled substitution of Al^{3+}. Eudialyte shows little emission at room temperature, this is attributed to quenching from Fe^{2+}. Emission from eudialyte above room temperature is attributed to alteration minerals such as catapleiite and potentially to inclusions of luminescent primary mineral phases.

I demonstrate that smart sorting could be a valuable beneficiation tool for REE minerals.

Further information on this thesis can be downloaded from: https://adrianfinchcouk.wordpress.com/2020/06/21/ree-induced-defects-in-minerals-a-spectroscopic-study-phd-thesis-by-nicky-horsburgh/

Jandessa Silva de Jesus

Late Quaternary evolution of the Middle Tocantins River in Eastern Amazon

March 2020

Institute of Geosciences, Universidade de São Paulo, São Paulo, Brazil

Degree: M.Sc.

Supervisors: Fabiano do Nascimento Pupim and André Oliveira Sawakuchi

The Amazon River forms the largest fluvial system on Earth and its dynamics and evolution play a key role in biogeochemistry cycles, ecological services, and biological diversity. The Tocantins River is the largest system that drains the eastern Amazon However, the Quaternary history of the Tocantins River is poorly known due to lack of geomorphological and geochronological data. Therefore, we use geomorphological, sedimentological and optically stimulated luminescence dating (OSL) techniques to the morphosedimentary evolution of the middle reach of the Tocantins river during the Late Quaternary. Three main geomorphological units were mapped: (i) fluvial plain, (ii) fluvial terraces and (iii) paleo-alluvial fan. The OSL ages from 32 samples show ages between 661 $\pm$ 42 years and 160 $\pm$ 16.3 ka. The luminescence properties show bright quartz grains, fast signal decay, exponential growth of dose-response curves and adequate ability to recover doses of radiation. The Single-Aliquot Regenerative (SAR) dose protocol was applied for estimates of the equivalent doses (D_e). Equivalent doses range from 1.6 $\pm$ 0.1 to 166.1 $\pm$ 11.5 Gy. Most of samples shows D_e dispersion below 30%, suggesting a well-bleached sediment not affected by post-deposition mixing; only five samples show relatively high OD values, between 30 and 60%. Dose rates ranged from 0.238 $\pm$ 0.015 to 3.02 $\pm$ 0.238 Gy/ky. Our data indicate three stages of aggradation and two stages of incision. The older aggradational stage is represented by sediments from Upper Terrace (T1) and the Paleo-alluvial fan and occurred between 160 to 32 ka. Subsequently, an incision event occurred at $\sim$31 ka, which resulted in abandonment of T1. The second phase of aggradation is recorded in the Lower Terraces (T2) and promotes a reactivation of the Paleo-alluvial fan from 31 to 6 ka. A new incision occurred about 6 to 5 ka, allowing the abandonment of the T2 and reducing the local base level to its current position. The modern floodplain was built from 5 ka to the present, with sediment deposition due to lateral migration of the Tocantins River. The results presented a highly diversified landscape in terms of geoforms, sedimentary and geochronological aspects that records the geomorphological evolution throughout the Late Quaternary. The geochronology results were correlated with regional paleoclimatic data pointed the climate change as the main drive of the evolution of the Tocantins river in the last 160 ka. The evolution of terraces in this region of the Amazon appears to be synchronous with terraces in Central and Western Amazonia, suggesting that the fluvial systems of the Eastern Amazon, which drain land from Central Brazil, present fluvial responses similar to rivers with headwaters in Andean lands. Reinforces that climatic fluctuations are a key factor in the Quaternary evolution of the Amazon fluvial system.

Şule Kaya-Keleş

Investigation of radiation induced defects of natural quartz: A combined TL, OSL and EPR study

February 2020

Institute of Nuclear Sciences, Ankara University, Ankara, Turkey

Degree: Ph.D.

Supervisors: Prof. Dr. Niyazi Meriç, Dr. George S. Polymeris

Quartz is one of the most preferred mineral inclusions used in retrospective dosimetry. Its crystal structure as well as its impurity content and concentration and the lattice defects exhibit diversities according to its origin. Therefore, it is important to the luminescence properties of natural quartz. In the present work, un-heated, pre-dosed quartz is investigated towards its effective applications such in retrospective dosimetry, dating and as a reference quartz material. The purpose of the study is to find a correlation between Thermoluminescence (TL) (high temperature TL peaks), Optically Stimulated Luminescence (OSL) (both continuous wave (CW) and linear modulation (LM)) and Electron Paramagnetic Resonance (EPR) signals. The present work indicated a triple correlation between the fast CW-OSL component and certain peaks of LM-OSL and TL while all these luminescence entities are attributed to the $C2_{EPR}$ at g_2 (Landé splitting factor) (g_2 = 1.9975). The present study provides experimental evidence that (i) one TL peak might be the source for more than two LM-OSL components and (ii) even two different TL peaks can contribute to the same OSL component. Furthermore, on the EPR signal, besides the well established Ge center, another un-identified component has been resolved.

Xue Rui

A chrono-stratigraphic investigation of lacustrine-fluvial deposits of the Nihewan Basin in the last 0.8 million years

June 2020

School of Earth, Atmospheric and Life Sciences, University of Wollongong, Australia

Degree: Ph.D.

Supervisors: Bo Li, Richard 'Bert' Roberts, Tim Cohen

The Nihewan Basin, northern China, is a key region to study Quaternary paleoenvironmental, paleontological and Paleolithic histories in East Asia. Previous studies showed that this basin was covered by a lake (i.e., the Nihewan Paleolake) during the Early and Middle Pleistocene. This lake was drained by a river (i.e., the Sanggan River) during the late Middle Pleistocene. The lake and river have deposited thick sequences of fluvial-lacustrine deposits, containing rich assemblages of mammalian fossils and stone artefacts. Although many studies have been carried out in this basin for decades, some critical questions remain unanswered, among which three of them form the focus of this thesis: 1) when, how and why did the Nihewan Paleolake disappear; 2) when did the terraces of the Sanggan River form; 3) what is the relationship between human occupation and environmental change in the Nihewan Basin.

Addressing the above questions rely on of the establishment of firm chronological control for the middle and late Quaternary sediments in the basin. So the overarching aim of this thesis is to develop a robust chronological framework for the mid-to-late Pleistocene geomorphological evolution of the basin. A series of newly developed luminescence dating techniques were used to date the sediments associated with lake-level history of the Nihewan Paleolake, human occupation, and the terraces of the Sanggan River. The suitability of luminescence dating on quartz and potassium-rich feldspar (K-feldspar) from this region were investigated; this includes studies of the thermal stability of the optically stimulated luminescence (OSL) signals from quartz, residual and anomalous fading of the post-infrared infrared stimulated luminescence (pIRIR) from K-feldspar, and standardised growth curve of K-feldspar using single aliquots, multiple aliquots and single grains. The performance tests and comparison with independent age controls suggest that quartz OSL is unstable and cannot be used for dating the sediments from this region, whereas K-feldspar pIRIR signals are stable and can provide robust age estimates for samples deposited up to $\sim$780 thousand years ago (ka).

To develop a chronological framework for the history of the Nihewan Basin, sediments from 12 lacustrine sections in the east of the Nihewan Basin were measured by both the single-grain and single-aliquot pIRIR procedure on K-feldspar. Our dating results revealed four periods of high lake levels at 520 – 551, 411 – 430, 298 – 338 and $\sim$168 ka, respectively. Twelve fluvial sections from three Sanggan River terraces (T3, T2 and T1) were identified according to the field investigation, and the single-grain pIRIR dating result for these sediments indicates that the formation ages of three terraces are 124 – 151, 25 – 9 and last 2 ka, respectively. The last high lake level at 168 ka and the oldest fluvial terrace at 151 ka suggests that the Nihewan Paleolake was drained between 151 and 168 ka. Combining the chronology framework with the geomorphological and paleoclimate information in the Nihewan Basin, tectonic movement is most likely the primary factor affecting the demise of the Nihewan Paleolake. By summarizing the published locations of the archaeological sites, we suggest that the hominis settled on the eastern edge of the Nihewan Basin when the paleolake existed. After the demise of the Nihewan Paleolake, they settled near the Sanggan River and spread to the whole basin.

Javier Andrés Sandoval Andrade

Datación de restos humanos prehispánicos a través de esmalte dental usando Resonancia Paramagnética Electronica (EPR) (Dating of Pre-Hispanic human remains through tooth enamel using Electron Paramagnetic Resonance (EPR)

June 1020

Universidad Nacional de Colombia, Bogotá, Colombia

Degree: B.Sc.

Supervisor: Alí Ocal

This thesis presents the experimental procedure followed dating through Electron Paramagnetic Resonance (EPR) pre-Hispanic tooth enamel from the Checua archaeological site (Nemocón, Cundinamarca, Colombia). This work represents a pioneering effort in the development of archaeometry in this country, and in turn is consolidated as the first absolute date determined through EPR in Colombia.

The Checua site has one of the earliest dates in Colombian archaeology (ca. 7800 14C yr BP). Another of my goals in this work was to compare the EPR dates with previous 14C one, testing the technique's efficiency in age assessment for early Colombian sites.

I used two molars from one human skull found at the site between 70 and 80 cm, a stratum related to a semi-permanent hunter-gatherer camp. A mechanical method with liquid cooling was used to separate the enamel from the other dental layers. Then the AIEA protocol for disinfection and treatment of the sample was implemented. Once ready, the enamel was pulverized into grains not exceeding 5 mm and divided into 10 equal parts by weight or aliquots. Each aliquot was irradiated using a Siemens Primus Accelerator (LINAC 3995) at a dose rate of 0.5 Gy / min. The doses supplied were in the range between 0 to 70 Gy. After irradiation, the EPR signal was measured with a Bruker ESP spectrometer in band X. The peak-to-peak height of the signal with perpendicular g was used to calculate the amplitude. After the EPR measurements, the aliquots were irradiated with additional doses and the process was repeated until 10 points of EPR signal were obtained as a function of the dose.

Additionally, sediment samples from the Checua site were collected for measurement of U, Th and K through gamma spectrometry. This process was carried out by the group of nuclear technologies of the Colombian Geological Service. ROSY software was used to calculate the age of the tooth enamel sample. Some parameters such as the cosmic radiation dose ratio of the area (546 μGy / year), the content of U, Th and K obtained from the sediment analysis and the thickness of the dental layers of the sample: enamel (1.4mm) and dentin (5mm) were necessary. The other software defaults were used. Thus, finally, the estimated age in the analyses, for the study sample, was 7850 ± 190 years BP. In this way, the final date obtained through EPR shows an excellent correlation with the previous radiocarbon date, thus motivating the implementation of dating protocols with EPR of tooth enamel to date early archaeological sites in Colombian territory.

A PDF of this thesis can be downloaded from: https://www.researchgate.net/publication/340827271_DATACION_DE_RESTOS_HUMANOS_PREHISPANICOS_A_TRAVES_DE_ESMALTE_DENTAL_USANDO_RESONANCIA_PARAMAGNETICA_ELECTRONICA_EPR

Aayush Srivastava

Late Quaternary dune activity in the Thar Desert and its implications for palaeoenvironmental reconstructions: an insight from optically stimulated luminescence dating

January 2020
University of Oxford, Oxford, UK

Degree: Ph.D.
Supervisors: Julie Durcan, David Thomas

Sand dunes in the Thar Desert, owing to their location in the Indian summer monsoonal (ISM) regime, are rich archives of past geomorphological and palaeoenvironmental changes. However, existing dune records are not robust enough to allow their assessment and integration with a growing multiproxy framework of palaeoenvironmental change. Therefore, with an aim to investigate the timing of dune activity in the Thar, three research questions are answered in this thesis: (i) what are the key phases of dune activity in the desert; (ii) what is the effect of anthropogenic influences on the landscape; and (iii) how can dune chronologies be interpreted most effectively to reconstruct late Quaternary environmental changes? To answer these, systematic sampling of multiple dunes was carried out in the dunefields in the central and northern Thar, and luminescence dating was used to provide a detailed chronological framework.

Results demonstrate that the Thar dunes are >58 ka old, with preserved accumulation phases throughout the Holocene at $\sim 11.6-8.5$, $4-3$, $2-1$, $0.6-0.2$ and 0.07 ka. First records of modern net accumulation are presented, with rates varying between $2-5$ m/year, attributable to anthropogenic disturbances. Dune accumulation intensity methodology, in conjunction with available highly-resolved marine and terrestrial datasets, is used to infer palaeoenvironmental changes in the Thar. Whilst the strengthening of the ISM has been evidently shown to have a significant influence on widespread dune accumulation in the early Holocene, equivocal relationships between both lake levels/dune accumulation and monsoon variability during later Holocene suggest a complex interplay of regional and more local drivers like sediment supply, lowered sea levels etc. The study concludes with emphasis on the importance of recognising external and local controls on dune systems, and demonstrates that diverse responses to same environmental stimuli should be expected in palaeoenvironmental reconstructions.

Roos Marina Johanna van Wees

Combining luminescence dating and sedimentary analysis to derive the landscape dynamics of the Velická Valley in the High Tatra Mountains, Slovakia

June 2020
Lund University, Lund, Sweden

Degree: M.Sc.
Supervisors: Helena Alexanderson, Isa Doverbratt and Juraj Janočko

Luminescence dating is widely used in combination with sedimentological analysis to reconstruct the landscape development of the Quaternary period. Here, quartz and K-feldspar measurements are used to date and evaluate the luminescence characteristics of sediments from seven sites of the lower part of the Velická valley (995 – 1250 m a.s.l.) in the High Tatra Mountains, Slovakia.

The quartz and K-feldspar grains are separated, and multiple quality and control tests are carried out to test the quality of the minerals. The observed characteristics and unreliable results of the quartz are appointed to the weak optical stimulated luminescence signal and the saturation of the signal, this led to using K-feldspar stimulated by infrared stimulated luminescence (IRSL) for further dating of the sampled sediment at the sites. The age of deposition of the sediments is derived from the combined uncorrected and for fading corrected post-IR IRSL at 225 °C (pIRIR225), the corrected ages were applied for the samples containing a fading rate exceeding the 3%/decade. From the sampled and dated modern analogues (samples from next to the river; site 6 and 7) could be inferred that the K-feldspar was significantly incompletely bleached. Moreover, for the four oldest samples the pIRIR225 signal showed to be saturated.

The results of the dating and the sedimentology are put in the context of landscape dynamics. The deposition of the sediments (except for the modern analogues) dates back to the Middle Pleistocene epoch. Sites 4, 1, 2, and 5 (in order from old to young) are correlated to the Riss I and Riss II glaciation and the Riss II/Würm interglacial. From the evidence that the clasts have been reworked by water, the planar beds, and other evidence the sediments on site 1, 2, 4, and 5 are interpreted to have been transported by different kinds of

subaerial flows. Based on the ages and the maximum particle size the ice margin is hypothesized to have been around one kilometre north of the study area during the deposition of the sediment of sites 1 and 2. From this setting and the observations of the sediments, there can be derived that these sediments have been deposited in a proglacial outwash plain. After the deposition of the sediment at site 1 (171 $\pm$ 20 ka) the vertical incision of the Velická valley is believed to have taken place, enhanced by an increase of discharged meltwater from the glacier during a glacial to interglacial transition and the sudden sediment release from the outwash plain generating an erosional pulse. Afterwards, when the input of meltwater decreased and a low energy environment took place, the terraces were deposited (142 $\pm$ 14 ka) in the Velická valley during the Riss II/Würm interglacial.

Bibliography

Compiled by Sebastien Huot

From 1st November 2019 to 31st May 2020

Special issue

- Methods and Applications in Trapped Charge Dating, James K. Feathers ed. Published in Methods and Protocols

Blackwell, A.B.B., Kazi, F.M., Huang, L.C.C., Doronicheva, V.E., Golovanova, V.L., Doronichev, B.V., Singh, K.C.I., Blickstein, I.B.J., 2020. Sedimentary dosimetry for the Saradj-Chuko Grotto: A cave in a Lava Tube in the North-Central Caucasus, Russia. Methods and Protocols 3, 20. http://doi.org/10.3390/mps3010020

Doverbratt, I., Alexanderson, H., 2019. Transferring grains from single-grain luminescence discs to SEM specimen stubs. Methods and Protocols 2, 87. https://www.mdpi.com/2409-9279/2/4/87

Feathers, J.K., 2020. Methods and applications in trapped charge dating. Methods and Protocols 3, 24. http://doi.org/10.3390/mps3010024

Groza-Săcaciu, Ș.-M., Panaiotu, C., Timar-Gabor, A., 2020. Single aliquot regeneration (SAR) optically stimulated luminescence dating protocols using different grain-sizes of quartz: Revisiting the chronology of Mircea Vodă Loess-Paleosol master section (Romania). Methods and Protocols 3, 19. http://doi.org/10.3390/mps3010019

Hood, A.G.E., Highcock, E.G., 2019. Using DosiVox to reconstruct radiation transport through complex archaeological environments. Methods and Protocols 2, 91. https://www.mdpi.com/2409-9279/2/4/91

Hu, Y., Li, B., Jacobs, Z., 2020. Single-grain quartz OSL characteristics: Testing for correlations within and between sites in Asia, Europe And Africa. Methods and Protocols 3, 2. http://doi.org/10.3390/mps3010002

Nelson, M., Rittenour, T., Cornachione, H., 2019. Sampling methods for luminescence dating of subsurface deposits from cores. Methods and Protocols 2, 88. https://www.mdpi.com/2409-9279/2/4/88

Sawakuchi, A.O., Rodrigues, F.C., Mineli, T.D., Mendes, V.R., Melo, D.B., Chiessi, C.M., Giannini, P.C., 2020. Optically stimulated luminescence sensitivity of quartz for provenance analysis. Methods and Protocols 3, 6. http://doi.org/10.3390/mps3010006

Spencer, J.Q.G., Huot, S., Archer, A.W., Caldas, M.M., 2019. Testing luminescence dating methods for small samples from very young fluvial deposits. Methods and Protocols 2, 90. https://www.mdpi.com/2409-9279/2/4/90

Tsukamoto, S., Takeuchi, T., Tani, A., Miyairi, Y., Yokoyama, Y., 2020. ESR and radiocarbon dating of gut strings from early plucked instruments. Methods and Protocols 3, 13. http://doi.org/10.3390/mps3010013

Zhang, J., Li, S.-H., 2020. Review of the Post-IR IRSL dating protocols of K-feldspar. Methods and Protocols 3, 7. http://doi.org/10.3390/mps3010007

Zhang, J.-F., Qiu, W.-L., Hu, G., Zhou, L.-P., 2020. Determining the age of terrace formation using luminescence dating—a case of the Yellow River terraces in the Baode area, China. Methods and Protocols 3, 17. http://doi.org/10.3390/mps3010017

Various geological applications

- aeolian

Buckland, C.E., Bailey, R.M., Thomas, D.S.G., 2019. Using post-IR IRSL and OSL to date young (< 200 yrs) dryland aeolian dune deposits. Radiation Measurements 126, 106131. http://doi.org/10.1016/j.radmeas.2019.106131

Del Valle, L., Pomar, F., Fornós, J.J., Gómez-Pujol, L., Timar-Gabor, A., 2020. Lower to middle pleistocene coastal dune fields formation in the western mediterranean (Western Eivissa, Balearic archipelago): Chronology and landscape evolution. Aeolian Research 45, 100595. http://doi.org/10.1016/j.aeolia.2020.100595

Fitzsimmons, K.E., Nowatzki, M., Dave, A.K., Harder, H., 2020. Intersections between wind regimes, topography and sediment supply: Perspectives from aeolian landforms in Central Asia. Palaeogeography, Palaeoclimatology, Palaeoecology 540, 109531. http://doi.org/10.1016/j.palaeo.2019.109531

Hu, G., Wang, P., Li, D., Huang, J., Wang, H., Yang, X., Zhang, J., Chen, J., Qiu, M., Zhang, A., Shi, L., 2020. Landscape change and its influence on human activities in Lhasa basin of central Tibetan plateau since the last deglacial. Quaternary International 536, 1-12. http://doi.org/10.1016/j.quaint.2019.11.023

Jankowski, N.R., Stern, N., Lachlan, T.J., Jacobs, Z., 2020. A high-resolution late Quaternary depositional history and chronology for the southern portion of the Lake Mungo lunette, semi-arid Australia. Quaternary Science Reviews 233, 106224. http://doi.org/10.1016/j.quascirev.2020.106224

Jin, J.-h., Li, Z.-z., Ling, Z.-y., Zheng, F., Xu, X.-l., Cheng, Y., Cao, X.-d., Li, Z.-x., Zhang, W.-j., Ren, Y.-q., 2019. Chronology of coastal aeolian deposition and its paleoenvironmental implications on the Liuao Peninsula of South China. Journal of Mountain Science 16, 2754-2769. http://doi.org/10.1007/s11629-019-5551-3

Ling, Z., Yang, S., Wang, X., Wang, J., Xia, D., Chen, F., 2020. Spatial-temporal differentiation of eolian sediments in the Yarlung Tsangpo catchment, Tibetan Plateau, and response to global climate change since the Last Glaciation. Geomorphology 357, 107104. http://doi.org/10.1016/j.geomorph.2020.107104

Srivastava, A., Thomas, D.S.G., Durcan, J.A., Bailey, R.M., 2020. Holocene palaeoenvironmental changes in the Thar Desert: An integrated assessment incorporating new insights from aeolian systems. Quaternary Science Reviews 233, 106214. http://doi.org/10.1016/j.quascirev.2020.106214

Wang, X., Zhao, H., Yang, H., Wang, K., 2019. Optical dating reveals that the height of Earth's tallest megadunes in the Badain Jaran Desert of NW China is increasing. Journal of Asian Earth Sciences 185, 104025. http://doi.org/10.1016/j.jseaes.2019.104025

Zular, A., Sawakuchi, A.O., Wang, H., Guedes, C.C.F., Hartmann, G.A., Jaqueto, P.F., Chiessi, C.M., Cruz, F.W., Giannini, P.C.F., Daros, V.K., Atencio, D., Trindade, R.I.F., 2020. The response of a dune succession from Lençóis Maranhenses, NE Brazil, to climate changes between MIS 3 and MIS 2. Quaternary International 537, 97-111. http://doi.org/10.1016/j.quaint.2019.12.012

- cave

Watanabe, S., Cano, N.F., Carvalho-Júnior, A.B., Ayala-Arenas, J.S., Gonzales-Lorenzo, C.D., Rao, T.K.G., 2019. Dating of carbonate covering cave paintings at peruaçu, Brazil by TL and EPR methods. Applied Radiation and Isotopes 153, 108847. http://doi.org/10.1016/j.apradiso.2019.108847

- coastal

Bartz, M., Walk, J., Binnie, S.A., Brill, D., Stauch, G., Lehmkuhl, F., Hoffmeister, D., Brückner, H., 2020. Late Pleistocene alluvial fan evolution along the coastal Atacama Desert (N Chile). Global and Planetary Change 190, 103091. http://doi.org/10.1016/j.gloplacha.2019.103091

Brill, D., Cisternas, M., 2020. Testing quartz and feldspar luminescence dating to determine earthquake and tsunami recurrence in the area of the giant 1960 Chile earthquake. Quaternary Geochronology 58, 101080. http://doi.org/10.1016/j.quageo.2020.101080

Brill, D., Seeger, K., Pint, A., Reize, F., Hlaing, K.T., Seeliger, M., Opitz, S., Win, K.M.M., Nyunt, W.T., Aye, N., Aung, A., Kyaw, K., Kraas, F., Brückner, H., 2020. Modern and historical tropical cyclone and tsunami deposits at the coast of Myanmar: Implications for their identification and preservation in the geological record. Sedimentology 67, 1431-1459. http://doi.org/10.1111/sed.12586

Cano, N.F., Ayala-Arenas, J.S., Javier-Ccallata, H.S., Watanabe, S., 2020. OSL and EPR dating of shells and sediments from Congonhas II sambaqui, Santa Catarina, Brazil. Radiation Physics and Chemistry 167, 108240. http://doi.org/10.1016/j.radphyschem.2019.03.044

Chamberlain, E.L., Mehta, J.M., Reimann, T., Wallinga, J., 2020. A geoarchaeological perspective on the challenges and trajectories of Mississippi Delta communities. Geomorphology 360, 107132. http://doi.org/10.1016/j.geomorph.2020.107132

Cheng, Q., Wang, F., Chen, J., Ge, C., Chen, Y., Zhao, X., Nian, X., Zhang, W., Liu, K.-b., Xu, Y., Lam, N., 2020. Combined chronological and mineral magnetic approaches to reveal age variations and stratigraphic heterogeneity in the Yangtze River subaqueous delta. Geomorphology 359, 107163. http://doi.org/10.1016/j.geomorph.2020.107163

Dalabehera, L., Hazra, A., Pattanayak, S., Pal, T., 2020. The paleobeach ridges of Digha coastal tract, West Bengal, India: Observation and implication for sea regression from 500 YBP to 200 YBP. Journal of the Geological Society of India 95, 131-144. http://doi.org/10.1007/s12594-020-1402-7

Dillenburg, S.R., Hesp, P.A., Keane, R., da Silva, G.M., Sawakuchi, A.O., Moffat, I., Barboza, E.G., Bitencourt, V.J.B., 2020. Geochronology and evolution of a complex barrier, Younghusband Peninsula, South Australia. Geomorphology 354, 107044. http://doi.org/10.1016/j.geomorph.2020.107044

Ellerton, D., Rittenour, T., Shulmeister, J., Gontz, A., Welsh, K.J., Patton, N., 2020. An 800 kyr record of dune emplacement in relationship to high sea level forcing, Cooloola Sand Mass, Queensland, Australia. Geomorphology 354, 106999. http://doi.org/10.1016/j.geomorph.2019.106999

Fruergaard, M., Tessier, B., Poirier, C., Mouazé, D., Weill, P., Noël, S., 2020. Depositional controls on a hypertidal barrier-spit system architecture and evolution, Pointe du Banc spit, north-western France. Sedimentology 67, 502-533. http://doi.org/10.1111/sed.12652

Goswami, K., Krishnan, S., Kumerasan, A., Sadasivam, S.K., Kumar, P., Jaiswal, M.K., 2019. Luminescence chronology of fluvial and marine records from subsurface core in Kaveri delta, Tamil Nadu: Implications to sea level fluctuations. Geochronometria 46, 125-137. http://doi.org/10.1515/geochr-2015-0112

Guedes, C.C.F., Nascimento, M.G.d., Angulo, R.J., Souza, M.C.d., 2020. Geological evidences as a guide to OSL dating interpretation and northern occurrence of MIS 7e barrier at Southern Brazil. Journal of South American Earth Sciences 98, 102478. http://doi.org/10.1016/j.jsames.2019.102478

Hoffmann, G., Grützner, C., Schneider, B., Preusser, F., Reicherter, K., 2020. Large Holocene tsunamis in the northern Arabian Sea. Marine Geology 419, 106068. http://doi.org/10.1016/j.margeo.2019.106068

Jin, J.-h., Li, Z.-z., Ling, Z.-y., Zheng, F., Xu, X.-l., Cheng, Y., Cao, X.-d., Li, Z.-x., Zhang, W.-j., Ren, Y.-q., 2019. Chronology of coastal aeolian deposition and its paleoenvironmental implications on the Liuao Peninsula of South China. Journal of Mountain Science 16, 2754-2769. http://doi.org/10.1007/s11629-019-5551-3

Lewis, R.J., Tibby, J., Arnold, L.J., Barr, C., Marshall, J., McGregor, G., Gadd, P., Yokoyama, Y., 2020. Insights into subtropical Australian aridity from Welsby Lagoon, north Stradbroke Island, over the past 80,000 years. Quaternary Science Reviews 234, 106262. http://doi.org/10.1016/j.quascirev.2020.106262

Li, Y., Tsukamoto, S., Shang, Z., Tamura, T., Wang, H., Frechen, M., 2019. Constraining the transgression history in the Bohai Coast China since the Middle Pleistocene by luminescence dating. Marine Geology 416, 105980. http://doi.org/10.1016/j.margeo.2019.105980

Liu, J., Qiu, J., Saito, Y., Zhang, X., Nian, X., Wang, F., Xu, G., Xu, T., Li, M., 2020. Formation of the Yangtze Shoal in response to the post-glacial transgression of the paleo-Yangtze (Changjiang) estuary, China. Marine Geology 423, 106080. http://doi.org/10.1016/j.margeo.2019.106080

Oliver, T.S.N., Murray-Wallace, C.V., Woodroffe, C.D., 2020. Holocene shoreline progradation and coastal evolution at Guichen and Rivoli Bays, southern Australia. The Holocene 30, 106-124. http://doi.org/10.1177/0959683619875815

Zhou, L., Gao, S., Jia, J., Zhang, Y., Yang, Y., Mao, L., Fang, X., Shulmeister, J., 2019. Extracting historic cyclone data from coastal dune deposits in eastern Hainan Island, China. Sedimentary Geology 392, 105524. http://doi.org/10.1016/j.sedgeo.2019.105524

- colluvial

May, S.M., Meine, L., Hoffmeister, D., Brill, D., Medialdea, A., Wennrich, V., Gröbner, M., Schulte, P., Steininger, F., Deprez, M., de Kock, T., Bubenzer, O., 2020. Origin and timing of past hillslope activity in the hyper-arid core of the Atacama Desert – The formation of fine sediment lobes along the Chuculay Fault System, Northern Chile. Global and Planetary Change 184, 103057. http://doi.org/10.1016/j.gloplacha.2019.103057

Medialdea, A., May, S.M., Brill, D., King, G., Ritter, B., Wennrich, V., Bartz, M., Zander, A., Kuiper, K., Hurtado, S., Hoffmeister, D., Schulte, P., Gröbner, M., Opitz, S., Brückner, H., Bubenzer, O., 2020. Identification of humid periods in the Atacama Desert through hillslope activity established by infrared stimulated luminescence (IRSL) dating. Global and Planetary Change 185, 103086. http://doi.org/10.1016/j.gloplacha.2019.103086

- earthquake (and fault related)

Bacon, S.N., Bullard, T.F., Keen-Zebert, A.K., Jayko, A.S., Decker, D.L., 2020. Spatiotemporal patterns of distributed slip in southern Owens Valley indicated by deformation of late Pleistocene shorelines, eastern California. GSA Bulletin 132, 1681-1703. http://doi.org/10.1130/B35247.1

Burgette, R.J., Hanson, A.M., Scharer, K.M., Rittenour, T.M., McPhillips, D., 2020. Late Quaternary slip rate of the Central Sierra Madre fault, southern California: Implications for slip partitioning and earthquake hazard. Earth and Planetary Science Letters 530, 115907. http://doi.org/10.1016/j.epsl.2019.115907

Cocco, F., Andreucci, S., Sechi, D., Cossu, G., Funedda, A., 2019. Upper Pleistocene tectonics in western Sardinia (Italy): Insights from the Sinis peninsula structural high. Terra Nova 31, 485-493. http://doi.org/10.1111/ter.12418

Fattahi, M., Talebian, M., Khatib, M.M., Aghazadeh, A., Amini, H., Ataei, N., Sloan, R.A., Ersek, V., 2019. Slip rate determination of Dasht-e Bayaz fault using single grain OSL dating of Miam Qanat system in eastern Iran. Journal of Seismology and Earthquake Engineering 21, 1-9. http://www.jsee.ir/index.php/jsee/article/view/652

Guo, X., Wei, J., Song, Z., Lai, Z., Yu, L., 2020. Optically stimulated luminescence chronology and geomorphic imprint of Xiazangtan landslide upon the upper Yellow River valley on the northeastern Tibetan Plateau. Geological Journal 55, 5498-5507. http://doi.org/10.1002/gj.3754

Gutiérrez, F., Moreno, D., López, G.I., Jiménez, F., del Val, M., Alonso, M.J., Martínez-Pillado, V., Guzmán, O., Martínez, D., Carbonel, D., 2020. Revisiting the slip rate of Quaternary faults in the Iberian Chain, NE Spain. Geomorphic and seismic-hazard implications. Geomorphology 363, 107233. http://doi.org/10.1016/j.geomorph.2020.107233

Li, X., Zhang, H., Su, Q., 2019. Bedrock channel form in the Madong Shan (NE Tibet): Implications for the strain transfer along the strike-slip Haiyuan Fault. Journal of Asian Earth Sciences 181, 103896. http://doi.org/10.1016/j.jseaes.2019.103896

Lin, S., Li, Y., Luo, D., Fu, Y., 2019. Research on the fracture structure and activity of the Qinling Mountains thrust nappe system in western Hubei. Canadian Journal of Earth Sciences 57, 1-15. http://doi.org/10.1139/cjes-2018-0118

McCalpin, J.P., Gutierrez, F., Bruhn, R.L., Guerrero, J., Pavlis, T.L., Lucha, P., 2020. Tectonic geomorphology and late Quaternary deformation on the Ragged Mountain fault, Yakutat microplate, south coastal Alaska. Geomorphology 351, 106875. http://doi.org/10.1016/j.geomorph.2019.106875

- fluvial

An, P., Yu, L., Wang, Y., Miao, X., Wang, C., Lai, Z., Shen, H., 2020. Holocene incisions and flood activities of the Keriya River, NW margin of the Tibetan plateau. Journal of Asian Earth Sciences 191, 104224. http://doi.org/10.1016/j.jseaes.2019.104224

Cunha, P.P., Martins, A.A., Gomes, A., Stokes, M., Cabral, J., Lopes, F.C., Pereira, D., de Vicente, G., Buylaert, J.-P., Murray, A.S., Antón, L., 2019. Mechanisms and age estimates of continental-scale endorheic to exorheic drainage transition: Douro River, Western Iberia. Global and Planetary Change 181, 102985. http://doi.org/10.1016/j.gloplacha.2019.102985

Forbes, M., Jankowski, N., Cohen, T., Hopf, F., Mueller, D., Bird, M., Haberle, S., Jacobs, Z., 2020. Palaeochannels of Australia's Riverine Plain - Reconstructing past vegetation environments across the Late Pleistocene and Holocene. Palaeogeography, Palaeoclimatology, Palaeoecology 545, 109533. http://doi.org/10.1016/j.palaeo.2019.109533

Greenbaum, N., Mushkin, A., Porat, N., Amit, R., 2020. Runoff generation, rill erosion and time-scales for hyper-arid abandoned alluvial surfaces, the Negev desert, Israel. Geomorphology 358, 107101. http://doi.org/10.1016/j.geomorph.2020.107101

Hu, G., Wang, P., Li, D., Huang, J., Wang, H., Yang, X., Zhang, J., Chen, J., Qiu, M., Zhang, A., Shi, L., 2020. Landscape change and its influence on human activities in Lhasa basin of central Tibetan plateau since the last deglacial. Quaternary International 536, 1-12. http://doi.org/10.1016/j.quaint.2019.11.023

Lauer, T., Weiss, M., Bernhardt, W., Heinrich, S., Rappsilber, I., Stahlschmidt, M.C., von Suchodoletz, H., Wansa, S., 2020. The Middle Pleistocene fluvial sequence at Uichteritz, central Germany: Chronological framework, paleoenvironmental history and early human presence during MIS 11. Geomorphology 354, 107016. http://doi.org/10.1016/j.geomorph.2019.107016

Li, X., Zhang, H., Su, Q., 2019. Bedrock channel form in the Madong Shan (NE Tibet): Implications for the strain transfer along the strike-slip Haiyuan Fault. Journal of Asian Earth Sciences 181, 103896. http://doi.org/10.1016/j.jseaes.2019.103896

Lopes, F.A., Lana, C.E., Castro, P.d.T.A., de Carvalho Lana, C., 2020. Paleomorphology of the northwestern of the Quadrilátero Ferrífero (central Brazil): Stratigraphic and geochronological evidence of a pleistocene alluvial fan system. Quaternary International 542, 30-40. http://doi.org/10.1016/j.quaint.2020.02.025

Ma, Z., Feng, Z., Peng, T., Liu, S., Li, M., Guo, B., Li, X., Song, C., Zhao, Z., Li, J., 2020. Quaternary drainage evolution of the Datong River, Qilian Mountains, northeastern Tibetan Plateau, China. Geomorphology 353, 107021. http://doi.org/10.1016/j.geomorph.2019.107021

Moiya, J.N., Luirei, K., Longkumer, L., Kothyari, G.C., Thong, G.T., 2020. Late Quaternary deformation in parts of the Belt of Schuppen of Dimapur and Peren districts, Nagaland, NE India. Geological Journal 55, 457-476. http://doi.org/10.1002/gj.3413

Neagu, N., Matmon, A., Enzel, Y., Porat, N., 2020. Quaternary evolution of a hyperarid drainage under climatic fluctuations and rift-margin base-level fall, NE Negev, Israel. Geomorphology 354, 107042. http://doi.org/10.1016/j.geomorph.2020.107042

Oldknow, C.J., Carr, A.S., Hooke, J.M., Shen, Z., 2020. The suitability of a low temperature post-IR IRSL signal for dating alluvial and colluvial "cut and fill" sequences in the Great Karoo, South Africa. Quaternary Geochronology 58, 101064. http://doi.org/10.1016/j.quageo.2020.101064

Spencer, J.Q.G., Huot, S., Archer, A.W., Caldas, M.M., 2019. Testing luminescence dating methods for small samples from very young fluvial deposits. Methods and Protocols 2, 90. https://www.mdpi.com/2409-9279/2/4/90

Suresh, N., Kumar, R., 2020. Late Quaternary Deflections of the Beas-Satluj rivers at the Himalayan mountain front, Kangra re-entrant, India: Response to fold growth and climate. Journal of Asian Earth Sciences 191, 104248. http://doi.org/10.1016/j.jseaes.2020.104248

Williams, R.T., Fryirs, K.A., 2020. The morphology and geomorphic evolution of a large chain-of-ponds river system. Earth Surface Processes and Landforms 45, 1732-1748. http://doi.org/10.1002/esp.4842

Zhang, J.-F., Qiu, W.-L., Hu, G., Zhou, L.-P., 2020. Determining the age of terrace formation using luminescence dating—a case of the Yellow River terraces in the Baode area, China. Methods and Protocols 3, 17. http://doi.org/10.3390/mps3010017

- glacial and periglacial

Meyer, M.C., Gliganic, L.A., May, J.H., Merchel, S., Rugel, G., Schlütz, F., Aldenderfer, M.S., Krainer, K., 2020. Landscape dynamics and human-environment interactions in the northern foothills of Cho Oyu and Mount Everest (southern Tibet) during the Late Pleistocene and Holocene. Quaternary Science Reviews 229, 106127. http://doi.org/10.1016/j.quascirev.2019.106127

Shukla, A.D., Sharma, S., Rana, N., Bisht, P., Juyal, N., 2020. Optical chronology and climatic implication of glacial advances from the southern Ladakh Range, NW Himalaya, India. Palaeogeography, Palaeoclimatology, Palaeoecology 539, 109505. http://doi.org/10.1016/j.palaeo.2019.109505

- karst

Engel, M., Rückmann, S., Drechsler, P., Brill, D., Opitz, S., Fassbinder, J.W., Pint, A., Peis, K., Wolf, D., Gerber, C., Pfeiffer, K., Eichmann, R., Brückner, H., 2020. Sediment-filled karst depressions and riyad – key archaeological environments of south Qatar. Quaternary Science Journal 68, 215-236. http://doi.org/10.5194/egqsj-68-215-2020

- lacustrine

Bacon, S.N., Bullard, T.F., Keen-Zebert, A.K., Jayko, A.S., Decker, D.L., 2020. Spatiotemporal patterns of distributed slip in southern Owens Valley indicated by deformation of late Pleistocene shorelines, eastern California. GSA Bulletin 132, 1681-1703. http://doi.org/10.1130/B35247.1

Bacon, S.N., Jayko, A.S., Owen, L.A., Lindvall, S.C., Rhodes, E.J., Schumer, R.A., Decker, D.L., 2020. A 50,000-year record of lake-level variations and overflow from Owens Lake, eastern California, USA. Quaternary Science Reviews 238, 106312. http://doi.org/10.1016/j.quascirev.2020.106312

Barrows, T.T., Fitzsimmons, K.E., Mills, S.C., Tumney, J., Pappin, D., Stern, N., 2020. Late Pleistocene lake level history of Lake Mungo, Australia. Quaternary Science Reviews 238, 106338. http://doi.org/10.1016/j.quascirev.2020.106338

Diederich, J.L., Wennrich, V., Bao, R., Büttner, C., Bolten, A., Brill, D., Buske, S., Campos, E., Fernández-Galego, E., Gödickmeier, P., Ninnemann, L., Reyers, M., Ritter, B., Ritterbach, L., Rolf, C., Scheidt, S., Dunai, T.J., Melles, M., 2020. A 68 ka precipitation record from the hyperarid core of the Atacama Desert in northern Chile. Global and Planetary Change 184, 103054. http://doi.org/10.1016/j.gloplacha.2019.103054

Jiang, M., Han, Z., Li, X., Wang, Y., Stevens, T., Cheng, J., Lv, C., Zhou, Y., Yang, Q., Xu, Z., Yi, S., Lu, H., 2020. Beach ridges of Dali Lake in Inner Mongolia reveal precipitation variation during the Holocene. Journal of Quaternary Science 35, 716-725. http://doi.org/10.1002/jqs.3195

Kemp, C.W., Tibby, J., Arnold, L.J., Barr, C., Gadd, P.S., Marshall, J.C., McGregor, G.B., Jacobsen, G.E., 2020. Climates of the last three interglacials in subtropical eastern Australia inferred from wetland sediment geochemistry. Palaeogeography, Palaeoclimatology, Palaeoecology 538, 109463. http://doi.org/10.1016/j.palaeo.2019.109463

Li, G., Wang, Z., Zhao, W., Jin, M., Wang, X., Tao, S., Chen, C., Cao, X., Zhang, Y., Yang, H., Madsen, D., 2020. Quantitative precipitation reconstructions from Chagan Nur revealed lag response of East Asian summer monsoon precipitation to summer insolation during the Holocene in arid northern China. Quaternary Science Reviews 239, 106365. http://doi.org/10.1016/j.quascirev.2020.106365

Ling, Z., Yang, S., Wang, X., Wang, J., Xia, D., Chen, F., 2020. Spatial-temporal differentiation of eolian sediments in the Yarlung Tsangpo catchment, Tibetan Plateau, and response to global climate change since the Last Glaciation. Geomorphology 357, 107104. http://doi.org/10.1016/j.geomorph.2020.107104

Simon, Q., Ledru, M.-P., Sawakuchi, A.O., Favier, C., Mineli, T.D., Grohmann, C.H., Guedes, M., Bard, E., Thouveny, N., Garcia, M., Tachikawa, K., Rodríguez-Zorro, P.A., 2020. Chronostratigraphy of a 1.5±0.1 Ma composite sedimentary record from Colônia basin (SE Brazil): Bayesian modeling based on paleomagnetic, authigenic 10Be/9Be, radiocarbon and luminescence dating. Quaternary Geochronology 58, 101081. http://doi.org/10.1016/j.quageo.2020.101081

Sobczyk, A., Borówka, R.K., Badura, J., Stachowicz-Rybka, R., Tomkowiak, J., Hrynowiecka, A., Sławińska, J., Tomczak, M., Pitura, M., Lamentowicz, M., Kołaczek, P., Karpińska-Kołaczek, M., Tarnawski, D., Kadej, M., Moska, P., Krąpiec, M., Stachowicz, K., Bieniek, B., Siedlik, K., Bąk, M., van der Made, J., Kotowski, A., Stefaniak, K., 2020. Geology, stratigraphy and palaeoenvironmental evolution of the Stephanorhinus kirchbergensis-bearing Quaternary palaeolake(s) of Gorzów Wielkopolski (NW Poland, Central Europe). Journal of Quaternary Science 35, 539-558. http://doi.org/10.1002/jqs.3198

Wu, D., Zhou, A., Zhang, J., Chen, J., Li, G., Wang, Q., Chen, L., Madsen, D., Abbott, M., Cheng, B., Chen, F., 2020. Temperature-induced dry climate in basins in the northeastern Tibetan Plateau during the early to middle Holocene. Quaternary Science Reviews 237, 106311. http://doi.org/10.1016/j.quascirev.2020.106311

- loess

Balescu, S., Tuffreau, A., Dobrescu, R., Auguste, P., Bahain, J.-J., Lamothe, M., Petculescu, A., Shao, Q., 2018. Nouvelles données sur la chronologie des sites paléolithiques en contexte lœssique du Nord-Est et du Sud-Est de la Roumanie (Périphérie orientale des Carpates). L'Anthropologie 122, 87-110. http://doi.org/10.1016/j.anthro.2018.02.001

Carobene, D., Meyer, M.C., Spötl, C., Rötzel, R., Göhlich, U.B., Mandic, O., Harzhauser, M., Wimmer-Frey, I., Reimer, P.J., Auer, F., 2020. An interdisciplinary study of a mammoth-bearing Late Pleistocene sediment succession in lower Austria. Quaternary International 542, 15-29. http://doi.org/10.1016/j.quaint.2020.02.022

Fenn, K., Durcan, J.A., Thomas, D.S.G., Banak, A., 2020. A 180 ka record of environmental change at Erdut (Croatia): a new chronology for the loess–palaeosol sequence and its implications for environmental interpretation. Journal of Quaternary Science 35, 582-593. http://doi.org/10.1002/jqs.3201

Groza-Săcaciu, Ș.-M., Panaiotu, C., Timar-Gabor, A., 2020. Single aliquot regeneration (SAR) optically stimulated luminescence dating protocols using different grain-sizes of quartz: Revisiting the chronology of Mircea Vodă Loess-Paleosol master section (Romania). Methods and Protocols 3, 19. http://doi.org/10.3390/mps3010019

Li, G., Yang, H., Stevens, T., Zhang, X., Zhang, H., Wei, H., Zheng, W., Li, L., Liu, X., Chen, J., Xia, D., Oldknow, C., Ye, W., Chen, F., 2020. Differential ice volume and orbital modulation of Quaternary moisture patterns between Central and East Asia. Earth and Planetary Science Letters 530, 115901. http://doi.org/10.1016/j.epsl.2019.115901

Li, G., Zhang, H., Liu, X., Yang, H., Wang, X., Zhang, X., Jonell, T.N., Zhang, Y., Huang, X., Wang, Z., Yixuan, W., Yu, L., Xia, D., 2020. Paleoclimatic changes and modulation of East Asian summer monsoon by high-latitude forcing over the last 130,000 years as revealed by independently dated loess-paleosol sequences on the NE Tibetan Plateau. Quaternary Science Reviews 237, 106283. http://doi.org/10.1016/j.quascirev.2020.106283

Lu, H., Wu, D., Zhang, H., Ma, Y., Zheng, X., Li, Y., 2020. Spatial patterns of Late Quaternary river incision along the northern Tian Shan foreland. Geomorphology 357, 107100. http://doi.org/10.1016/j.geomorph.2020.107100

Sun, H., Song, Y., Chen, X., Cheng, L., Liu, H., 2020. Holocene dust deposition in the Ili Basin and its implications for climate variations in Westerlies-dominated Central Asia. Palaeogeography, Palaeoclimatology, Palaeoecology 550, 109731. http://doi.org/10.1016/j.palaeo.2020.109731

Tecsa, V., Gerasimenko, N., Veres, D., Hambach, U., Lehmkuhl, F., Schulte, P., Timar-Gabor, A., 2020. Revisiting the chronostratigraphy of Late Pleistocene loess-paleosol sequences in southwestern Ukraine: OSL dating of Kurortne section. Quaternary International 542, 65-79. http://doi.org/10.1016/j.quaint.2020.03.001

Tecsa, V., Mason, J.A., Johnson, W.C., Miao, X., Constantin, D., Radu, S., Magdas, D.A., Veres, D., Marković, S.B., Timar-Gabor, A., 2020. Latest Pleistocene to Holocene loess in the central Great Plains: Optically stimulated luminescence dating and multi-proxy analysis of the enders loess section (Nebraska, USA). Quaternary Science Reviews 229, 106130. http://doi.org/10.1016/j.quascirev.2019.106130

Waroszewski, J., Sprafke, T., Kabala, C., Musztyfaga, E., Kot, A., Tsukamoto, S., Frechen, M., 2020. Chronostratigraphy of silt-dominated Pleistocene periglacial slope deposits on Mt. Ślęża (SW, Poland): Palaeoenvironmental and pedogenic significance. CATENA 190, 104549. http://doi.org/10.1016/j.catena.2020.104549

Xu, S., Kong, F., Jia, G., Miao, X., Ding, X., 2018. An integrated OSL chronology, sedimentology and geochemical approach to loess deposits from Tuoji Island, Shandong Province: Implications for the late quaternary paleoenvironment in East China. Aeolian Research 31, 105-116. http://doi.org/10.1016/j.aeolia.2017.07.007

Zhang, J., Zhou, X., Long, H., 2020. Late Quaternary loess accumulation at the Rudak section in Uzbekistan, central Asia: Chronology and palaeoclimate implications. Palaeogeography, Palaeoclimatology, Palaeoecology 547, 109695. http://doi.org/10.1016/j.palaeo.2020.109695

Zhang, J.-F., Qiu, W.-L., Hu, G., Zhou, L.-P., 2020. Determining the age of terrace formation using luminescence dating—a case of the Yellow River terraces in the Baode area, China. Methods and Protocols 3, 17. http://doi.org/10.3390/mps3010017

- soil

Bourman, R.P., Buckman, S., Chivas, A.R., Ollier, C.D., Price, D.M., 2020. Ferricretes at Burringurrah (Mount Augustus), Western Australia: Proof of lateral derivation. Geomorphology 354, 107017. http://doi.org/10.1016/j.geomorph.2019.107017

Pollmann, T., Tsukamoto, S., Frechen, M., Giani, L., 2020. Rate of soil formation in Arenosols of dunes on Spiekeroog Island (Germany). Geoderma Regional 20, e00246. http://doi.org/10.1016/j.geodrs.2019.e00246

- surface exposure dating

Riedesel, S., Autzen, M., 2020. Beta and gamma dose rate attenuation in rocks and sediment. Radiation Measurements 133, 106295. http://doi.org/10.1016/j.radmeas.2020.106295

- tephra (and volcanic related)

Bösken, J.J., Schmidt, C., 2020. Direct and indirect luminescence dating of tephra: A review. Journal of Quaternary Science 35, 39-53. http://doi.org/10.1002/jqs.3160

Harangi, S., Molnár, K., Schmitt, A.K., Dunkl, I., Seghedi, I., Novothny, Á., Molnár, M., Kiss, B., Ntaflos, T., Mason, P.R.D., Lukács, R., 2020. Fingerprinting the Late Pleistocene tephras of Ciomadul volcano, eastern–central Europe. Journal of Quaternary Science 35, 232-244. http://doi.org/10.1002/jqs.3177

Reuther, J.D., Rogers, J., Druckenmiller, P., Bundtzen, T.K., Wallace, K., Bowman, R., May, K., Feathers, J., Cherkinsky, A., 2020. Late Quaternary (≥MIS 3 to MIS 1) stratigraphic transitions in a highland Beringian landscape along the Kuskokwim River, Alaska. Quaternary Research 93, 139-154. http://doi.org/10.1017/qua.2019.51

Shitaoka, Y., Saito, T., Yamamoto, J., Miyoshi, M., Ishibashi, H., Soda, T., 2019. Eruption age of Kannabe volcano using multi-dating: Implications for age determination of young basaltic lava flow. Geochronometria 46, 49-56. http://doi.org/10.1515/geochr-2015-0108

Zámolyi, A., Salcher, B., Draganits, E., Exner, U., Wagreich, M., Gier, S., Fiebig, M., Lomax, J., Surányi, G., Diel, M., Zámolyi, F., 2017. Latest Pannonian and Quaternary evolution at the transition between Eastern Alps and Pannonian Basin: new insights from geophysical, sedimentological and geochronological data. International Journal of Earth Sciences 106, 1695-1721. http://doi.org/10.1007/s00531-016-1383-3

Archaeology applications

al Khasawneh, S., Murray, A., Kafafi, Z., Petit, L., 2019. Luminescence dating of the Iron Age deposits from Tell Damiyah in the Jordan Valley. Radiocarbon 62, 1-12. http://doi.org/10.1017/RDC.2019.90

Blackwell, A.B.B., Kazi, F.M., Huang, L.C.C., Doronicheva, V.E., Golovanova, V.L., Doronichev, B.V., Singh, K.C.I., Blickstein, I.B.J., 2020. Sedimentary dosimetry for the Saradj-Chuko Grotto: A cave in a Lava Tube in the North-Central Caucasus, Russia. Methods and Protocols 3, 20. http://doi.org/10.3390/mps3010020

Blackwell, B.A.B., Šalamanov-Korobar, L., Huang, C.L.C., Zhuo, J.L., Kitanovski, B., Blickstein, J.I.B., Florentin, J.A., Vasilevski, S., 2019. Sedimentary radioactivity in an upper paleolithic-middle paleolithic (MP-UP) transition site: Increasing ESR tooth dating accuracy at Golema Pešt, North Macedonia. Radiation Protection Dosimetry 186, 94-112. http://doi.org/10.1093/rpd/ncz183

Chamberlain, E.L., Mehta, J.M., Reimann, T., Wallinga, J., 2020. A geoarchaeological perspective on the challenges and trajectories of Mississippi Delta communities. Geomorphology 360, 107132. http://doi.org/10.1016/j.geomorph.2020.107132

Clarkson, C., Harris, C., Li, B., Neudorf, C.M., Roberts, R.G., Lane, C., Norman, K., Pal, J., Jones, S., Shipton, C., Koshy, J., Gupta, M.C., Mishra, D.P., Dubey, A.K., Boivin, N., Petraglia, M., 2020. Human occupation of northern India spans the Toba super-eruption ~74,000 years ago. Nature Communications 11, 961. http://doi.org/10.1038/s41467-020-14668-4

Daujeard, C., Falguères, C., Shao, Q., Geraads, D., Hublin, J.-J., Lefèvre, D., Graoui, M.E., Rué, M., Gallotti, R., Delvigne, V., Queffelec, A., Arous, E.B., Tombret, O., Mohib, A., Raynal, J.-P., 2020. Earliest African evidence of carcass processing and consumption in cave at 700 ka, Casablanca, Morocco. Scientific Reports 10, 4761. http://doi.org/10.1038/s41598-020-61580-4

Dirks, P.H.G.M., Roberts, E.M., Hilbert-Wolf, H., Kramers, J.D., Hawks, J., Dosseto, A., Duval, M., Elliott, M., Evans, M., Grün, R., Hellstrom, J., Herries, A.I.R., Joannes-Boyau, R., Makhubela, T.V., Placzek, C.J., Robbins, J., Spandler, C., Wiersma, J., Woodhead, J., Berger, L.R., 2017. The age of Homo naledi and associated sediments in the Rising Star Cave, South Africa. eLife 6, e24231. http://doi.org/10.7554/eLife.24231

Feathers, J.K., Evans, M., Stratford, D.J., de la Peña, P., 2020. Exploring complexity in luminescence dating of quartz and feldspars at the Middle Stone Age site of Mwulu's cave (Limpopo, South Africa). Quaternary Geochronology 59, 101092. http://doi.org/10.1016/j.quageo.2020.101092

Feathers, J.K., Nami, H.G., 2018. Luminescence dating of Late Pleistocene and Holocene sediments in Uruguay. Latin American Antiquity 29, 495-513. http://doi.org/10.1017/laq.2018.9

Gao, J., Hou, G., Wei, H., Chen, Y., E, C., Chen, X., Lancuo, Z., 2020. Prehistoric human activity and its environmental background in Lake Donggi Cona basin, northeastern Tibetan Plateau. The Holocene 30, 657-671. http://doi.org/10.1177/0959683619895583

Glauberman, P., Gasparyan, B., Sherriff, J., Wilkinson, K., Li, B., Knul, M., Brittingham, A., Hren, M.T., Arakelyan, D., Nahapetyan, S., Raczynski-Henk, Y., Haydosyan, H., Adler, D.S., 2020. Barozh 12: Formation processes of a late Middle Paleolithic open-air site in western Armenia. Quaternary Science Reviews 236, 106276. http://doi.org/10.1016/j.quascirev.2020.106276

Goder-Goldberger, M., Crouvi, O., Caracuta, V., Kolska Horwitz, L., Neumann, F.H., Porat, N., Scott, L., Shavit, R., Jacoby-Glass, Y., Zilberman, T., Boaretto, E., 2020. The Middle to Upper Paleolithic transition in the southern Levant: New insights from the late Middle Paleolithic site of Far'ah II, Israel. Quaternary Science Reviews 237, 106304. http://doi.org/10.1016/j.quascirev.2020.106304

Heydari, M., Guérin, G., Kreutzer, S., Jamet, G., Kharazian, M.A., Hashemi, M., Nasab, H.V., Berillon, G., 2020. Do Bayesian methods lead to more precise chronologies? 'BayLum' and a first OSL-based chronology for the Palaeolithic open-air site of Mirak (Iran). Quaternary Geochronology 59, 101082. http://doi.org/10.1016/j.quageo.2020.101082

Hood, A.G.E., Highcock, E.G., 2019. Using DosiVox to reconstruct radiation transport through complex archaeological environments. Methods and Protocols 2, 91. https://www.mdpi.com/2409-9279/2/4/91

Jacobs, Z., Jones, B.G., Cawthra, H.C., Henshilwood, C.S., Roberts, R.G., 2020. The chronological, sedimentary and environmental context for the archaeological deposits at Blombos Cave, South Africa. Quaternary Science Reviews 235, 105850. http://doi.org/10.1016/j.quascirev.2019.07.032

Lauer, T., Weiss, M., Bernhardt, W., Heinrich, S., Rappsilber, I., Stahlschmidt, M.C., von Suchodoletz, H., Wansa, S., 2020. The Middle Pleistocene fluvial sequence at Uichteritz, central Germany: Chronological framework, paleoenvironmental history and early human presence during MIS 11. Geomorphology 354, 107016. http://doi.org/10.1016/j.geomorph.2019.107016

Liritzis, I., Miller, M.C., L., A., 2020. The value of OSL in distinguishing ancient from more recent structures in an archaeological landscape. Scientific Culture 6, 23-34. https://sci-cult.com/the-value-of-osl-in-distinguishing-ancient-from-more-recent-structures-in-an-archaeological-landscape/

Meyer, M.C., Gliganic, L.A., May, J.H., Merchel, S., Rugel, G., Schlütz, F., Aldenderfer, M.S., Krainer, K., 2020. Landscape dynamics and human-environment interactions in the northern foothills of Cho Oyu and Mount Everest (southern Tibet) during the Late Pleistocene and Holocene. Quaternary Science Reviews 229, 106127. http://doi.org/10.1016/j.quascirev.2019.106127

Moore, M.W., Westaway, K., Ross, J., Newman, K., Perston, Y., Huntley, J., Keats, S., Kandiwal Aboriginal, C., Morwood, M.J., 2020. Archaeology and art in context: Excavations at the Gunu Site Complex, Northwest Kimberley, Western Australia. PLOS ONE 15, e0226628. http://doi.org/10.1371/journal.pone.0226628

Pietsch, T., Kemp, J., Pardoe, C., Grün, R., Olley, J., Wood, R., 2019. A multi-method approach to dating the burial and skeleton of Kiacatoo Man, New South Wales, Australia. Journal of Quaternary Science 34, 662-673. http://doi.org/10.1002/jqs.3165

Rizal, Y., Westaway, K.E., Zaim, Y., van den Bergh, G.D., Bettis, E.A., Morwood, M.J., Huffman, O.F., Grün, R., Joannes-Boyau, R., Bailey, R.M., Sidarto, Westaway, M.C., Kurniawan, I., Moore, M.W., Storey, M., Aziz, F., Suminto, Zhao, J.-x., Aswan, Sipola, M.E., Larick, R., Zonneveld, J.-P., Scott, R., Putt, S., Ciochon, R.L., 2019. Last appearance of Homo erectus at Ngandong, Java, 117,000–108,000 years ago. Nature 577, 381-385. http://doi.org/10.1038/s41586-019-1863-2

Şahiner, E., Polymeris, G.S., Atlihan, M.A., Aktürk, S., Meriç, N., 2020. Indirect dating of an olive tree planting event using luminescence of the sediments lying beneath the roots of the tree: a pilot study in the south-western part of Anatolia, Turkey. Journal of Quaternary Science 35, 706-715. http://doi.org/10.1002/jqs.3212

Slack, M.J., Law, W.B., Gliganic, L.A., 2020. The early occupation of the Eastern Pilbara revisited: New radiometric chronologies and archaeological results from Newman Rockshelter and Newman Orebody XXIX. Quaternary Science Reviews 236, 106240. http://doi.org/10.1016/j.quascirev.2020.106240

Tepper, Y., Porat, N., Bar-Oz, G., 2020. Sustainable farming in the Roman-Byzantine period: Dating an advanced agriculture system near the site of Shivta, Negev Desert, Israel. Journal of Arid Environments 177, 104134. http://doi.org/10.1016/j.jaridenv.2020.104134

Tsukamoto, S., Takeuchi, T., Tani, A., Miyairi, Y., Yokoyama, Y., 2020. ESR and radiocarbon dating of gut strings from early plucked instruments. Methods and Protocols 3, 13. http://doi.org/10.3390/mps3010013

Watanabe, S., Cano, N.F., Carvalho-Júnior, A.B., Ayala-Arenas, J.S., Gonzales-Lorenzo, C.D., Rao, T.K.G., 2019. Dating of carbonate covering cave paintings at peruaçu, Brazil by TL and EPR methods. Applied Radiation and Isotopes 153, 108847. http://doi.org/10.1016/j.apradiso.2019.108847

Wright, D.K., MacEachern, S., Ambrose, S.H., Choi, J., Choi, J.-H., Lang, C., Wang, H., 2019. Iron Age landscape changes in the Benoué River Valley, Cameroon. Quaternary Research 92, 323-339. http://doi.org/10.1017/qua.2019.25

Yang, L., Long, H., Cheng, H., Hu, G., Duan, H., Zhao, H., 2020. Historical settlement abandonment in the middle Hexi Corridor linked to human-induced desertification. Palaeogeography, Palaeoclimatology, Palaeoecology 545, 109634. http://doi.org/10.1016/j.palaeo.2020.109634

Various ESR applications

Bahain, J.J., Dolo, J.M., Falguères, C., Garcia, T., Trompier, F., 2020. Dosimetry of ionising radiation, in: Bertrand, P. (Ed.), Electron Paramagnetic Resonance Spectroscopy: Applications. Springer International Publishing, Cham, pp. 1-28. http://doi.org/10.1007/978-3-030-39668-8_1

Bertrand, P., 2020. Electron paramagnetic resonance spectroscopy. Springer. http://doi.org/10.1007/978-3-030-39663-3

Blackwell, A.B.B., Kazi, F.M., Huang, L.C.C., Doronicheva, V.E., Golovanova, V.L., Doronichev, B.V., Singh, K.C.I., Blickstein, I.B.J., 2020. Sedimentary dosimetry for the Saradj-Chuko Grotto: A cave in a Lava Tube in the North-Central Caucasus, Russia. Methods and Protocols 3, 20. http://doi.org/10.3390/mps3010020

Blackwell, B.A.B., Šalamanov-Korobar, L., Huang, C.L.C., Zhuo, J.L., Kitanovski, B., Blickstein, J.I.B., Florentin, J.A., Vasilevski, S., 2019. Sedimentary radioactivity in an upper paleolithic-middle paleolithic (MP-UP) transition site: Increasing ESR tooth dating accuracy at Golema Pešt, North Macedonia. Radiation Protection Dosimetry 186, 94-112. http://doi.org/10.1093/rpd/ncz183

Cano, N.F., Ayala-Arenas, J.S., Javier-Ccallata, H.S., Watanabe, S., 2020. OSL and EPR dating of shells and sediments from Congonhas II sambaqui, Santa Catarina, Brazil. Radiation Physics and Chemistry 167, 108240. http://doi.org/10.1016/j.radphyschem.2019.03.044

Daujeard, C., Falguères, C., Shao, Q., Geraads, D., Hublin, J.-J., Lefèvre, D., Graoui, M.E., Rué, M., Gallotti, R., Delvigne, V., Queffelec, A., Arous, E.B., Tombret, O., Mohib, A., Raynal, J.-P., 2020. Earliest African

evidence of carcass processing and consumption in cave at 700 ka, Casablanca, Morocco. Scientific Reports 10, 4761. http://doi.org/10.1038/s41598-020-61580-4

Dirks, P.H.G.M., Roberts, E.M., Hilbert-Wolf, H., Kramers, J.D., Hawks, J., Dosseto, A., Duval, M., Elliott, M., Evans, M., Grün, R., Hellstrom, J., Herries, A.I.R., Joannes-Boyau, R., Makhubela, T.V., Placzek, C.J., Robbins, J., Spandler, C., Wiersma, J., Woodhead, J., Berger, L.R., 2017. The age of Homo naledi and associated sediments in the Rising Star Cave, South Africa. eLife 6, e24231. http://doi.org/10.7554/eLife.24231

Duval, M., Martin, L., 2019. ESR dating of fossil teeth: In which extent the thickness of adjacent tissues should be taken into account in the external beta dose rate evaluation? Geochronometria 46, 102-110. http://doi.org/10.1515/geochr-2015-0105

Gutiérrez, F., Moreno, D., López, G.I., Jiménez, F., del Val, M., Alonso, M.J., Martínez-Pillado, V., Guzmán, O., Martínez, D., Carbonel, D., 2020. Revisiting the slip rate of Quaternary faults in the Iberian Chain, NE Spain. Geomorphic and seismic-hazard implications. Geomorphology 363, 107233. http://doi.org/10.1016/j.geomorph.2020.107233

Hayes, R.B., Abdelrahman, F.M., 2020. Low level EPR dosimetry of a commercial sugar. Applied Radiation and Isotopes 157, 109038. http://doi.org/10.1016/j.apradiso.2020.109038

Hayes, R.B., O'Mara, R.P., Hooper, D.A., 2019. Initial TL/OSL/EPR considerations for commercial diatomaceous earth in retrospective dosimetry and dating. Radiation Protection Dosimetry 185, 310-319. http://doi.org/10.1093/rpd/ncz013

Ma, Z., Feng, Z., Peng, T., Liu, S., Li, M., Guo, B., Li, X., Song, C., Zhao, Z., Li, J., 2020. Quaternary drainage evolution of the Datong River, Qilian Mountains, northeastern Tibetan Plateau, China. Geomorphology 353, 107021. http://doi.org/10.1016/j.geomorph.2019.107021

Medialdea, A., May, S.M., Brill, D., King, G., Ritter, B., Wennrich, V., Bartz, M., Zander, A., Kuiper, K., Hurtado, S., Hoffmeister, D., Schulte, P., Gröbner, M., Opitz, S., Brückner, H., Bubenzer, O., 2020. Identification of humid periods in the Atacama Desert through hillslope activity established by infrared stimulated luminescence (IRSL) dating. Global and Planetary Change 185, 103086. http://doi.org/10.1016/j.gloplacha.2019.103086

Rizal, Y., Westaway, K.E., Zaim, Y., van den Bergh, G.D., Bettis, E.A., Morwood, M.J., Huffman, O.F., Grün, R., Joannes-Boyau, R., Bailey, R.M., Sidarto, Westaway, M.C., Kurniawan, I., Moore, M.W., Storey, M., Aziz, F., Suminto, Zhao, J.-x., Aswan, Sipola, M.E., Larick, R., Zonneveld, J.-P., Scott, R., Putt, S., Ciochon, R.L., 2019. Last appearance of Homo erectus at Ngandong, Java, 117,000–108,000 years ago. Nature 577, 381-385. http://doi.org/10.1038/s41586-019-1863-2

Tsukamoto, S., Takeuchi, T., Tani, A., Miyairi, Y., Yokoyama, Y., 2020. ESR and radiocarbon dating of gut strings from early plucked instruments. Methods and Protocols 3, 13. http://doi.org/10.3390/mps3010013

Watanabe, S., Cano, N.F., Carvalho-Júnior, A.B., Ayala-Arenas, J.S., Gonzales-Lorenzo, C.D., Rao, T.K.G., 2019. Dating of carbonate covering cave paintings at peruaçu, Brazil by TL and EPR methods. Applied Radiation and Isotopes 153, 108847. http://doi.org/10.1016/j.apradiso.2019.108847

Wei, C.-Y., Liu, C.-R., Li, C.-A., Yin, G.-M., Zhang, Y.-F., Li, W.-P., Yu, L.-P., 2019. Application of long time artificial optical bleaching of the E1' centre to sediment ESR dating. Geochronometria 46, 79-86. http://doi.org/10.1515/geochr-2015-0106

Basic research

Benavente, J.F., Gómez-Ros, J.M., Romero, A.M., 2019. Thermoluminescence glow curve deconvolution for discrete and continuous trap distributions. Applied Radiation and Isotopes 153, 108843. http://doi.org/10.1016/j.apradiso.2019.108843

Benavente, J.F., Gómez-Ros, J.M., Romero, A.M., 2020. Numerical analysis of the irradiation and heating processes of thermoluminescent materials. Radiation Physics and Chemistry 170, 108671. http://doi.org/10.1016/j.radphyschem.2019.108671

Chang, Z., Zhou, L., 2019. Evidence for provenance change in deep sea sediments of the Bengal Fan: A 7 million year record from IODP U1444A. Journal of Asian Earth Sciences 186, 104008. http://doi.org/10.1016/j.jseaes.2019.104008

Chen, R., Pagonis, V., 2020. A Monte-Carlo study of the fading of TL and OSL signals in the presence of deep-level competitors. Radiation Measurements 132, 106257. http://doi.org/10.1016/j.radmeas.2020.106257

Chithambo, M.L., Dawam, R.R., 2020. Phototransferred thermoluminescence of annealed synthetic quartz: Analysis of illumination-time profiles, kinetics and competition effects. Radiation Measurements 131, 106236. http://doi.org/10.1016/j.radmeas.2019.106236

Chithambo, M.L., Kalita, J.M., Finch, A.A., 2020. F- and F+-band radioluminescence and the influence of annealing on its emission spectra in Al2O3:C,Mg. Radiation Measurements 134, 106306. http://doi.org/10.1016/j.radmeas.2020.106306

Delice, S., 2018. Temperature lag effect on TL glow peaks: Corrections on kinetic parameters. Journal of Luminescence 204, 81-88. http://doi.org/10.1016/j.jlumin.2018.07.044

Dorenbos, P., 2018. The hole picture as alternative for the common electron picture to describe hole trapping and luminescence quenching. Journal of Luminescence 197, 62-65. http://doi.org/10.1016/j.jlumin.2018.01.013

Duller, G.A.T., Gunn, M., Roberts, H.M., 2020. Single grain infrared photoluminescence (IRPL) measurements of feldspars for dating. Radiation Measurements 133, 106313. http://doi.org/10.1016/j.radmeas.2020.106313

Guo, Y., Li, B., Zhao, H., 2020. Comparison of single-aliquot and single-grain MET-pIRIR De results for potassium feldspar samples from the Nihewan Basin, northen China. Quaternary Geochronology 56, 101040. http://doi.org/10.1016/j.quageo.2019.101040

Heydari, M., Guérin, G., Kreutzer, S., Jamet, G., Kharazian, M.A., Hashemi, M., Nasab, H.V., Berillon, G., 2020. Do Bayesian methods lead to more precise chronologies? 'BayLum' and a first OSL-based chronology for the Palaeolithic open-air site of Mirak (Iran). Quaternary Geochronology 59, 101082. http://doi.org/10.1016/j.quageo.2020.101082

Hu, Y., Li, B., Jacobs, Z., 2020. Single-grain quartz OSL characteristics: Testing for correlations within and between sites in Asia, Europe And Africa. Methods and Protocols 3, 2. http://doi.org/10.3390/mps3010002

Kaya-Keleş, Ş., Polymeris, G.S., Perçinler, B., Meriç, N., 2020. Dealing with non-conventional LM-OSL curve shapes in quartz following bleaching; a deconvolution approach. Journal of Luminescence 220, 117026. http://doi.org/10.1016/j.jlumin.2020.117026

Kazakis, N.A., 2019. Comment on the paper 'luminescence models by S.W.S. Mckeever and R. Chen, Radiation Measurements 27(5/6), 1997, pp. 625–661'. Radiation Protection Dosimetry 185, 131-134. http://doi.org/10.1093/rpd/ncy281

Kitis, G., Pagonis, V., 2018. Localized transition models in luminescence: A reappraisal. Nuclear Instruments and Methods in Physics Research Section B: Beam Interactions with Materials and Atoms 432, 13-19. http://doi.org/10.1016/j.nimb.2018.06.029

Kitis, G., Polymeris, G.S., Pagonis, V., 2019. Stimulated luminescence emission: From phenomenological models to master analytical equations. Applied Radiation and Isotopes 153, 108797. http://doi.org/10.1016/j.apradiso.2019.05.041

Kumar, M., 2019. Further considerations on "Towards the origins of over-dispersion in beta source calibration" by Hansen et al., radiation measurements, 2018. Radiation Measurements 126, 106137. http://doi.org/10.1016/j.radmeas.2019.106137

Lamothe, M., Forget Brisson, L., Hardy, F., 2020. Circumvention of anomalous fading in feldspar luminescence dating using Post-Isothermal IRSL. Quaternary Geochronology 57, 101062. http://doi.org/10.1016/j.quageo.2020.101062

Li, B., Jacobs, Z., Roberts, R.G., 2020. Validation of the LnTn method for De determination in optical dating of K-feldspar and quartz. Quaternary Geochronology 58, 101066. http://doi.org/10.1016/j.quageo.2020.101066

Mendes, V.R., Sawakuchi, A.O., Chiessi, C.M., Giannini, P.C.F., Rehfeld, K., Mulitza, S., 2019. Thermoluminescence and optically stimulated luminescence measured in marine sediments indicate precipitation changes over northeastern Brazil. Paleoceanography and Paleoclimatology 34, 1476-1486. http://doi.org/10.1029/2019PA003691

Pagonis, V., Kreutzer, S., Duncan, A.R., Rajovic, E., Laag, C., Schmidt, C., 2020. On the stochastic uncertainties of thermally and optically stimulated luminescence signals: A Monte Carlo approach. Journal of Luminescence 219, 116945. http://doi.org/10.1016/j.jlumin.2019.116945

Polymeris, G.S., Pagonis, V., Kitis, G., 2020. Investigation of thermoluminescence processes during linear and isothermal heating of dosimetric materials. Journal of Luminescence 222, 117142. http://doi.org/10.1016/j.jlumin.2020.117142

Rui, X., Li, B., Guo, Y., 2020. The effect of residual signal on dose measurements using MET-pIRIR signals from K-feldspar. Quaternary Geochronology 58, 101065. http://doi.org/10.1016/j.quageo.2020.101065

Rui, X., Li, B., Guo, Y., 2020. Testing the upper limit of luminescence dating based on standardised growth curves for MET-pIRIR signals of K-feldspar grains from northern China. Quaternary Geochronology 57, 101063. http://doi.org/10.1016/j.quageo.2020.101063

Sawakuchi, A.O., Rodrigues, F.C., Mineli, T.D., Mendes, V.R., Melo, D.B., Chiessi, C.M., Giannini, P.C., 2020. Optically stimulated luminescence sensitivity of quartz for provenance analysis. Methods and Protocols 3, 6. http://doi.org/10.3390/mps3010006

Soni, A., Mishra, D.R., 2016. Mathematical formulation of Tmax–Tstop method for LM-OSL and its experimental validation on α-Al2O3:C. Nuclear Instruments and Methods in Physics Research Section B: Beam Interactions with Materials and Atoms 375, 87-92. http://doi.org/10.1016/j.nimb.2016.03.039

Trindade, N.M., Jacobsohn, L.G., Yoshimura, E.M., 2019. Correlation between thermoluminescence and optically stimulated luminescence of α-Al2O3:C,Mg. Journal of Luminescence 206, 298-301. http://doi.org/10.1016/j.jlumin.2018.10.084

Williams, O.M., Spooner, N.A., 2020. Quartz optically stimulated luminescence configurational coordinate model. Radiation Measurements 132, 106259. http://doi.org/10.1016/j.radmeas.2020.106259

Yukihara, E.G., 2019. Characterization of the thermally transferred optically stimulated luminescence (TT-OSL) of BeO. Radiation Measurements 126, 106132. http://doi.org/10.1016/j.radmeas.2019.106132

Zhang, J., Wang, L., 2020. Thermoluminescence dating of calcite – Alpha effectiveness and measurement protocols. Journal of Luminescence 223, 117205. http://doi.org/10.1016/j.jlumin.2020.117205

Zhou, R., Wei, M.-J., Song, B., Zhang, Y., Zhao, Q.-Y., Pan, B.-L., Li, T.-F., 2016. Evaluation of trapping parameters of annealed natural quartz. Nuclear Instruments and Methods in Physics Research Section B: Beam Interactions with Materials and Atoms 375, 32-39. http://doi.org/10.1016/j.nimb.2016.02.067

Dose rate issues

Degering, D., Degering, A., 2020. Change is the only constant - time-dependent dose rates in luminescence dating. Quaternary Geochronology 58, 101074. http://doi.org/10.1016/j.quageo.2020.101074

Duval, M., Martin, L., 2019. ESR dating of fossil teeth: In which extent the thickness of adjacent tissues should be taken into account in the external beta dose rate evaluation? Geochronometria 46, 102-110. http://doi.org/10.1515/geochr-2015-0105

Hood, A.G.E., Highcock, E.G., 2019. Using DosiVox to reconstruct radiation transport through complex archaeological environments. Methods and Protocols 2, 91. https://www.mdpi.com/2409-9279/2/4/91

Riedesel, S., Autzen, M., 2020. Beta and gamma dose rate attenuation in rocks and sediment. Radiation Measurements 133, 106295. http://doi.org/10.1016/j.radmeas.2020.106295

Smedley, R.K., Duller, G.A.T., Rufer, D., Utley, J.E.P., 2020. Empirical assessment of beta dose heterogeneity in sediments: Implications for luminescence dating. Quaternary Geochronology 56, 101052. http://doi.org/10.1016/j.quageo.2020.101052

Dosimetry

Atlıhan, M.A., 2020. Thermoluminescence properties of two natural colorful fluorite samples of Anatolian origin for dosimetric applications. Nuclear Instruments and Methods in Physics Research Section B: Beam Interactions with Materials and Atoms 467, 33-39. http://doi.org/10.1016/j.nimb.2020.02.002

Discher, M., Woda, C., Lee, J., Kim, H., Chung, K., Lang, A., 2020. PTTL characteristics of glass samples from mobile phones. Radiation Measurements 132, 106261. http://doi.org/10.1016/j.radmeas.2020.106261

Hayes, R.B., Abdelrahman, F.M., 2020. Low level EPR dosimetry of a commercial sugar. Applied Radiation and Isotopes 157, 109038. http://doi.org/10.1016/j.apradiso.2020.109038

Hayes, R.B., O'Mara, R.P., Hooper, D.A., 2019. Initial TL/OSL/EPR considerations for commercial diatomaceous earth in retrospective dosimetry and dating. Radiation Protection Dosimetry 185, 310-319. http://doi.org/10.1093/rpd/ncz013

Hoedlmoser, H., Greiter, M., Bandalo, V., Brönner, J., Kleinau, P., Haninger, T., Mende, E., Emmerl, M., Scheubert, P., Esser, R., Figel, M., 2020. Individual monitoring with BeOSL dosemeters: New dosemeters for extremity and area dosimetry. Radiation Measurements 132, 106258. http://doi.org/10.1016/j.radmeas.2020.106258

Kazakis, N.A., Tsirliganis, N.C., 2019. Optically stimulated luminescence investigation of chicken bones towards their use at food post-sterilization and retrospective dosimetry. Applied Radiation and Isotopes 154, 108899. http://doi.org/10.1016/j.apradiso.2019.108899

McKeever, S.W.S., Sholom, S., Shrestha, N., Klein, D.M., 2020. An in-situ, fiber-optic system for sub-surface, environmental dose measurements using radiophotoluminescence from Ag-doped alkali-phosphate glass. Radiation Measurements 132, 106273. http://doi.org/10.1016/j.radmeas.2020.106273

Polymeris, G.S., Başdoğan, M., Çakal, G.Ö., Aşlar, E., Meriç, N., 2020. Gamma dose rate effects in luminescence signals of various artificial, well established dosimetric phosphors. Radiation Measurements 133, 106282. http://doi.org/10.1016/j.radmeas.2020.106282

Sądel, M., Bilski, P., Kłosowski, M., Sankowska, M., 2020. A new approach to the 2D radiation dosimetry based on optically stimulated luminescence of LiF:Mg,Cu,P. Radiation Measurements 133, 106293. http://doi.org/10.1016/j.radmeas.2020.106293

Siti Rozaila, Z., Khandaker, M.U., Wahib, N.b., Hanif bin Abdul Jilani, M.K., Abdul Sani, S.F., Bradley, D.A., 2020. Thermoluminescence characterization of smartphone screen for retrospective accident dosimetry. Radiation Physics and Chemistry 167, 108297. http://doi.org/10.1016/j.radphyschem.2019.04.047

Surdo, A., Abashev, R., Milman, I., 2020. On the possibility of photo- and photo-thermal depletion of deep traps in α-Al2O3-δ. Nuclear Instruments and Methods in Physics Research Section B: Beam Interactions with Materials and Atoms 467, 97-101. http://doi.org/10.1016/j.nimb.2020.02.004

Takagi, H., Yanagisawa, S., Koba, Y., Shinsho, K., 2020. Basic study of an effective energy measurement method using a stacked thermoluminescence dosimeter. Radiation Measurements 133, 106283. http://doi.org/10.1016/j.radmeas.2020.106283

Yukihara, E.G., 2019. Characterization of the thermally transferred optically stimulated luminescence (TT-OSL) of BeO. Radiation Measurements 126, 106132. http://doi.org/10.1016/j.radmeas.2019.106132

Beyond quartz and K-feldspar: non-traditional minerals

- calcite

Zhang, J., Wang, L., 2020. Thermoluminescence dating of calcite – Alpha effectiveness and measurement protocols. Journal of Luminescence 223, 117205. http://doi.org/10.1016/j.jlumin.2020.117205

Instruments

Finch, A.A., Wang, Y., Townsend, P.D., Ingle, M., 2019. A high sensitivity system for luminescence measurement of materials. Luminescence 34, 280-289. http://doi.org/10.1002/bio.3606

Computer coding

Degering, D., Degering, A., 2020. Change is the only constant - time-dependent dose rates in luminescence dating. Quaternary Geochronology 58, 101074. http://doi.org/10.1016/j.quageo.2020.101074

Review

Bahain, J.J., Dolo, J.M., Falguères, C., Garcia, T., Trompier, F., 2020. Dosimetry of ionising radiation, in: Bertrand, P. (Ed.), Electron Paramagnetic Resonance Spectroscopy: Applications. Springer International Publishing, Cham, pp. 1-28. http://doi.org/10.1007/978-3-030-39668-8_1

Bertrand, P., 2020. Electron paramagnetic resonance spectroscopy. Springer. http://doi.org/10.1007/978-3-030-39663-3

Bösken, J.J., Schmidt, C., 2020. Direct and indirect luminescence dating of tephra: A review. Journal of Quaternary Science 35, 39-53. http://doi.org/10.1002/jqs.3160

Chamberlain, E.L., Goodbred, S.L., Hale, R., Steckler, M.S., Wallinga, J., Wilson, C., 2020. Integrating geochronologic and instrumental approaches across the Bengal Basin. Earth Surface Processes and Landforms 45, 56-74. http://doi.org/10.1002/esp.4687

Doverbratt, I., Alexanderson, H., 2019. Transferring grains from single-grain luminescence discs to SEM specimen stubs. Methods and Protocols 2, 87. https://www.mdpi.com/2409-9279/2/4/87

Gutiérrez, F., Moreno, D., López, G.I., Jiménez, F., del Val, M., Alonso, M.J., Martínez-Pillado, V., Guzmán, O., Martínez, D., Carbonel, D., 2020. Revisiting the slip rate of Quaternary faults in the Iberian Chain, NE Spain. Geomorphic and seismic-hazard implications. Geomorphology 363, 107233. http://doi.org/10.1016/j.geomorph.2020.107233

Nelson, M., Rittenour, T., Cornachione, H., 2019. Sampling methods for luminescence dating of subsurface deposits from cores. Methods and Protocols 2, 88. https://www.mdpi.com/2409-9279/2/4/88

Zhang, J., Li, S.-H., 2020. Review of the Post-IR IRSL dating protocols of K-feldspar. Methods and Protocols 3, 7. http://doi.org/10.3390/mps3010007

Conference Announcements: DLED 2020

German Luminescence and ESR Meeting

27 – 29 November 2020, Leipzig, Germany

www.eva.mpg.de/evolution/dled2020
DLED2020@eva.mpg.de

Registration:
Opens 15 July 2020
Closes 31 October 2020

Organising committee:
Tobias Lauer
Debra Colarossi
Daniel Richter
Michael Hein
Steffi Hesse
Victoria Krippner

This is the first announcement for the 2020 German luminescence and ESR meeting (DLED2020). The meeting will be hosted by the Luminescence group at the Department of Human Evolution, Max Planck Institute for Evolutionary Anthropology in Leipzig, Germany.

Further information will be made available through the meeting website so please bookmark the page.

We look forward to welcoming you in Saxony.

Ancient TL

ISSN 0735-1348

Aims and Scope

Ancient TL is a journal devoted to Luminescence dating, Electron Spin Resonance (ESR) dating, and related techniques. It aims to publish papers dealing with experimental and theoretical results in this field, with a minimum of delay between submission and publication. Ancient TL also publishes a current bibliography, thesis abstracts, letters, and miscellaneous information, e.g., announcements for meetings.

Frequency

Two issues per annum in June and December

Submission of articles to Ancient TL

Ancient TL has a reviewing system in which direct dialogue is encouraged between reviewers and authors. For instructions to authors and information on how to submit to Ancient TL, please visit the website at:
http://ancienttl.org/TOC1.htm

Journal Enquiries

For enquiries please contact the editor:
Regina DeWitt, Department of Physics, East Carolina University, Howell Science Complex, 1000 E. 5th Street, Greenville, NC 27858, USA; Tel: +252-328-4980; Fax: +252-328-0753 (dewittr@ecu.edu)

Subscriptions to Ancient TL

Ancient TL Vol. 32 No.2 December 2014 was the last issue to be published in print. Past and current issues are available for download free of charge from the Ancient TL website:
http://ancienttl.org/TOC4.htm